Graduate Theses, Dissertations, and Problem Reports

2018

Impacts of land use and land cover change on regional climate in China

Yaqian He

Impacts of land use and land cover change on regional climate in China

Yaqian He

Dissertation submitted
to the Eberly College of Arts and Science
at West Virginia University

in partial fulfillment of the requirements for the degree of

Doctor of Philosophy in
Department of Geology and Geography

Eungul Lee, Ph.D., Chair
Timothy Warner, Ph.D.
Brenden McNeil, Ph.D.
Nicolas Zégre, Ph.D.
Lei Meng, Ph.D.

Department of Geology and Geography

Morgantown, West Virginia
2018

ABSTRACT

Impacts of land use and land cover change on regional climate in China

Yaqian He

The purpose of this research is to investigate, using an empirical approach, the effects of land use and land cover change (LULCC) on the regional climate of China. Land surface is one of the important factors in determining regional climate. Changed land surface conditions (e.g. changes in albedo, soil moisture, surface roughness, and leaf area index) due to LULCC have caused significant impacts to regional climates across the globe. China, which is home to more than 1.3 billion people, has experienced extensive LULCC since the economic reform of 1978. Summer and Autumn rainfall in China has significantly increased in the south and decreased in the north in the past four decades. Understanding the influences of LULCC on regional climate variability of China will greatly improve climate forecasts, directly benefiting society, including famers and water resources managers. Consequently, an integrated study on the role of LULCC on regional climate of China is of great necessity.

In order to tackle the role of LULCC on regional climate in China, I divided this study into three parts. First, I produced a continuous series of annual land use and land cover (LULC) maps of China from 1982 to 2013 using random forest classification of 19 phenological metrics derived from Advanced Very High Resolution Radiometer (AVHRR) Global Inventory Modeling and Mapping Studies (GIMMS) third generation NDVI (NDVI3g) data. The 19 phenological metrics include start of growing season, end of growing season, maximum and minimum NDVI values, and so on. The classifier was trained using reference data derived from the MODIS land cover type product (MCD12Q1). The resulting AVHRR LULC maps were compared to the annual MODIS LULC products for the years 2001-2012, and an agreement of between 69.3% and 72.5% was found. Similarly, the overall consistency between the AVHRR LULC maps and the Chinese Land-Use/cover (CLU) dataset, for the years 1995, 2000, 2005, and 2010, was found to be 64.3%, 64.3%, 63.0%, and 64.4%, respectively. Based on a more traditional error evaluation using high resolution 2012 Google Earth images as a reference source, the overall accuracy of a simplified eight-class version of the 2012 LULC map was estimated to be 73.8%, which is not significantly different from the accuracy of the MODIS map of the same year. These inter-comparison and accuracy evaluation indicate the reliability of our AVHRR LULC maps.

Secondly, I explored the effects of three spatial scaling methods on correlations among LULC data and a land surface climatic variable, latent heat flux. Scaling by a fractional method preserved significant correlations among LULC data and latent heat flux at all three studied scales (0.5°, 1.0°, and 2.5°), whereas nearest neighbor and majority aggregation methods caused these correlations to diminish and even become statistically non-significant at coarser spatial scales (i.e., 2.5°). Based on the fractional method, I identified fractional changes in croplands, forests, and grasslands in China using the continuous series of LULC maps from 1982 to 2012. Relative to common

LULC change analyses conducted over two time steps or several time periods, this annually-resolved and 31-year time-series of LULC maps enables robust interpretation of LULC change. Specifically, the annual resolution of these data enabled us to more precisely observe three key and statistically significant LULCC trends and transitions that could have consequential effects on land-atmosphere interaction: (1) decreasing grasslands being replaced by increasing croplands in the Northeast China plain and the Yellow river basin, (2) decreasing croplands being replaced by increasing forests in the Yangtze river basin, and (3) decreasing grasslands being replaced by increasing forests in Southwest China.

Finally, I examined the impacts of croplands expansion on temperature in the troposphere during late summer of August and September in Northeast China from 1982 to 2010. By using statistical methods including correlation analysis, linear regression analysis, and Granger-causality test, the relationships between croplands fractions and climatic variables (i.e., latent heat flux, sensible heat flux, surface temperature, multi-level temperature, and geopotential height) and their underlying physical mechanisms were investigated. I found that the increased croplands in Northeast China results in increased latent heat flux in the regions with significantly increased croplands. The increased latent heat flux decreases surface temperature. The cooling effect of cropland expansion in Northeast China also extends to upper-level troposphere.

Overall, this dissertation contributes to multidisciplinary geospatial research by applying remote sensing and climatological analyses to study the roles of LULCC in affecting regional climate of China. The 32 years of sequential annual LULC maps generated by this dissertation provide a valuable database of LULCC information for China. The examining of existing methods to address scale issues between remotely sensed data and climate data contributes to the integration of remote sensing and climate research. The insight regarding potential physical mechanisms for the effects of croplands expansion on regional climate advance the knowledge in land-atmosphere interaction studies in the mid-latitude regions.

Dedication

For my parents and sister.

For my husband.

Thank you for your love and support.

Acknowledgments

Any time hurry, any time flies. The day when I arrived Morgantown is still vivid in my mind, while five years have passed. This dissertation not only stands for a scientific product for my PhD degree, but also a memorable life for me in Morgantown. At this special moment, I would like to take this opportunity to express my gratitude to those who provided me with their invaluable support and accompany throughout the whole journey of my doctoral studies.

First of all, I would like to thank my advisor Dr. Eungul Lee. It is definitely true that this dissertation cannot be completed without Dr. Lee's guidance and support. My background is remote sensing and I knew little about climatology in the first year of PhD. Dr. Lee helped me establish my fundamental knowledge in climatology through providing books, articles, and frequent discussions. I cherished the lunch time with Dr. Lee and other lab members in my first three years, when I could express any questions no matter how silly they are. Dr. Lee trained me to obtain skills of not only climate model, programmer language, scientific writing, but also the way to conduct research. I learned from Dr. Lee how to build hypothesis and how to explore the research questions following the hypothesized physical mechanisms step by step. This systematic training has profoundly influenced and inspired me to be an independent researcher. I enjoyed the moments when I encountered difficulties, Dr. Lee could always point me to another possibilities. This incited me to continue my research with enthusiasm. In my fourth year of PhD, I was pregnant. Dr. Lee encouraged me and shared his wife's (Dr. Hyun Jung Yang) experience with me, which supported me to conduct my research smoothly. I appreciate Dr. Lee for his four years' funding supporting, enabling me to work as a research assistant. Dr. Lee has been academically and professionally engaged in this dissertation. I am highly grateful to Dr. Lee.

I would like to express my sincere thanks to my committee members. I learned logicality in research, scientific writing skill, and strategy of responding to reviewer's comments from Dr. Timothy Warner. I would not forget the day when Dr. Warner came

to our lab and sat beside me in order to help me make sure my experiments design related to validate land use and land cover maps using Google Earth was right. Dr. Warner's quick, detail, and constructive suggestions for my works, leading to my first and second chapters of this dissertation. I appreciate Dr. Warner for his generous supporting for me to attend 2016 IGARSS in Beijing, China and for his frequent concerning about my health during my pregnancy. Dr. Brenden McNeil helped me extend research area in remote sensing through his course 'Remote Sensing of Ecosystems'. I am grateful to Dr. McNeil to his creative suggestions to my term project, leading to my second chapter of this dissertation. In my fifth year, I was preparing for my next step and applying several postdoc/faculty positions. It is much more stressful than past four years. I am thankful to Dr. McNeil for his suggestions on my application materials. I would not forget the moment that Dr. McNeil said he would stay at office during the week of Christmas in order to help me revise a cover letter properly. I learned water cycle, hydrology data analysis using R, and Budyko curve from Dr. Nicolas Zégre. Dr. Zégre is always energetic and inspired me to be a passionate researcher. I am thankful to Dr. Zégre for giving me the opportunity to acquire experience in guest lecture about remote sensing of vegetation. Dr. Zégre's constructive suggestions on my term project led to my final chapter of this dissertation. I am grateful to Dr. Lei Meng at Western Michigan University. Dr. Meng gave me advice on Granger-causality test and encouraged me to use climate model to conduct analysis. I am thankful for Dr. Meng for his generous to share Chinese Meteorology Station data with me. This data is an important component in the final chapter of this dissertation.

I also would like to thank Dr. Jingjing Liang and Dr. Mo Zhou for their guidance and discussions on exploring roles of vegetation activities on the Sahel summer rainfall, which strengthened my statistical skills. I am grateful to Dr. Yong-Lak Park for his humorous and insights on bee-mite-blueberry project, which extended my research area and brought much fun into my research. Thanks to Dr. Jeong Joon Ahn for his detail explanation to help me better understand emergence and development of bee and mite. I am thankful to my Master's advisor Dr. Yanchen Bo, at Beijing Normal University, for

Table of Contents

List of Tables

List of Figures

List of Abbreviation

LULCC	Land Use and Land Cover Change
LULC	Land Use and Land Cover
MODIS	Moderate-resolution Imaging Spectroradiometer
AVHRR	Advanced Very High Resolution Radiometer
NDVI	Normalized Difference Vegetation Index
GIMMS	Global Inventory Modeling and Mapping Studies
IGBP	International Geosphere-biosphere Programme
CLU	Chinese Land-Use/cover
RESDC	Data Center for Resources and Environmental Sciences
NetCDF	Network Common Data Form
CCRS	Canadian Centre for Remote Sensing
IPCC	Intergovernmental Panel on Climate Change
NCEP	National Center for Environmental Prediction
NCAR	National Center for Atmospheric Research
ECMWF	European Centre for Medium-Range Weather Forecasts
CRU TS	Climate Research Unit Time-series
GIS	Geographic Information System
CESM	Community Earth System Model
TM	Landsat Thematic Mapper
ETM+	Enhanced Thematic Mapper Plus
IDL	Interactive data language
FLUXNET-MTE	FLUXNET-Multi-Tree Ensemble
fAPAR	fraction of Absorbed Photosynthetically Active Radiation
GPCC	Global Precipitation Climatology Center
ERS	European Remote Sensing Satellite

1 Introduction

Summer and autumn rainfall accounts for more than 40% of the annual total precipitation in China (Yang and Lau 2004). From 1977 to 2008, the interannual variability of summer and autumn rainfall has intensified with more extreme wet and dry years (Ye 2014). In addition, summer and autumn rainfall in China has significantly increased in the south and decreased in the north areas in the past four decades (Piao et al. 2010, Ye 2014). The significant changes in rainfall often result in severe drought or floods. In 2004, floods in Hunan province of central China destroyed 2.6 million houses, and a drought in Harbin in Heilongjiang provinces of Northeast China led to the drying up of sections of the Songhuajiang River, one of the longest rivers in China (Chao 2004). It is of great importance to investigate the reasons for the intensified variation of regional climate over China.

Both observational and modeling studies have shown that land use and land cover change (LULCC) could significantly impact the climate system (Takata, Saito and Yasunari 2009, Webster 1987). This may happen by means of biogeophysical processes (changes in water and energy balance) through modifying the surface wetness, partitioning the surface energy between sensible and latent heat fluxes, and altering the roughness of the land surface (McPherson 2007). China has experienced extensive LULCC, including cropland expansion, desertification, deforestation, afforestation, and urbanization (Houghton and Hackler 2003, Lin and Ho 2003, Ge et al. 2004, Liu et al. 2005). There have been many studies that have attempted to explicate the role of LULCC in the regional climate of China (Lee et al. 2011, Xue 1996, Fu 2003, Jones, Lister and Li 2008, Han and Yang 2013). For example, Xue (1996) investigated the impact of desertification in the Mongolian and the Inner Mongolian grasslands on the regional climate of China, and found a weakened East Asian summer monsoon due to the sinking motion of air, which was caused by the reduction of convective latent heating above the surface of the area, where desertification was prevalent.

Previous studies on the climate in China have mainly concentrated on modeling (Xue 1996, Ma et al. 2013a, Ma et al. 2013b, Zhao et al. 2012). For instance, Ma et al. (2013a) used the National Center for Atmospheric Research Community Climate System Model (CCSM) to examine the roles of afforestation in influencing the climate of East China, and found that summer cooling could be attributed to the enhanced evapotranspiration. Those modeling studies were primarily limited by three factors (Wang et al. 2014). Firstly, their results were model-dependent; different models might produce different results. Second, nearly all of the modeling studies involved extreme sensitivity experiments. For example, in order to examine the effects of desertification on regional climate, Xue (1996) completely replaced the grass in Inner Mongolia with bare soil. Such extreme experiments are likely to be unrealistic as vegetation changes tend to be heterogeneous and partial. Third, the model uncertainty, such as the uncertainty of model parameters, could influence the results. Thus, owing to the limitations of modeling studies, observational studies are essential to help constrain model results.

Due to the scarcity of continuous annual land use and land cover maps, previous studies generally have used a map of a specific year representing the entire study period (Zhu 2012), to indicate the locations of LULCC. For instance, Zhu (2012) employed a map of irrigation only for the year 2000 to examine the impacts of irrigation on climate during the period of 1978 to 2008, despite the tremendous change in irrigation infrastructure during theses 30 years. Therefore, obtaining accurate LULCC information on a continuous basis is critical for better understanding the effects of LULCC on climate in China.

Remotely sensed LULC maps usually have very different spatial resolutions from that of climate data, including atmospheric and oceanic variables. For both physical and observational reasons, climate data generally have much coarser spatial resolution than remotely sensed LULC data. For example, National Center for Environmental Prediction (NCEP)/ National Center for Atmospheric Research (NCAR) reanalysis, European Centre for Medium-Range Weather Forecasts (ECMWF) reanalysis (ERA-40), and Climate Research Unit Time-series (CRU TS) high-resolution gridded datasets have a

resolution of 2.5° by 2.5°, 1.125° by 1.125°, and 0.5° by 0.5°, respectively. Simply resampling LULC maps into the same resolution as climate data is problematic, as LULCC is complex, with heterogeneous patterns that may not be evident in simple measures, such as dominant change type, in coarse resolution data. However, the potentially problematic scale effects of the spatial resolution of LULC data and issues of rescaling have been largely overlooked in land-atmosphere interaction studies. It is therefore important to identify the effect of different spatial scaling methods for LULC data on land-atmosphere interaction.

Moreover, previous studies generally have focused on climate responses to urbanization in a single case study area in China, such as the Yangtze River delta (Gu et al. 2011). The rainfall variability in China may also be related to other types of LULCC, such as croplands expansion. The physical mechanisms behind the impacts of different types of LULCC on climate have not been completely understood for China. Consequently, an integrated study on the role of different types of LULCC on the regional climate of China is of great necessity.

The overall objective of this dissertation is to investigate the effects of human-induced LULCC on regional climate in China from an observational perspective. In addressing the overall objective, this dissertation addresses three questions:
1) What are long-term continuous LULC maps in China? (Chapter 2)
2) What is the best spatial scaling method to match LULC data and climate data? (Chapter 3)
3) What are the empirical relationships and their underlying physical mechanisms of land surface variables with atmospheric variables in the geographic areas of LULCC? (Chapter 4)

2 A time series of annual land use and land cover maps of China from 1982 to 2013 generated using AVHRR GIMMS NDVI3g data*

2.1 Background

Land surface condition is an important factor in determining climate through both biophysical and biogeochemical processes (Foley et al. 2003). Recent changes in land surface conditions (e.g., albedo, soil moisture, and surface roughness) and atmospheric composition (e.g., CO_2 and methane) due to land use and land cover change (LULCC) have had significant effects on regional and global climates (McPherson 2007, Lee et al. 2015, Pielke 2005, Mahmood et al. 2014, Bonan, Pollard and Thompson 1992, Foley et al. 2005). For example, Bonan et al. (1992) found that replacing bare ground and tundra with boreal forest results in warming of both winter and summer air temperatures. In a more recent study, He and Lee (2016) found that vegetation growth in the Sahel may have induced the recent trend of increasing rainfall in that region.

There have been many attempts to explore the effects of LULCC on climate based on observational (Lee et al. 2009, Lee et al. 2015, Kaufmann and Stern 1997) and modeling (Douglas et al. 2006, Lee et al. 2011, Eltahir 1996, Lawrence et al. 2012, Lawrence and Chase 2010) studies across the globe (Pielke et al. 2011). Both observational and modeling studies require as an input land use and land cover (LULC) maps that characterize the pattern of changing LULC over time. However, due to the limited length of time for which such LULC maps are available, previous climate studies have often made simplifying assumptions, for example, using a potential vegetation map (Fu 2003) or a single map of a specific year (Zhu 2012) to represent the LULC of the entire study period. For instance, Zhu (2012) employed a single map of irrigation for the year 2000 to examine the impacts of irrigation on climate during the period of 1978 to 2008, despite the tremendous change in irrigation infrastructure during those three decades. Therefore, obtaining a continuous sequence of annual LULC maps over an

extended time period, for at least multiple decades, is critical for quantifying the effects of LULCC on climate.

Townshend et al. (1991) and Running, Loveland and Pierce (1994) have noted that only remotely sensed data can potentially provide accurate and repeatable global land use and land cover for monitoring change. Since then, a number of studies have generated LULC maps in China using remotely sensed data. For instance, Wang et al. (2012) classified urban areas based on Landsat TM/ETM+ data during the years 1986-1994, 1999-2002, and 2008-2010, and examined urban expansion in China from the 1990s to 2010s. Liu et al. (2014) used Landsat and Huanjing-1 satellite data from the late 1980s, 1995, 2000, 2005, and 2010 to generate a sequence of LULC maps of China every five years, which they used to investigate the spatiotemporal change patterns of LULC. However, these datasets have relatively low temporal frequency of acquisition. Finding cloud-free images to cover all of China may require imagery from several different years or a combination of data from different satellites. These problems may result in inconsistent periods of time in the analysis and biased results because of inconsistent data sources. Another remotely sensed data set that is particularly useful for such work is cloud-minimized multi-temporal composites (Holben 1986) derived from high temporal frequency images acquired at a coarse/moderate spatial scale (pixels 250 m or larger). This coarse/moderate spatial scale is better suited to the coarse scale typically used in climate modeling (e.g. 0.05° (approximately 5 km) or larger (Lawrence and Chase 2007)) compared to the finer scale sensors with global coverage, such as Landsat (Sexton et al. 2013, Kim et al. 2014). An example of a dataset generated from a moderate-scale sensor that has been used for climate work is the Moderate-resolution Imaging Spectroradiometer (MODIS) land cover type product (MCD12Q1) (Lawrence and Chase 2007). Unfortunately, however, global LULC data from MODIS is only available since 2001, thus limiting the time span that can be studied, an important consideration in climate studies.

Fortunately, there is a dataset with coarse spatial resolution and high temporal frequency that does provide global data for an extended period: NOAA Advanced Very

High Resolution Radiometer (AVHRR) imagery (James and Kalluri 1994). Often combined with MODIS data, AVHRR data have been widely used for monitoring land surface conditions at coarse scales (Andres, Salas and Skole 1994, Lunetta et al. 2006). The early AVHRR instruments had just 4 spectral bands, although this was later increased to 5 in some subsequent sensors (Tucker et al. 2005). One of the most important derived datasets from AVHRR data is based on the Normalized Difference Vegetation Index (NDVI), a normalized ratio of the visible red and near infrared spectral bands (Rouse Jr et al. 1974). Water is generally associated with negative NDVI values, bare soil with values near zero (Sabins and Lulla 1987), and vegetation with high positive values that are broadly indicative of the amount of photosynthesizing vegetation present (Dappen 2003).

There is a long history of using AVHRR imagery for continental (Townshend, Justice and Kalb 1987, Tucker, Townshend and Goff 1985) and even global scale mapping (DeFries and Townshend 1994, DeFries, Hansen and Townshend 1995, Loveland et al. 2000, Hansen et al. 2000). For example, Gitas et al. (2004) used AVHRR imagery to map burned areas in the Spanish Mediterranean coast region after a large forest fire. More recently, Zhang et al. (2016) generated a global climatic vegetation map from AVHRR imagery. These studies typically used NDVI data alone, or in combination with reflectance values in each spectral band as well as temperature variables from the AVHRR thermal bands. However, in a study of the importance of different variables in discriminating classes for producing a global land cover map using AVHRR, DeFries et al. (1995) found summary metrics describing NDVI phenology were by far the most important for most vegetation classes. Nevertheless, for LULC classes for which vegetation phenology is of limited diagnostic use, such as the urban, snow, water, and barren classes, ancillary data such as digital cartographic information was found to be necessary (e.g. Loveland et al. (2000)). Significantly, these early efforts focused on producing single maps, and to our knowledge, AVHRR data has not yet been used to produce a time series of LULC maps over broad regions. In recent years less attention has been paid to AVHRR data classification due to the availability of improved, higher signal to noise, and higher spatial resolution remotely sensed data, such as from MODIS

(Schneider et al. 2009; Muhammad et al. 2015). However, AVHRR data comprise the longest global image time-series, and thus provide the potential to generate a long-term time-series of LULC maps, a key input for climatological analysis.

The aim of this study is to produce annual land use and land cover maps of Mainland China for the three decades covering the period from 1982 to 2013. The maps are produced based on a random forest classification using phenological metrics derived from the AVHRR Global Inventory Modeling and Mapping Studies (GIMMS) NDVI third generation (NDVI3g) dataset and trained using land cover information from the MODIS MCD12Q1 data set. The key attribute of our classified land cover maps is that they comprise a continuous time series covering three decades, which contrasts with the limited temporal information previously available for use in climate studies.

2.2   Data and Methods

2.2.1   Data
The primary dataset in this study is AVHRR GIMMS NDVI3g, first version, with data covering the period from 1982 to 2013, which were acquired from https://nex.nasa.gov/nex/projects/1349/. GIMMS NDVI3g data have been normalized to account for issues such as sensor calibration loss, orbital drift, and atmospheric effects such as volcanic eruptions (Pinzon and Tucker 2014). The spatial resolution of the data is 1/12°. Each layer in the dataset is a bimonthly (15 days) composite produced using the maximum NDVI value for each pixel (Holben 1986). We re-projected NDVI3g data onto a geographic grid, with WGS 1984 spheroid.

The second major dataset used is MODIS MCD12Q1 collection 5 data (Channan, Collins and Emanuel 2014), which we utilized as a reference source for identification of training areas and class labels for the AVHRR classification. The MODIS MCD12Q1 data with a WGS 1984 spheroid were obtained from University of Maryland http://glcf.umd.edu/data/lc/. The data comprise annual maps of land use classes keyed to the International Geosphere-biosphere Programme (IGBP) classification system, covering the period 2001 to 2012. MODIS MCD12Q1 collection 5 data are generated from

MODIS bands 1-7 and enhanced vegetation index data using an ensemble supervised classification algorithm (Friedl et al. 2010). The original MODIS MCD12Q1 data were resampled by the University of Maryland to 1/12° pixels, the resolution of the AVHRR GIMMS NDVI3g dataset, using a majority aggregation method (Channan et al. 2014). In this approach, each new pixel was labeled as the class that most frequently occurred in the original resolution data, for the area encompassing that new pixel.

The Chinese Land-Use/cover (CLU) dataset for 1995, 2000, 2005, and 2010 were obtained from the Data Center for Resources and Environmental Sciences (RESDC), Chinese Academy of Sciences (http://www.resdc.cn). CLU data were compared with our classified LULC maps in order to assess the 32-year time series of LULC dataset more robustly. The CLU data are produced mainly from 30 m Landsat TM data, as well as 30 m Huangjing-1 satellite imagery and 20 m China-Brazil Earth Resources Satellite-1 imagery using a human-computer interactive interpretation method (Liu et al. 2003a; Liu et al. 2010; Liu et al. 2014). The CLU data have 6 classes: cropland, woodland, water body (which includes water, snow, and ice), built-up land, and unused land. The accuracy of the six classes of land use is about 94.3% (Liu et al. 2014). RESDC provides the CLU data with spatial resolution of 1 km. To be consistent with our classified maps, we resampled the data to 1/12° spatial resolution, using a majority aggregation approach.

2.2.2 Data pre-processing

Although the temporal compositing process used in producing the NDVI3g dataset greatly reduces cloud and other atmospheric effects, residual noise remains (de Jong et al. 2011, Reed et al. 1994). Cleaning and smoothing NDVI data is therefore necessary (**Figure 2.1**) (A second version of GIMMS NDVI3g dataset, including data up to 2015, has recently been made available. However, this new dataset is not directly compatible with the original dataset, and for that reason, we did not incorporate the new data. Specifically, the binary VI3g data format of the first version was changed to the Network Common Data Form (NetCDF) for the second version, and the 1 to 7 range of the quality flag for the first version was adjusted to 0 to 2 for the second version.)

8
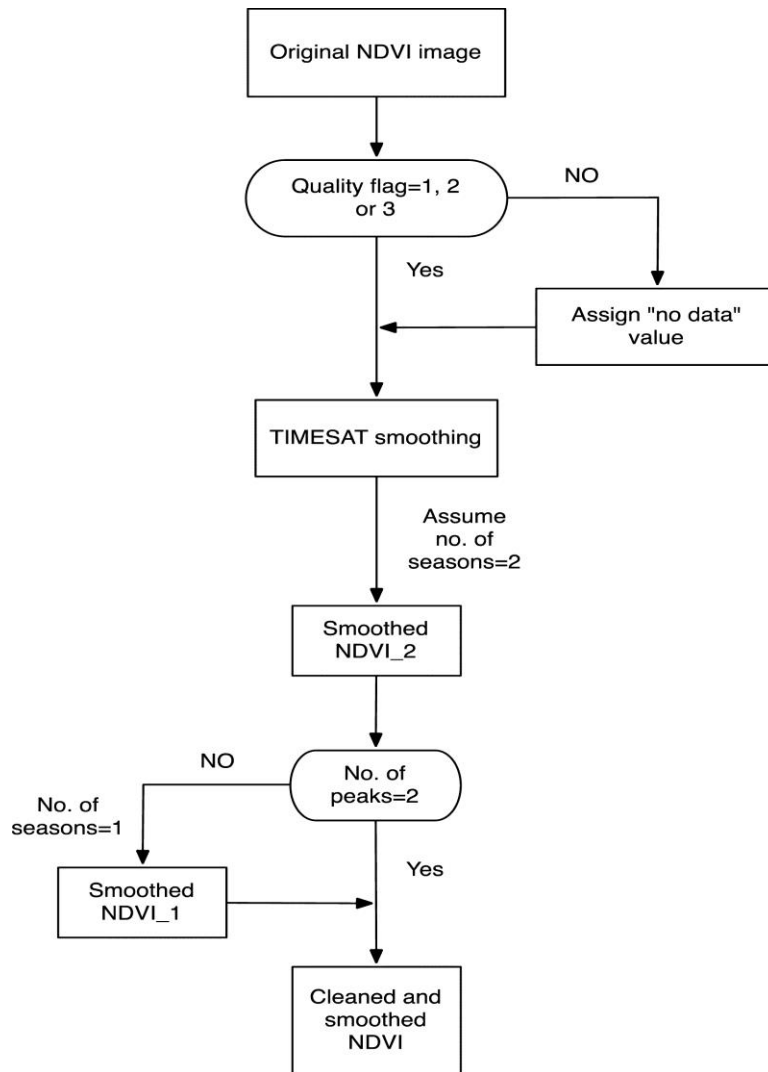
Figure 2.1. Flowchart for pre-processing the GIMMS NDVI3g data.

1) *Cleaning AVHRR GIMMS NDVI3g data-* The quality information flags for NDVI3g
   data range from 1 to 7. Flag values of 1 and 2 represent good data, 3 indicates the
   application of a spline interpolation (i.e. a data gap that has been filled), 4 and 6
   indicate possible snow, 5 indicates a gap filled through averaging the seasonal
   profile, and 7 indicates missing data. We retained data with flag values of 1, 2, and 3,
   following Chen et al. (2016), and excluded data with flag values of 4 to 7 by
   assigning those locations a "no data" value.

2) *Smoothing the cleaned AVHRR GIMMS NDVI data*- Even after removing pixels that are flagged as having low quality, smoothing is required to reduce the noise. This was done using the program TIMESAT (Jönsson and Eklundh 2002, Jönsson and Eklundh 2004). TIMESAT is a software package for analyzing time-series of satellite sensor data and available from http://web.nateko.lu.se/timesat/timesat.asp. Numerous studies have employed TIMESAT for phenological analysis (Palacios-Orueta et al. 2012, Boyd et al. 2011, Heumann et al. 2007, Palmer et al. 2015). TIMESAT offers multiple outlier removal methods: median filtering, approaches using weights from the Seasonal-Trend decomposition procedure based on Loess (STL)-decomposition (Cleveland et al. 1990) or weights from STL-decomposition multiplied with the original weights assigned based on the ancillary data, and three smoothing functions (a Savitzky-Golay filter, an asymmetric Gaussian filter, and a double logistic smoothing function) (Jönsson and Eklundh 2004). Following Lee et al. (2015), we selected median filtering to remove outliers that deviate more than two standard deviations from the median in a moving window (Eklundh and Jönsson 2015) and the double logistic method to smooth the time-series.

TIMESAT smoothing requires the user to specify the number of growing season per year. In China, two growing seasons are common in some locations (e.g., cropland areas in Southern China), and only one growing season predominates elsewhere (e.g., deciduous forest and cropland in Northern China). In order to identify the appropriate number of seasons, we first smoothed the entire NDVI time-series with two growing seasons (Smoothed NDVI_2) (Figure 1). Each resulting smoothed time-series was checked to determine if there were at least four points of increasing NDVI before the NDVI peak (i.e., where the first derivative is zero) and four points of decreasing NDVI points after the peak, in each year. We chose these criteria as the potential growing season for cropland in China is approximately four months. If the time-series for a particular year did not meet these criteria, it was replaced with a smoothing based on the assumption of a single growing season (Smoothed NDVI_1) (Figure 1).

For the time series of a single pixel, any year with missing data that comprises a continuous period longer than 0.2 years, is not smoothed by TIMESAT. Similarly, the entire 32 year time-series for any pixel is also not smoothed if 25% of the data is missing (Gao et al. 2008). These pixels were labeled "no data" in our classified LULC maps, and cover 3.7% of the area of China.

Figure 2.2 displays the spatial patterns of cleaned, and cleaned and smoothed NDVI for Julian day 75 of 2011 as an example. Pixels with flag values 4 to 7, which were excluded in the cleaning processes, are mostly found in Northeast China and Western China, as shown in white in **Figure 2.2 (a)**. The smoothing processes discussed above improves the completeness of the NDVI, reducing, but not entirely eliminating, the number of no data pixels, as shown in **Figure 2.2 (b)**. This is due to the limitation of TIMESAT, as mentioned above.

(a)   (b)
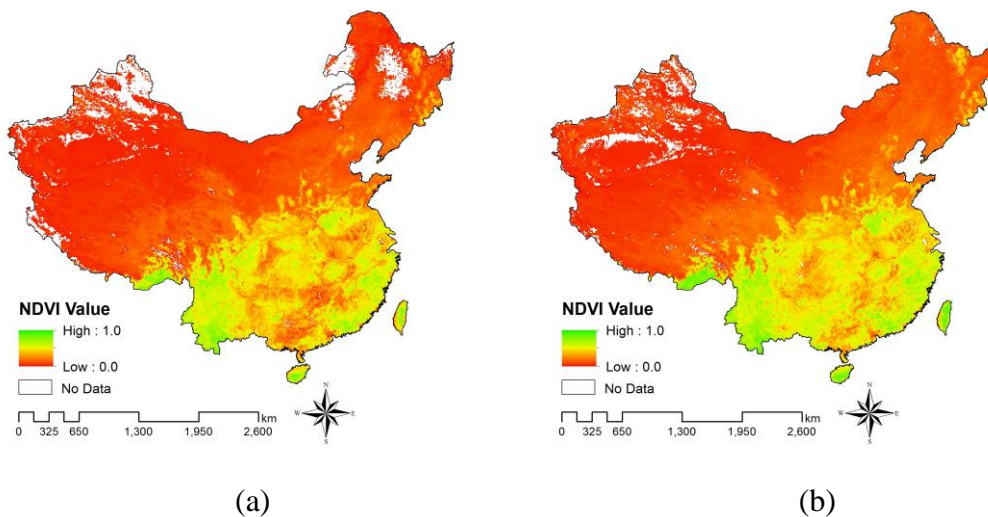
Figure 2.2. Spatial patterns for Julian day 75 of 2011 of (a) cleaned and (b) cleaned and smoothed NDVI.

Figure 2.3 displays the raw NDVI and cleaned and smoothed NDVI time-series for a single year of randomly selected individual pixels from Northeast China representing mixed forest, croplands, and grasslands. After cleaning and smoothing, the NDVI profiles provide generalized overall patterns of the NDVI time-series.

11
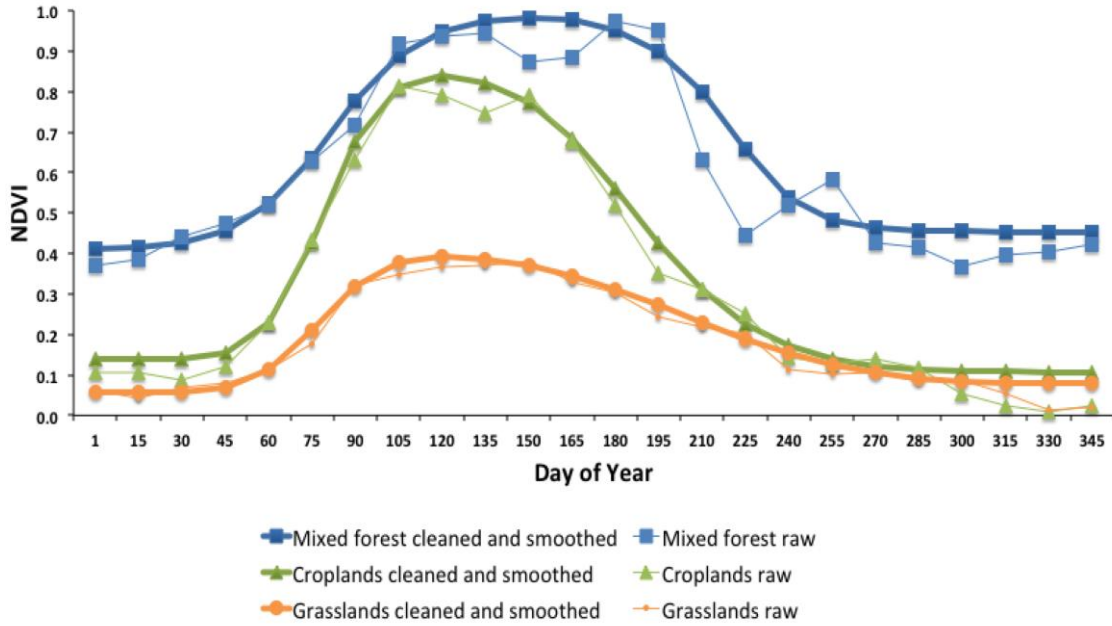
Figure 2.3. Raw, and cleaned and smoothed NDVI time-series of mixed forest, croplands, and grasslands.

2.2.3 Land use and land cover classification methods

Pixels identified as having two growing seasons (as described in section 2.2) were directly labeled as croplands, since natural vegetation should have only one growing season. The remaining pixels, which comprise those with one growing season, were classified following the procedures in **Figure 2.4**.
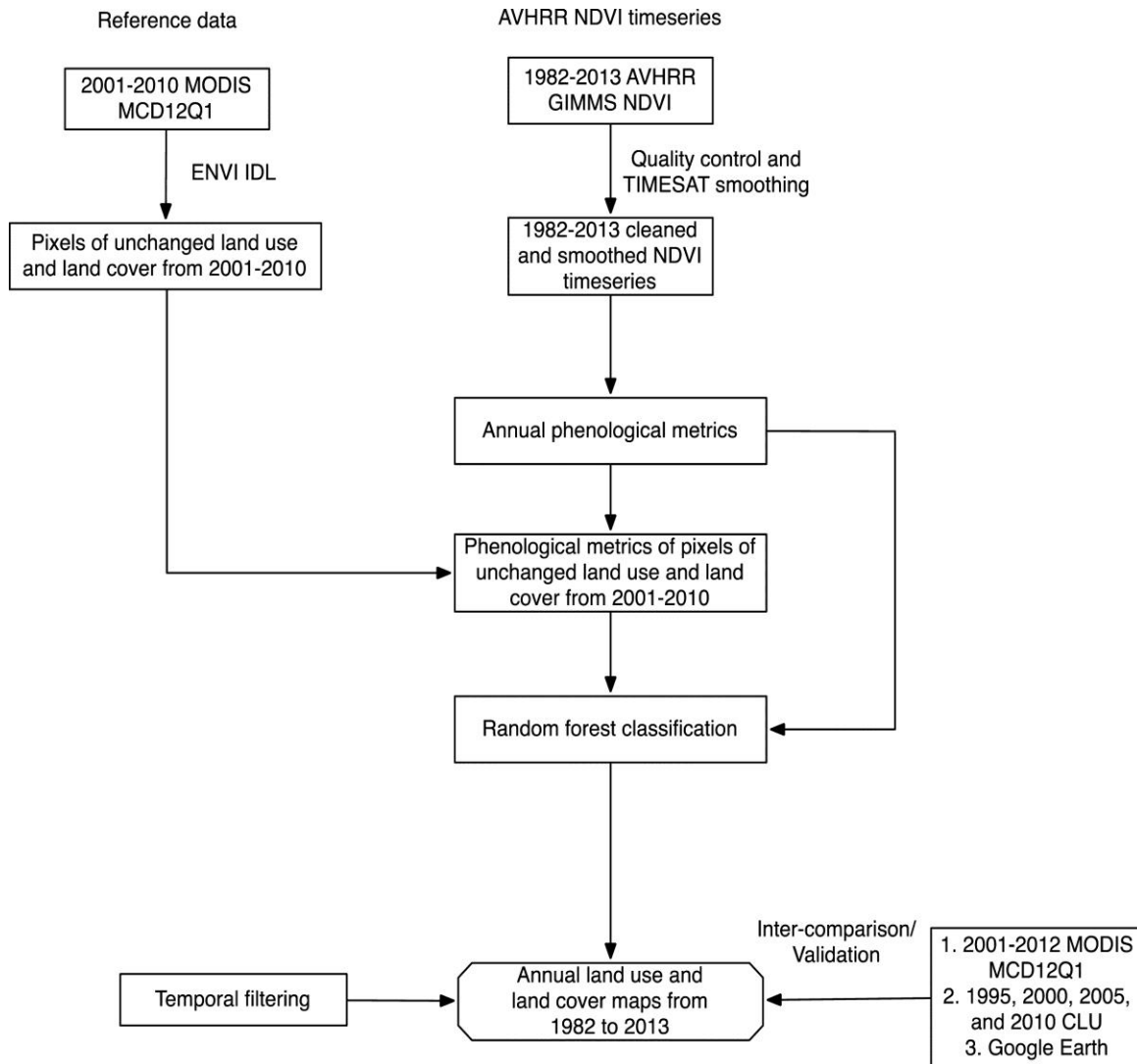
Figure 2.4. Flowchart of the land use and land cover classification approach.

2.2.3.1 *Classification*

Our aim in selecting a method for obtaining training data for the classification was to develop a method that provided many examples of each land cover class, from multiple years, in order to capture both geographic and temporal variability. We therefore used as a reference data source pixels of unchanged land cover during the period from 2001 to 2010 in the MODIS MCD12Q1 dataset (**Figure 2.4**). The reference data were randomly split, with 25% used as training data (25%) and the remaining 75% used as validation data (75%) for an initial evaluation of the classification.

Prior to carrying out the classification, China was divided into four separate regions generally based on vegetation zones, as suggested by Hou (1981) (Figure 5), and each region was classified separately. This segmentation was applied because the characteristics of phenological patterns of the mapping classes vary geographically. For example, croplands in Central and Southern China may have two growing seasons and spring green-up occurs typically in March, while croplands in Northeast China only have one growing season and green-up occurs only in May (Wu et al. 2010). Similarly, natural vegetation spring green-up occurs later, moving from south to north (Zhang, Friedl and Schaaf 2006). The boundaries of the sub-regions were chosen along arbitrary N-S and E-W lines, and not along previously mapped ecological boundaries. Our choice for doing so reflected our philosophical concern not to impose a simple view of sharp ecotonal boundaries that have not moved over the more than three decades of the study. An added advantage of using simple, relatively arbitrary sub-region boundaries is that it made for simpler processing, which could potentially easily be applied to the production of a global map, where the issue of identifying simple sharp ecotonal boundaries between regions would be even more problematic. A potential drawback with our approach as it perhaps increases the chance for classification inconsistencies across the sub-region boundaries.

The four zones chosen were: Western China, Northeast China, Central China, and Southern China. In Western China, barren or sparsely vegetated land and grasslands dominate, with some minor croplands. In Northeast China, the main vegetation types are grasslands, croplands, and mixed forest. In Central China, the dominant classes are barren or sparsely vegetated, grasslands, and croplands. Southern China has the most diverse vegetation types, including grasslands, croplands, forest, and savanna (**Figure 2.5**).

14
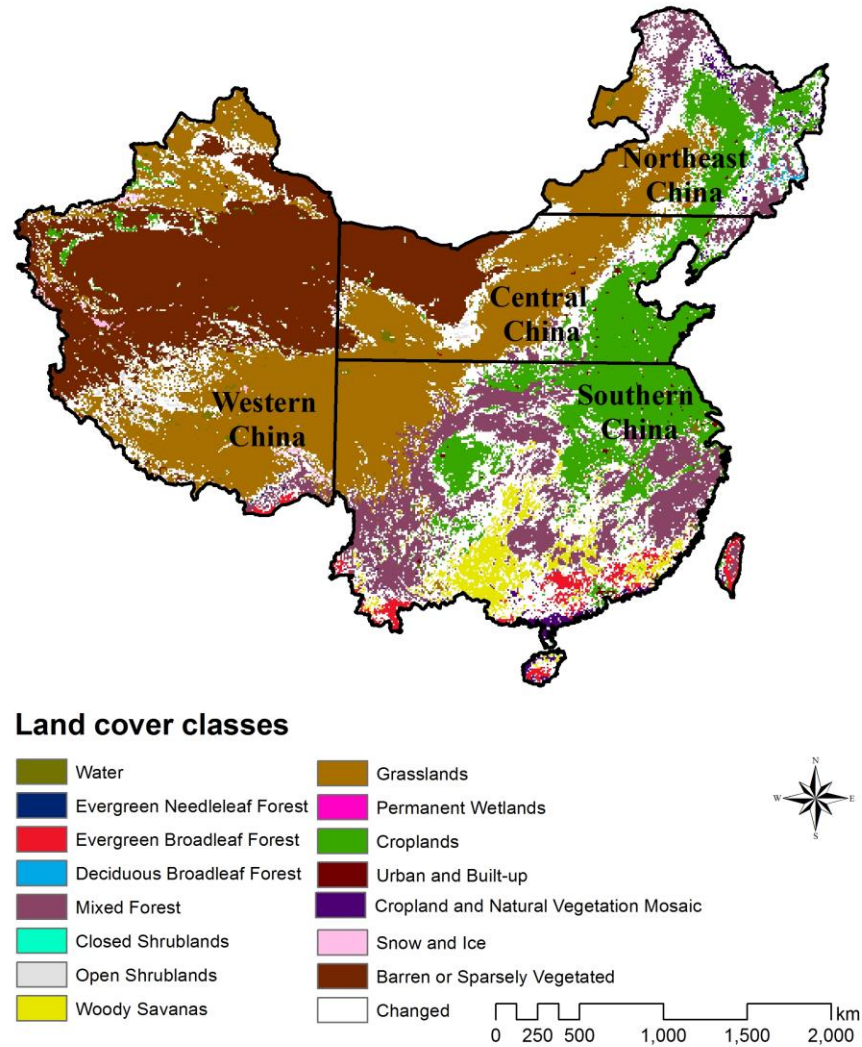
Figure 2.5. Unchanged pixels of LULC for Mainland China, 2001 to 2010 derived from MODIS MCD12Q1, and used for training the random forest classifier.

The numbers of pixels for each unchanged LULC type in each region are shown in **Table 2.1**. For some LULC types, the numbers of pixels are zero or close to zero. For example, there are no unchanged pixels in the deciduous needleleaf forest class and only two pixels of permanent wetlands and closed shrublands. These LULC types of limited extent were excluded from further analysis, reducing the original 17 classes down to 13 LULC classes that were mapped (**Table 2.1,** class for AVHRR classification).

Table 2.1. Number of pixels for each unchanged LULC type in each region in China. These pixels were randomly split, with 25% used for training, and 75% for validation.

MODIS MCD12Q1 Class	Number of pixels				Class for AVHRR classification
	Western	**Northeast**	**Central**	**Southern**	
Water	313	60	135	260	Water
Evergreen Needleleaf Forest	20	0	0	0	Evergreen Needleleaf Forest
Evergreen Broadleaf Forest	141	0	0	1432	Evergreen Broadleaf Forest
Deciduous Needleleaf Forest	0	0	0	0	
Deciduous Broadleaf Forest	0	117	75	0	Deciduous Broadleaf Forest
Mixed Forest	496	2702	1832	10032	Mixed Forest
Closed Shrublands	0	0	2	0	
Open Shrublands	210	0	43	0	Open Shrublands
Woody Savannas	0	1	0	2949	Woody Savannas
Savannas	0	0	0	0	
Grasslands	16062	5387	12530	3628	Grasslands
Permanent wetlands	0	0	0	2	
Croplands	450	3947	7751	6177	Croplands
Urban and Built-up	4	25	138	233	Urban and Built-up
Cropland and Natural Vegetation Mosaic	7	556	102	521	Cropland and Natural Vegetation Mosaic
Snow and Ice	432	0	1	5	Snow and Ice
Barren or Sparsely Vegetated	23881	0	5159	0	Barren or Sparsely Vegetated

The cleaned and smoothed 1982-2013 AVHRR GIMMS NDVI dataset (section 2.2) was used to generate a total of 19 phenological metrics (**Table 2.2**), including start of growing season, end of growing season, and maximum and minimum NDVI values, for each pixel. Maximum and minimum NDVI value, Julian day of maximum and minimum NDVI value, NDVI value of start and end of season, and Julian day of start and end of the season are commonly used phenological variables for land cover characterization

(Knight et al. 2006; Vuolo et al. 2011; Xue et al. 2014; Yan et al. 2015) because they capture the gross pattern of the annual NDVI cycle. For instance, in **Figure 2.3**, the maximum NDVI value is greatest for mixed forest, followed by croplands, and then grasslands, which have the lowest value. The Croplands in **Figure 2.3** are distinguished by an earlier green-up than mixed forest and grasslands. Additional key summary metrics were generated from integrated NDVI values. According to Liu et al. (2015) and Vuolo et al. (2011), integrated phenological metrics are important in classifying crops, thus we included several integrated values, such as the integral under the NDVI curve, and the integral between start season and maximum value. Other metrics, for example those based on the maximum and minimum derivative of the NDVI curve, were chosen in order to capture properties related to the rate and timing of phenological change, such as green-up (DeFries and Townshend 1994, Nellis, Price and Rundquist 2009).

Table 2.2. The 19 phenological metrics used as input for the random forest classification

Phenological Metrics
1: Maximum NDVI value
2: Minimum NDVI value
3: Julian day of maximum NDVI value
4: Julian day of minimum NDVI value
5: Integral of NDVI between Day 105 and Day 315
6: Integral under the NDVI curve
7: Maximum derivative of NDVI curve
8: Minimum derivative of NDVI curve
9: Julian day of maximum derivative of NDVI curve
10: Julian day of minimum derivative of NDVI curve
11: Julian day of start season
12: Julian day of end season
13: NDVI value of start season
14: NDVI value of end season
15: Integral between maximum derivative and minimum derivative
16: Integral between start season and maximum value
17: Integral between end season and maximum value
18: Maximum NDVI value − minimum NDVI value
19: Maximum NDVI value/ Integral under the NDVI curve

Classification was carried out using the R randomForest package (Liaw et al. 2009). Ensemble learning algorithms such as random forests have received increasing attention, because they are simple to implement, with few user-specified parameters, tend

not to be sensitive to noise or overtraining, and therefore do not need pruning, and are generally found to be more robust than single classifiers (Rodriguez-Galiano et al. 2012). The random forest classifier consists of a combination of a large number of classification trees, which "vote" to produce a single outcome for each pixel (Breiman 2001). Each individual tree is generated from a random subset of the training data, as well as a random subset of the variables. In this way, the individual trees have reduced accuracy, but also reduced correlation, resulting in a more reliable overall classification. The random forest classifier can handle thousands of variables without variable deletion (Rodriguez-Galiano et al. 2012), and can even be applied when the number of variables is much larger than the number of samples (Dahinden 2011). A further benefit is that the classifier provides an estimate of the importance of each variable by summarizing the accuracy of trees that don't use that variable. The random forest classifier (Breiman 2001) has been widely used in many fields, including remote sensing (Cutler et al. 2007, Speiser, Durkalski and Lee 2015, Baudron et al. 2013, Maxwell and Warner 2015, Maxwell, Warner and Strager 2016). Random forest classification requires two user-defined parameters: the number of decision trees produced (*ntree*) and the number of variables available for splitting at each node (*mtry*). In general, the value of *ntree* simply has to be large enough to give a stable result; we chose a value of 500 based on prior experience (Maxwell et al. 2016). For *mtry*, we chose the default value, in the randomForest package (Liaw et al. 2009), the square root of the number of predictor variables (i.e., 4), following Liu et al. (2016), though Shi and Yang (2016) advocate for a larger number of variables, combined with a smaller number of trees. The importance of the 19 phenological variables was measured using the mean decrease in accuracy (MDA) derived from the random forest classifier. The larger mean decrease in accuracy means the more the accuracy of the random forest decreased due to the exclusion of a variable, thus the greater the assumed importance of that variable (Breiman 2001). Separate random forest classifications were generated to map the LULC for each of the four regions.

2.2.3.2 Temporal filtering

In order to try to improve the overall quality of the map time series, short-term, unreasonable land cover transitions were identified and suppressed (Clark et al. 2010, Baker et al. 2013). For example, it would be unlikely that a forested pixel would be converted to urban cover, and then subsequently changed back to forest cover in the following year. Therefore, we used a temporal filter with a 3-year moving window to remove the disallowed land use and land cover transitions (Clark et al. 2010). Specifically, we tested to see if the classes from year n and $n+2$ were the same. If the classes were the same and class $n+1$ was a disallowed transition as specified by **Table 2.3**, then class $n+1$ was replaced with the class from year n.

Table 2.3. Allowed and disallowed class transitions

Class		Year n+1									
		Water	Forest	Open Shrublands	Woody Savannas	Grasslands	Croplands	Urban and Built-up	Cropland and Natural Vegetation Mosaic	Snow and Ice	Barren or Sparsely Vegetated
Year n and n+2	Water	Yes	No	No	No	No	No	No	No	No	No
	Forest	No	Yes[1]	No	No	No	No	No	No	No	No
	Open Shrublands	No	No	Yes	Yes	Yes	Yes	No	Yes	No	No
	Woody Savannas	No	No	Yes	Yes	Yes	Yes	No	Yes	No	No
	Grasslands	No	No	No	No	Yes	Yes	No	Yes	No	Yes
	Croplands	No	No	No	No	Yes	Yes	No	Yes	No	Yes
	Urban and Built-up	No	No	No	No	No	No	Yes	No	No	No
	Cropland and Natural Vegetation Mosaic	No	No	No	No	Yes	Yes	No	Yes	No	No
	Snow and Ice	No	No	No	No	No	No	No	No	Yes	No
	Barren or Sparsely Vegetated	No	No	No	No	Yes	No	No	No	No	Yes

[1]: Transitions of the same forest type: "Yes", transitions between different types of forest: "No"

2.2.3.3 *Inter-comparisons and accuracy evaluation*

To assess the reliability of the classified maps, we chose multiple approaches because the 32-year time series of land use and land cover maps represent such a complex dataset. These included inter-comparison with the validation data (75%), the entire 2001-2010 MODIS MCD12Q1 LULC maps (years that were used in training the classifier), as well as the entire MODIS MCD12Q1 LULC maps for 2011 and 2012 (years that were excluded from the reference data set), and the 1995, 2000, 2005, and 2010 CLU data. In addition, we undertook a more traditional error evaluation (Olofsson et al. 2014) using high resolution 2012 Google Earth images as a reference source.

We chose to compare our maps against the MODIS data in order to benchmark our approach against the input MODIS data. This comparison can potentially provide insight regarding how successful the AVHRR NDVI data are in reproducing the overall patterns as identified with MODIS, a sensor with superior spectral and radiometric resolution (Tucker et al. 2005). We compared our maps with CLU dataset, because it was a typical LULC dataset of China generated from high resolution imageries, such as Landsat and Huanjing -1 data. The CLU dataset has a classification system that differs from ours, as mentioned in section 2.1. Thus, we combined our classes of evergreen needleleaf forest, evergreen broadleaf forest, deciduous broadleaf forest, mixed forest, open shrubland, and woody savannas, into a single forest class; water and snow and ice into the water class; and croplands and the cropland and natural vegetation mosaic into the croplands class (Table 4, see column "class for comparing with CLU data"). It is important to note, however, that the inter-comparisons with MODIS and CLU data are not an accuracy evaluation, since the MODIS and CLU data themselves have errors. For example, the global overall accuracy of MODIS MCD12Q1 has been estimated as approximately 75% (Zhao et al. 2013).

Table 2.4. Class for comparing with CLU data

Class for comparing with CLU data	Class for AVHRR classification
Water	Water Snow and Ice

21

Forest	Evergreen Needleleaf Forest
	Evergreen Broadleaf Forest
	Deciduous Broadleaf Forest
	Mixed Forest
	Open Shrublands
	Woody Savannas
Grasslands	Grasslands
Croplands	Croplands
	Cropland and Natural Vegetation Mosaic
Urban and Built-up	Urban and Built-up
Barren or Sparsely Vegetated	Barren or Sparsely Vegetated

Comparisons with other land cover classifications provide useful insight into the similarities of the results with different sensors. However, only an assessment using independent reference data can provide an estimate of the map accuracy. We therefore undertook an accuracy evaluation using a manual interpretation of Google Earth imagery, focusing on land cover for the year 2012. This year was chosen because there were relatively abundant images in Google Earth for that year, and also this was a year not used in training the random forest classifier used to produce the AVHRR LULC maps.

A random sampling strategy with stratification was chosen to select sample points (Olofsson et al. 2014). The strata were the mapped classes. Based on multinomial sampling theory, we estimated a minimum of 150 random samples would be required in order to generate an estimate with 10% precision and 15% confidence (Jensen 2016). An initial random sample of 300 sample points with a minimum of 15 points for each stratum was selected across the study area. Sample points for the final analysis after points without appropriate high resolution imagery for 2012 in Google Earth were removed, leaving a final total of 256 points, many more than the 150 points we set as a minimum. Although we had concerns that only using locations for which 2012 imagery was available might introduce bias, there was no obvious pattern to the availability of such imagery.

A visual estimate was made of the dominant land cover within a 1/12° x 1/12° square, representing the AVHRR pixel dimensions, which was drawn around each sample point in Google Earth. Because it was not always possible to visually differentiate

between all classes, we combined evergreen needleleaf forest, evergreen broadleaf forest, deciduous broadleaf forest, mixed forest, open shrubland, and woody savannas to form a single forest class (Table 5, class for Google Earth validation). Thus, although the original map has 13 classes, the accuracy evaluation is based on only eight of those classes, and therefore the accuracy we estimated is for a simplified map that does not differentiate forest classes. The accuracy of the map with the original 13 classes will of course be lower than that of the eight classes map we evaluated.

Table 2.5. Class for Google Earth validation

Class for Google Earth validation	Class for AVHRR classification
Water	Water
Forest	Evergreen Needleleaf Forest Evergreen Broadleaf Forest Deciduous Broadleaf Forest Mixed Forest Open Shrublands Woody Savannas
Grasslands	Grasslands
Croplands	Croplands
Urban and Built-up	Urban and Built-up
Cropland and Natural Vegetation Mosaic	Cropland and Natural Vegetation Mosaic
Snow and Ice	Snow and Ice
Barren or Sparsely Vegetated	Barren or Sparsely Vegetated

Because the sampling design is stratified random using the map classes as strata, the cell entries of the error matrix are estimated using (Olofsson et al. 2014):

$$P_{ij} = W_i \frac{n_{ij}}{n_{i+}} \tag{1}$$

Where P_{ij} denotes the proportion of area for the population that is class i according to the classification information, and class j according to the reference information. W_i is the proportion of area mapped as class i. n_{ij} is the number of samples in class i according to the classification, and class j according to the reference information. n_{i+} denotes the row totals.

Recent research has called into questioning the value of the kappa statistic (Pontius and Millones 2011), consequently we instead calculated allocation disagreement

and quantity disagreement, measuring which divide overall error into components related to errors in class location and proportion, respectively (Pontius and Millones 2011). Based on the error matrix generated from Eq. (1), the overall allocation disagreement (A) and overall quantity disagreement (Q) were calculated as follows (Pontius and Millones 2011; Warrens 2015):

$$a_i = 2\min(p_{i+}, p_{+i}) - 2p_{ii} \tag{2}$$

$$A = \frac{1}{2}\sum_{i=1}^{C} a_i \tag{3}$$

$$q_i = |p_{i+} - p_{+i}| \tag{4}$$

$$Q = \frac{1}{2}\sum_{i=1}^{C} q_i \tag{5}$$

Where C is the number of classes. p_{i+} and p_{+i} denote the row and column totals, respectively. a_i is the allocation disagreement for class i. q_i is the quantity disagreement for class i.

The same points were used to estimate the accuracy of our 2012 AVHRR map and the MODIS MCD12Q1 2012 map. McNemar's test (de Leeuw et al. 2006) was used to assess whether our classified LULC was significantly different from that of the MODIS classification.

2.3   Results and Discussion

2.3.1   Relative importance of 19 phenological metrics

The importance of the 19 phenological metrics as predictors measured using the mean decrease in accuracy of the random forest classifier is showed in **Figure 2.6**. It is notable that the lowest mean decrease in accuracy is approximately 18%, indicating all the metrics appear to be useful for all regions, and that there is not a great deal of redundancy in the 19 metrics. This finding is most evident for Southern China, where excluding any single metric seemed to have a particularly large effect (no less than 30% mean decrease in accuracy). The other major observation from **Figure 2.6** is that there is little consistency in the importance of individual metrics for the different regions of China. However, in general, the most important metrics are Julian dates of phenological

events, such as the start of season (metric number 11), probably due to differences in the growth calendars of different vegetation cover types. For example, croplands start green-up earlier than mixed forest and grasslands (**Figure 2.3**). In Northeast China and Southern China, actual NDVI values are also important (e.g. the maximum NDVI value, metric number 1). As Northeast China and Southern China have mixed forest and other vegetation classes (**Figure 2.5**), maximum NDVI may differentiate less productive non-forest biomes from more highly productive forests. In Central China, the integral of NDVI over time (e.g. between the maximum value and the end of season, metric number 17) is also important. Barren or sparsely vegetated areas, grasslands, and croplands are dominant in Central China (**Figure 2.5**). Integrated NDVI values, such as integral between maximum value and the end of season, may separate croplands from other vegetation cover types, such as grasslands, since croplands are usually characterized by a high rate of green-up and senescence.
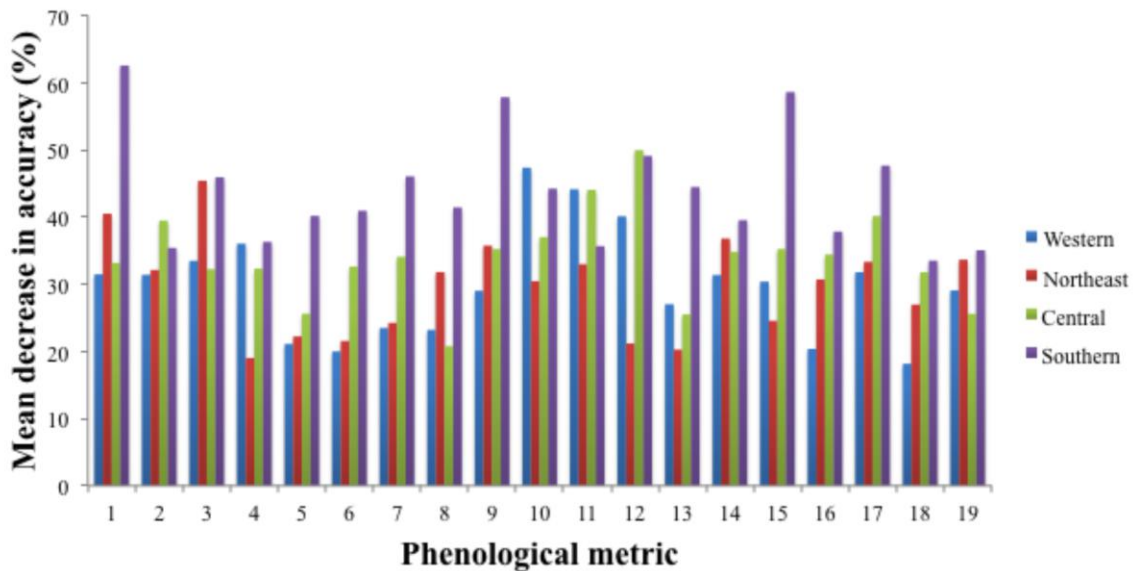
Figure 2.6. Relative importance of 19 phenological metrics as indicated by mean decrease in accuracy (larger values indicate higher importance). (See **Table 2.2** for associated metric for each metric number)

2.3.2 Temporal filtering of time-series of LULC maps

Comparing the classified maps before and after temporal filtering, the percentage of pixels replaced varies among different classes and years (**Figure 2.7**). Water,

evergreen needleleaf forest, deciduous broadleaf forest, open shrublands, urban and built-up, snow and ice, and barren or sparsely vegetated are replaced less than other classes, while mixed forest, woody savannas, grasslands, and croplands are replaced more frequently. This is likely due to the relatively large area of the latter classes.
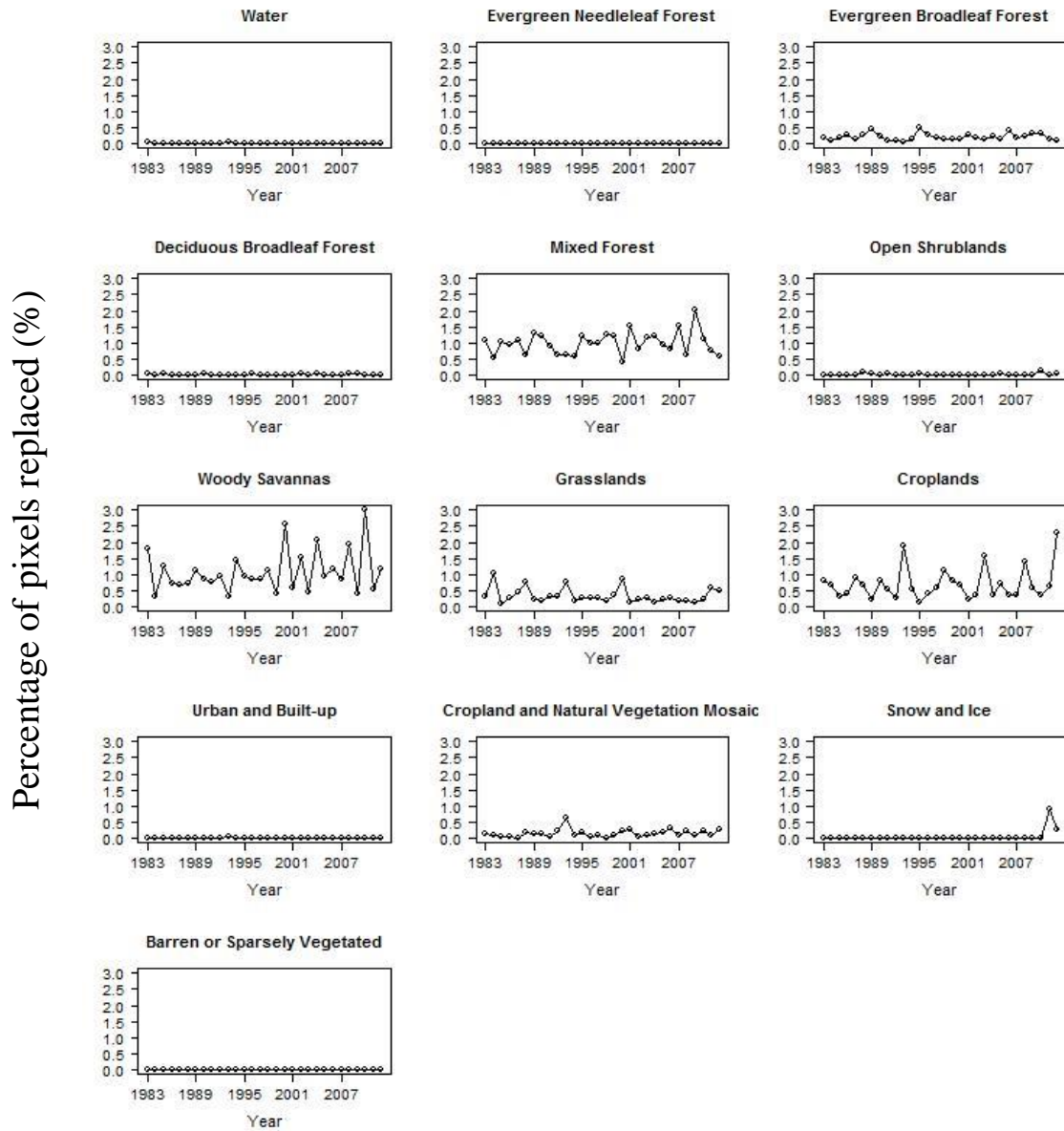
Figure 2.7. Percentage of pixels for each class for which the filtering operation changed the labeled class, per year from 1983 to 2012 (Note: the filtering operation does not affect the first and last year data, i.e., 1982 and 2013).

26

2.3.3 Inter-comparison and accuracy evaluation

In this section, we first evaluate the reliability of the AVHRR classifications. This is done by a comparison with the validation data (75%), and comparisons with the entire 2001-2012 MODIS classifications and 1995, 2000, 2005, and 2010 CLU data. These inter-comparisons with the validation data (75%) and MODIS data are based on 13 classes (i.e., the column "class for AVHRR classification" in **Table 2.1**), the inter-comparison with the CLU data is based on six classes (i.e., the column "class for comparing with CLU data" in **Table 2.4**). After these comparisons, we then report the results of the more traditional accuracy evaluation, which is based on the eight classes in the column "class for Google Earth Validation" in **Table 2.5**. After the accuracy evaluation we summarize the geographic and temporal trends in the 32-year time series in the following section. The focus of temporal trend analysis is on the areas of land cover classes in individual date and not change maps.

2.3.3.1 Inter-comparison of classified LULC with validation data (75%)

The user's accuracy and producer's accuracy vary among different classes and different regions (**Table 2.6**). It is apparent that the user's and producer's accuracies tend to be lower for most classes in Southern China compared to the other regions, possibly a result of cloud contamination. Some classes, for example, the barren or sparsely vegetated, grasslands, and mixed forest, are consistently mapped with relatively high accuracy (defined as here as greater than 75% user's and producer's accuracies). In contrast, water and evergreen needleleaf forest are mapped generally (though not always) with lower reliability (user's and producer's accuracies less than 50%). It is notable that the classes with higher accuracies, such as mixed forest, tend to cover larger areas, and thus have larger number of training samples (**Table 2.1**). The overall accuracy of validation data (75%) is also shown in **Table 2.6**. All of regions have high accuracy (>91%), except for southern China, which has 79.0% overall accuracy.

Table 2.6. Random forest user's accuracy (UA), producer's accuracy (PA), and overall accuracy for each region based on the validation data (75%).

	Western China		Northeast China		Central China		Southern China	
	UA	PA	UA	PA	UA	PA	UA	PA

Water	44.4%	2.1%	66.7%	8.3%	75.0%	5.3%	25.0%	3.2%
Evergreen Needleleaf Forest	25.0%	7.1%						
Evergreen Broadleaf Forest	76.0%	51.4%					64.2%	46.4%
Deciduous Broadleaf Forest			42.6%	29.9%	85.7%	20.7%		
Mixed Forest	76.5%	79.0%	89.0%	97.9%	85.0%	89.9%	79.1%	88.4%
Open Shrublands	40.0%	3.8%			100.0%	3.6%		
Woody Savannas							66.9%	58.1%
Grasslands	89.3%	92.9%	94.9%	97.2%	94.0%	96.6%	85.4%	86.5%
Croplands	71.5%	50.0%	91.7%	89.2%	92.9%	92.5%	85.3%	84.6%
Urban and Built-up			50.0%	5.9%	25.0%	1.0%	52.4%	15.4%
Cropland and Natural Vegetation Mosaic			62.8%	37.4%	63.0%	22.4%	55.4%	37.0%
Snow and Ice	66.7%	3.5%						
Barren or Sparsely Vegetated	93.6%	94.9%			96.7%	95.5%		
Number of validation pixels	28502		9518		19653		16518	
Overall Accuracy	91.4%		91.5%		93.5%		79.0%	

2.3.3.2 Inter-comparison of classified LULC with MODIS MCD12Q1

The comparison of our classification with the entire MODIS MCD12Q1 maps for the years not used in training the classifier (2011 and 2012) indicates a consistency of 71.0% for 2011, and 69.3% for 2012. Inconsistency is high in Northeast China and Southern China (**Figure 2.8**), whereas the two datasets are generally much more consistent in Western China. It is notable that the areas of inconsistent land cover are common where cloud cover is more frequent, including parts of the humid Southeastern China, and some of the relatively mountainous regions of Northeastern and Western China, as well as the places where land use and land cover change appears to be more common. However, for the Tibetan Plateau, inconsistent regions are more common on

the edges of the region than the interior. This may be due to the fact that the interiors of region tend to be dominated by more homogenous LULC (e.g., grasslands), while the edges of the region are transitional areas for different LULC type. For example, in Southeast edge of Tibetan Plateau, mixed forest and grasslands coexist. Furthermore, the inconsistency between these two land use and land cover datasets may be also related to the different data sources (i.e., NDVI in this study and reflectance of bands 1-7 in MCD12Q1) and methodologies (i.e., random forest in this study and ensemble supervised classification algorithm in MCD12Q1) for producing these two datasets.

(a)   (b)
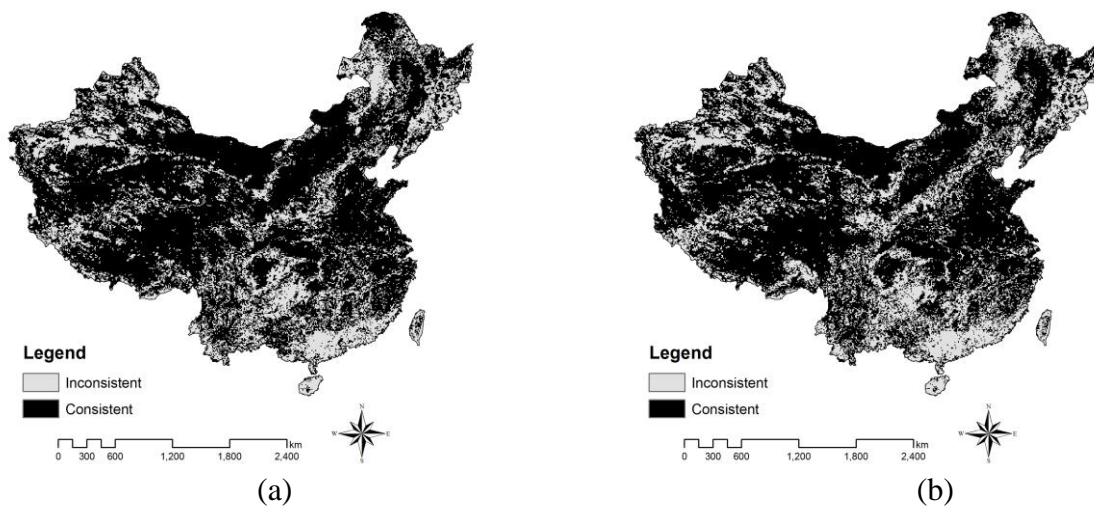
Figure 2.8. Comparisons of the classified LULC maps with MODIS MCD12Q1 in (a) 2011 and (b) 2012.

Notably, the consistency values for 2011 and 2012 are only slightly lower than the average of the consistency values observed for 2001-2010, years that were used for training the classifier (**Figure 2.9**). This result is encouraging, because it provides some evidence that the classifier is able to extrapolate to years other than those used in training. If the training data, or the classifier, were not adequate to capture the overall patterns, we would expect a much greater drop in years not used in training, when the annual patterns of rainfall or temperature, for example, might be slightly different than the years used for training.
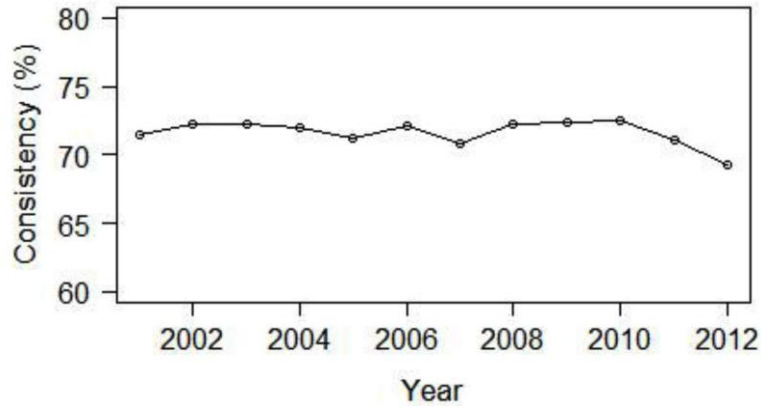
Figure 2.9. Consistency between classified LULC maps and MODIS MCD12Q1 from 2001 to 2012.

To further explore the consistency for different classes between these two LULC datasets, we display a time-series of user's consistency (calculated as the consistent pixels for class i / all pixels for class i in our classified map) and producer's consistency (calculated as the consistent pixels for class i / all pixels for class i in MODIS data) for each class from 2001 to 2012 (**Figure 2.10**). The classes with the highest user's and producer's consistencies for each year tend to be those of mixed forest, woody savannas, grasslands, croplands, and barren or sparsely vegetated. This may be due to the better performance of the random forest classification for the classes with a larger number of training samples (**Table 2.1** and **Table 2.6**). The classes with the lowest consistencies are water, evergreen needleleaf forest, evergreen broadleaf forest, deciduous broadleaf forest, open shrublands, urban and built-up, and snow and ice.
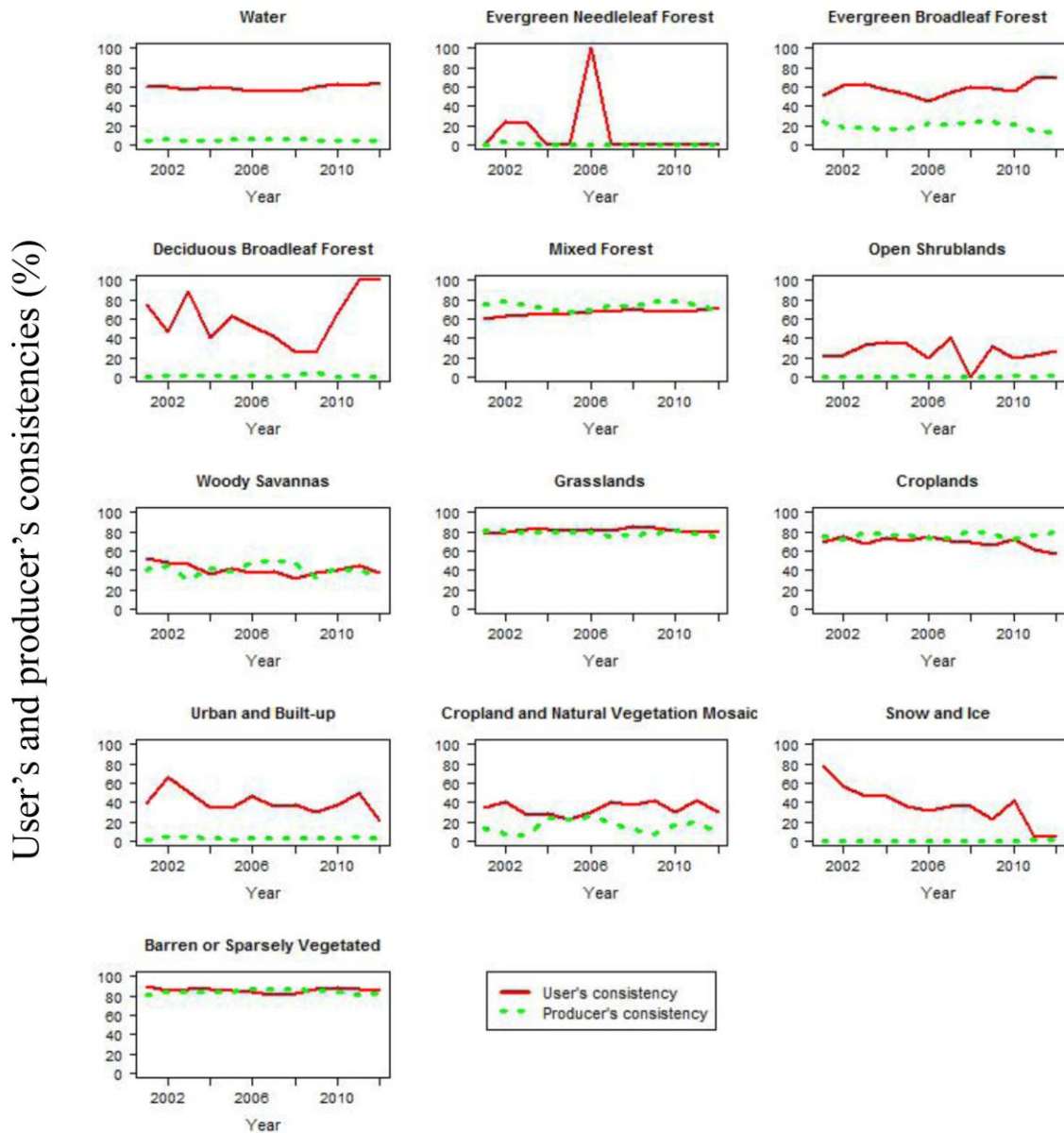
Figure 2.10. User's and producer's consistencies for each class between classified LULC maps and MODIS MCD12Q1 from 2001 to 2012.

2.3.3.3 *Inter-comparison of classified LULC with CLU dataset*

The overall consistency values between our classified LULC and the CLU dataset, for years 1995, 2000, 2005, and 2010, are 64.3%, 64.3%, 63.0%, and 64.4%, respectively. Compared to the consistency values of our classified LULC maps and MODIS MCD12Q1, the consistency values for the CLU maps are generally lower. The

very different spatial resolutions (i.e., 30 m for original CLU maps and 1/12° for our classified LULC maps) and different classification systems may have contributed to the lower consistency values.

Figure 2.11 summarizes the user's and producer's consistencies for our classified LULC and CLU maps for each class for 1995, 2000, 2005, and 2010, calculated as in Figure 2.10. Forest, grasslands, croplands, and barren or sparsely vegetated classes have relatively high consistencies, while water and urban and built-up have lower consistencies.
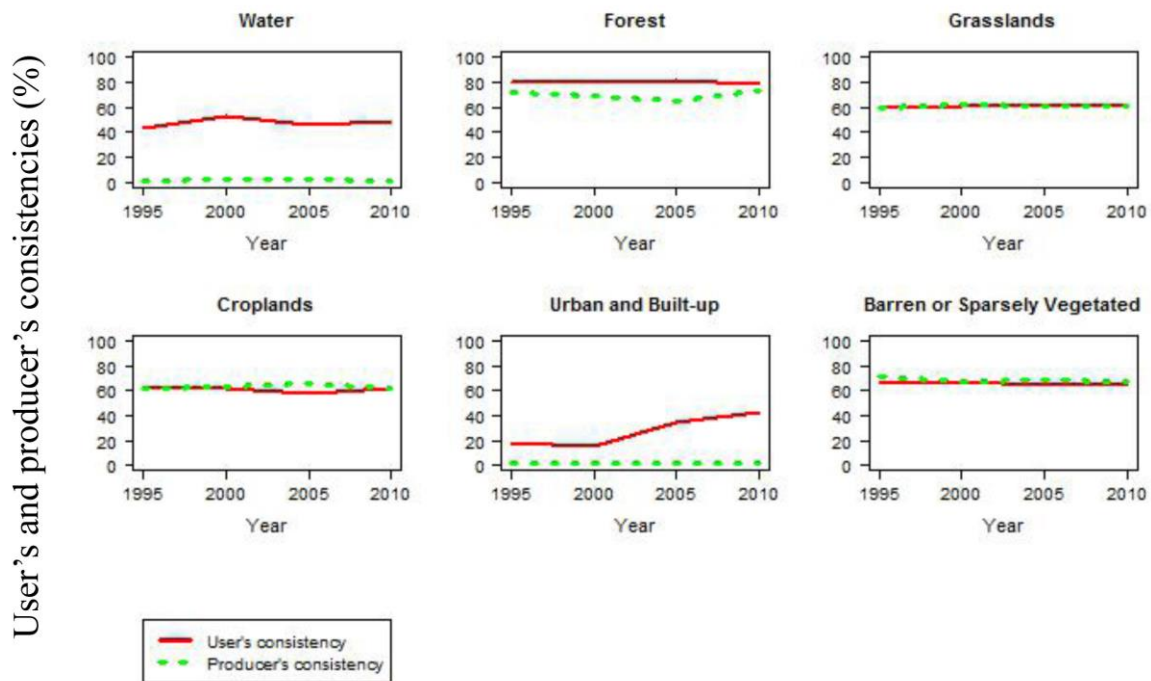
Figure 2.11. User's and producer's consistencies for each class between classified LULC and CLU maps for 1995, 2000, 2005, and 2010.

2.3.3.4 *Accuracy evaluation of the 2012 classification using Google Earth imagery*
The error matrix for the accuracy assessment of the 2012 AVHRR map, using the visual interpretation of eight classes from 256 samples of Google Earth images from 2012 as reference data, is shown in **Table 2.7**. The overall accuracy is 73.8%. The producer's and user's accuracies for urban and built-up, as well as producer's accuracy

for cropland and natural vegetation mosaic and user's accuracy for snow and ice, are low, but these estimates are based on a relatively small number of samples, and thus the uncertainty in these estimates is comparatively large. Another possible reason for the low accuracy of urban and built-up class may be the coarse spatial resolution of GIMMS NDVI data. As mentioned in Liu et al. (2003c) and Loveland et al. (2000), the urban class may easily be confused with other classes due to the complex mixtures of surface materials within each pixel. The low accuracy for cropland and natural vegetation mosaic and snow and ice may be due to the similarity of phenological characteristics with other classes (i.e., croplands and barren or sparsely vegetated, respectively). For instance, Guan et al. (2014) noted that in Africa, most croplands were fragmented and mixed with natural savannas, resulting in generally similar phenology patterns. The barren or sparsely vegetated class, which has a distinctive low NDVI year-round, has user's and producer's accuracies greater than 90%. Overall, the allocation disagreement (16.2%) is higher than the quantity disagreement (10.0%), which indicates the disagreement between our classified LULC map and Google Earth reference data is mainly due to errors in the location of the mapped classes, rather than their proportions in the map. Improving the quality of the training data might improve the spatial consistency of the map and thus improve the overall accuracy of our classified map.

Table 2.7. Error matrix of Google Earth data and classified LULC

		Reference LULC (from Google Earth interpretation)									
		Water	Forest	Grasslands	Croplands	Urban and built-up	Cropland and natural vegetation mosaic	Snow and Ice	Barren or sparsely vegetated	Total	User's accuracy
Classified LULC	Water	0.00049	0.00000	0.00000	0.00000	0.00004	0.00004	0.00000	0.00000	0.00057	86%
	Forest	0.00000	0.15101	0.00000	0.04066	0.00000	0.02323	0.00000	0.00000	0.21491	70%
	Grasslands	0.00000	0.01921	0.19211	0.07684	0.00000	0.00480	0.00000	0.01441	0.30737	63%
	Croplands	0.00000	0.03800	0.01900	0.16623	0.00475	0.01425	0.00000	0.00000	0.24223	69%
	Urban and built-up	0.00000	0.00011	0.00004	0.00008	0.00015	0.00011	0.00000	0.00000	0.00049	31%
	Cropland and natural vegetation mosaic	0.00000	0.00000	0.00000	0.00082	0.00000	0.00905	0.00000	0.00000	0.00988	92%
	Snow and Ice	0.00000	0.00000	0.00000	0.00000	0.00000	0.00000	0.00053	0.00177	0.00230	23%
	Barren or sparsely vegetated	0.00000	0.00000	0.00427	0.00000	0.00000	0.00000	0.00000	0.21799	0.22226	98%
	Total	0.00049	0.20833	0.21542	0.28463	0.00494	0.05149	0.00053	0.23417	1.00000	
	Producer's accuracy	100%	72%	89%	58%	3%	18%	100%	93%		73.8%

Using the same samples from Google Earth as reference data, the MODIS MCD12Q1 2012 error matrix is shown in **Table 2.8**. Because there is no snow and ice class for the sample points in 2012 MODIS data, it is impossible to calculate the proportion of area P_{ij} for snow and ice in error matrix. Therefor, we deleted the snow and ice class, remaining seven classes with 253 sample points for validating 2012 MODIS MCD12Q1. As with our 2012 AVHRR map, the MODIS producer's accuracies for the urban and built up land, as well as cropland and natural vegetation mosaic classes, are very low. The allocation disagreement and quantity disagreement are 12.1% and 16.6%, respectively, indicating the disagreement between MODIS map and Google Earth reference data is mainly due to errors in the proportions in the map. The overall accuracy of the 2012 MODIS LULC for the seven classes is estimated as 71.3%, 2.5% lower than the accuracy of our classified LULC. However, the McNemar's statistic (de Leeuw et al. 2006) based on the comparison of the two accuracy assessments is approximately 0.4, indicating that this difference is not statistically significant at the 95% confidence level.

Table 2.8. Error matrix of Google Earth data and MODIS LULC

		Reference LULC (from Google Earth interpretation)								
		Water	Forest	Grasslands	Croplands	Urban and built-up	Cropland and natural vegetation mosaic	Barren or sparsely vegetated	Total	User's accuracy
MODIS LULC	Water	0.00619	0.00000	0.00000	0.00000	0.00077	0.00000	0.00000	0.00696	89%
	Forest	0.00000	0.15929	0.01493	0.02489	0.00000	0.04480	0.00498	0.24889	64%
	Grasslands	0.00441	0.03531	0.18098	0.05738	0.00000	0.02207	0.01766	0.31782	57%
	Croplands	0.01035	0.00000	0.00345	0.13106	0.01035	0.01380	0.00000	0.16900	78%
	Urban and built-up	0.00000	0.00000	0.00000	0.00119	0.00238	0.00000	0.00000	0.00358	67%
	Cropland and natural vegetation mosaic	0.00000	0.00332	0.00000	0.00996	0.00000	0.01661	0.00000	0.02989	56%
	Barren or sparsely vegetated	0.00000	0.00000	0.00367	0.00367	0.00000	0.00000	0.21652	0.22386	97%
	Total	0.02095	0.19793	0.20303	0.22816	0.01350	0.09728	0.23915	1.00000	
	Producer's accuracy	30%	80%	89%	57%	18%	17%	91%		71.3%

2.3.4 Spatial patterns and temporal trends of annual LULC in China

Example classifications for 1982, 1992, 2002, and 2012 are shown in **Figure 2.12**. It is worth noting that the classification was carried out in four separate regions, with arbitrary boundaries (**Figure 2.5**). Nevertheless, a close examination of the final classifications (**Figure 2.12**) indicates no obvious evidence of artifacts or errors across these boundary lines. The maps show that in Western China, LULC appears broadly similar during the period 1982 to 2012. Croplands in Xinjiang province increase a little from 1982 to 2002, and then decrease from 2002 to 2012. The initial increase in croplands in Xinjiang may be attributed to the successful promotion of modern agronomic technology (Yin 2008), whilst the recent decrease, also observed by Liu et al. (2008), may reflect the conversion of cropland to built-up land, associated with the policy of increased Western China development. In Northeast China croplands increase notably during the three decades, while grasslands and mixed forest decrease. In Central China, croplands first increase from 1982 to 1992, then decease along the upper reach of Yellow River basin from 1992 to 2002, followed by an increasing trend during the last decade. In contrast, grasslands in Central China decrease from 1982 to 1992, followed by an increasing trend from 1992 to 2002 and a decreasing trend from 2002 to 2012. The recent increase in cropland, and reduction in other classes, is supported by the observations of Xu et al. (2015) in Central China, who noted, in a study that focused on the period since 2000, a conversion of wetlands, barren areas, and woody shrubland to cropland. In Southern China, cropland area decreases during the entire period from 1982 to 2012. Mixed forest and evergreen broadleaf forest increase, especially along the Yangtze river and tropical regions, such as the south part of Yunnan province. Woody savannas first increase from 1982 to 2002, then decrease during the last decade. The overall changing patterns in croplands documented in these maps, an increase in Northern China and decrease in Southern China, are broadly consistent with Liu et al. (2014). However, although a thorough analysis of the underlying reasons for different patterns of LULC over different regions in China is needed, this is beyond the scope of this paper.
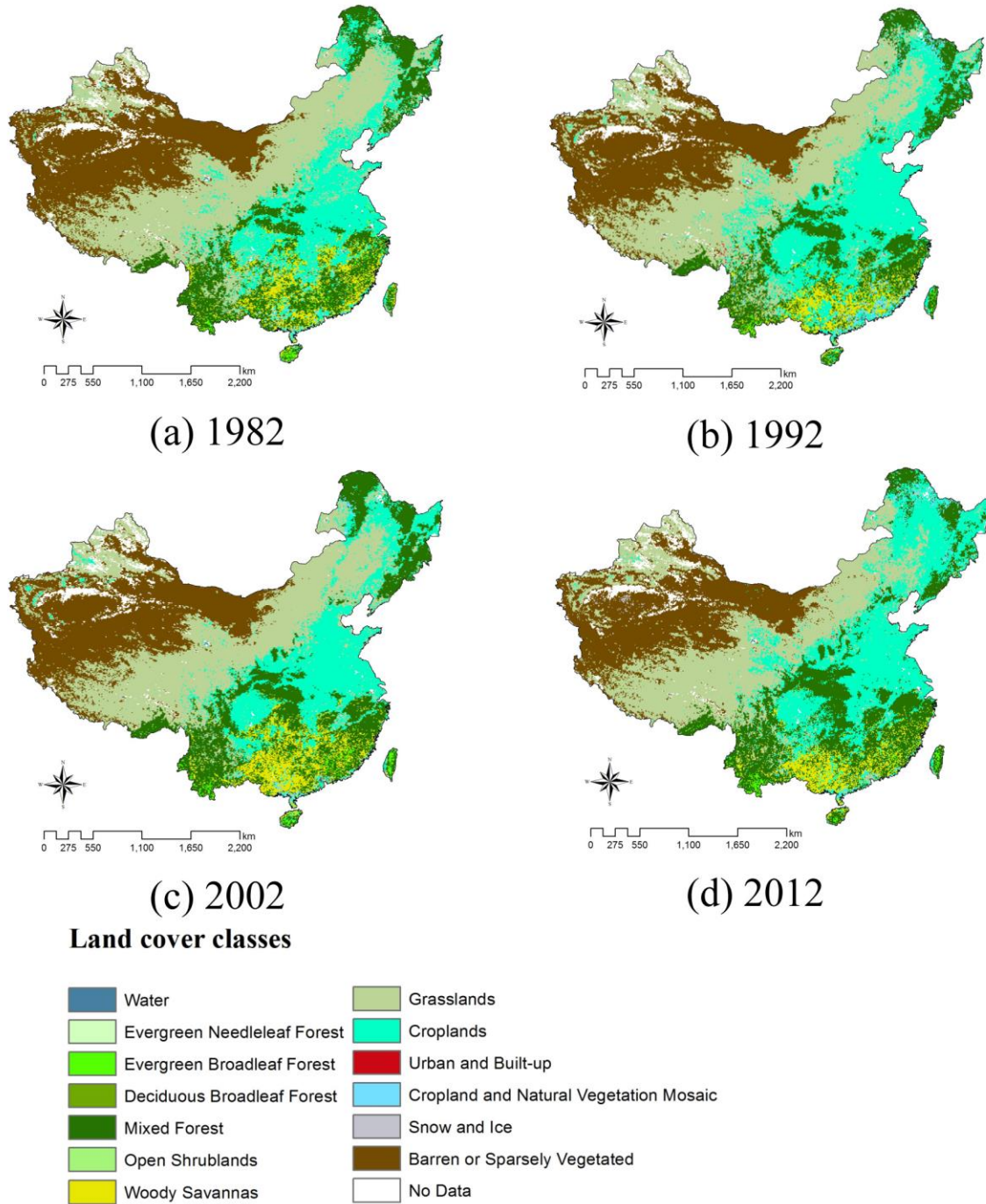
Figure 2.12. Annual LULC maps of China, produced by random forest classification. (a) 1982, (b) 1992, (c) 2002, and (d) 2012.

Based on abovementioned analyses, croplands, forest, and grasslands show the clear spatial change patterns. In **Figure 2.13,** we show the overall trends of these three

classes across the entire 32 years of the study for further analysis. In here, the forest class means evergreen needleleaf forest, evergreen broadleaf forest, deciduous broadleaf forest, and mixed forest in the column "class for AVHRR classification" in **Table 2.1**. We used the R nlme package (Pinheiro et al. 2014) to conduct the linear regression trend analysis accounting for temporal autocorrelation. The significance of the trend was tested by Student's *t* test. The overall trend for grassland is a significant decrease at the 1% level. This is consistent with Liu et al. (2014), who used Landsat TM/ETM+ data acquired in intervals of five years to explore LULCC in China since the late 1980s. The overall trend for forest is increasing, which may be due to afforestation efforts, such as the "Grain for Green" and "Three-North Shelterbelt" projects (Liu et al. 2014). The overall trend of cropland is an increase during the three decades. However, the standard errors of the trends for forest and croplands are larger than that of grasslands, and thus the uncertainty of the trends may be bigger. The trends for both forest and croplands are not significant at the 10% level. While the overall trends of these three classes are generally consistent with previous studies, there are some short-term variations in the three times series that seem inconsistently large, such as the large temporary increase in grasslands in 1984 as well as the decline in forest and increase in croplands in 1993. The latter short-term anomaly was also identified by He and Shi (2015), but the reasons for these variations do need to be explored further. Absent an obvious physical explanation, such as unusual weather patterns, or other national policy changes or pressures (Liu et al. 2003b), our assumption is that these variations may be artifacts, such as the result of temporal inconsistent variations of GIMMS NDVI time-series due to sensor drift. Previous studies have revealed the temporal inconsistency of GIMMS NDVI dataset (Detsch et al 2016; Fensholt et al. 2009; Fensholt and Proud 2012; Tian et al. 2015). For example, Tian et al. (2015) found that the abrupt increase of NDVI around 1994 coincided with the sensor shift from NOAA-11 to NOAA-9. The coarse spatial and temporal resolution of GIMMS dataset may also contribute to the artifacts. Alcaraz-segura et al. (2010) stated that GMMMS NDVI dataset failed to capture long-term ecosystem changes in some places, such as central Canada, while they were evident by using higher spatial resolution NDVI datasets, such as Canadian Centre for Remote Sensing (CCRS) NDVI dataset.
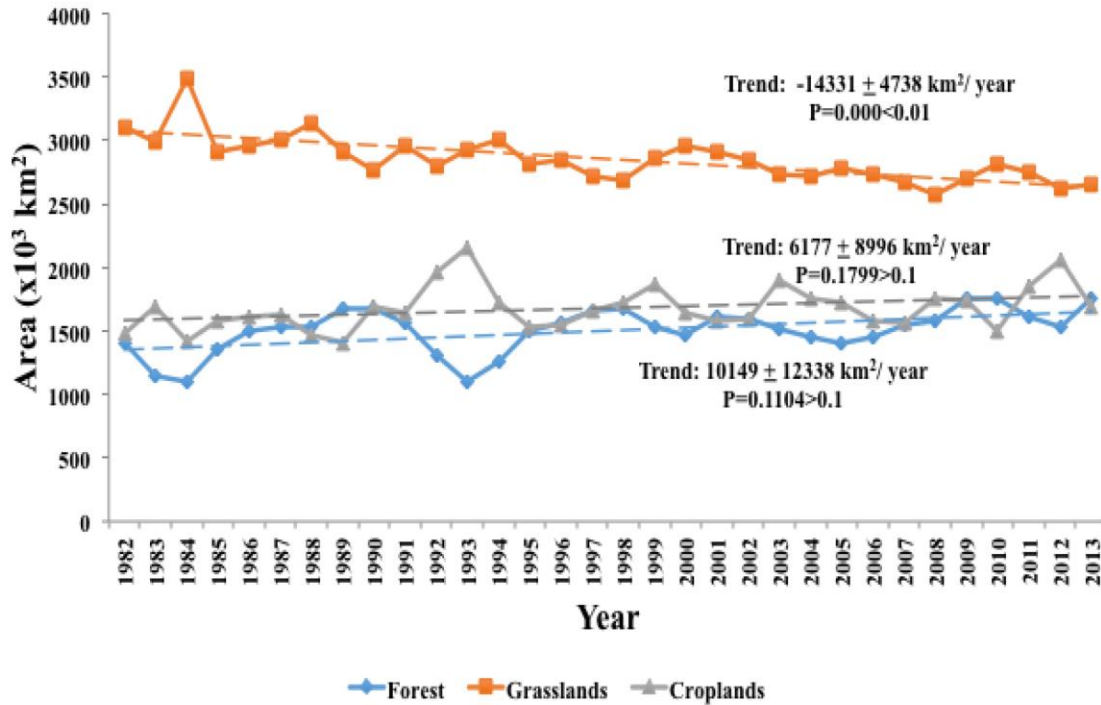
Figure 2.13. Temporal changes in area of grasslands, croplands, and forest classes from 1982 to 2013. Dotted lines represent overall trend.

2.4   Summary

Both observational and modeling studies have shown that LULCC can significantly affect the climate system (Takata et al. 2009, Webster 1987). This may happen through biogeophysical (changes in water and energy balance) and biogeochemical (changes in CO_2 and methane) processes that modify surface wetness, partition surface energy between sensible and latent heat fluxes, alter roughness of the land surface, and change terrestrial carbon storage (McPherson 2007, Foley et al. 2003). China has experienced extensive LULCC, including cropland expansion, desertification, deforestation, afforestation, and urbanization (Houghton and Hackler 2003, Lin and Ho 2003, Ge et al. 2004, Liu et al. 2005). However, due to the limited period for which time-series of annual land use and land cover maps are available, LULCC information in China has been normally used in climate modeling in only a simplified manner.

To address this need for an extended time-series of LULC data, we constructed a three-decade continuous time series of annual land use and land cover maps of China from 1982 to 2013 using AVHRR GIMMS NDVI3g data. The reference data for training the classifier was a 25% sample of the pixels of constant LULC class in the MODIS MCD12Q1 annual land cover maps from 2001 to 2010. Classes for which the number of reference pixels were zero, or close to zero, were excluded, reducing the number of classes from 17 to 13 (**Table 2.1**). 19 phenological features were derived from the AVHRR data, and used as attributes in the random forest classification.

Based on the validation data (75%), the overall accuracy of the AVHRR classification for 2001 to 2010 was greater than 91% for each region, except Southern China, for which it was 79%. This result is strong evidence that the AVHRR phenological features are broadly able to differentiate the different MODIS LULC classes. The higher user's accuracy and producer's accuracy for mixed forest, grasslands, croplands, and barren or sparsely vegetated in all of the four regions indicate the performance of random forest classifier is better in separating classes with larger reference data.

In the comparison with the MODIS classification across all of China for 2011 and 2012, years not used in training the classifier, consistency was 71.0% and 69.3%, respectively. It is not surprising that these numbers are lower than the accuracies for the unchanged pixels in the 2001 to 2010 reference data, since the latter data are presumably mostly pixels with consistent land cover with relatively distinct remote sensing spectral characteristics. Furthermore, we would expect slightly lower accuracy of land cover classification in years not used for training, since the climatic variations and thus phenological patterns from 2001 to 2010 may not have captured the entire range of possible conditions. However, comparisons of our AVHRR classification and the MODIS MCD12Q1 data from 2001 to 2010 (years that were used for training) show only 0-3% improvement, indicating that this effect is small. The relatively low consistency for Southern China may be due to extensive clouds in the relatively humid Southern China. For instance, An et al. (2015) found that poor relationships between MODIS and SPOT

NDVI datasets in Southern China may be attributed to greater cloud cover in that area. In summary, we regard the broad consistency with MODIS data as one line of evidence of the ability of the classifier to be extended over time. The comparisons between our classified maps and CLU data show the lower consistency values, ranging from 63.0% to 64.4%. It is in our expectation, because converting the very different spatial resolutions (i.e., 30 m for original CLU and 1/12° for our classified LULC) and classification systems may induce additional inconsistencies.

An overall accuracy assessment of the AVHRR classification was carried for 2012, a year not used for training. The reference data were derived from a visual interpretation of stratified random samples of Google Earth imagery. This accuracy assessment combined all the forest classes, resulting in a simplified map with just eight classes. The overall accuracy of this eight-class map was 73.8%. In comparison, the MODIS MCD12Q1 product, which has been estimated to have a global accuracy of approximately 75% (Zhao et al. 2013), was found to have an accuracy of 71.3% for China in 2012. The McNemar's test indicated no significant difference between the MODIS LULC and AVHRR LULC accuracies. We regard this finding as particularly notable. MODIS is a sensor with greater spectral and radiometric resolution than AVHRR (Tucker et al. 2005), and thus achieving an accuracy with AVHRR that is similar to the MODIS product is encouraging. On the hand, it is important to acknowledge that the MODIS MD12Q1 is generated through a global classification, whereas our classification is based on four regional classifications, a much simpler mapping task.

Several areas of future work seem promising. First, using as reference data areas in the MODIS MD12Q1 maps that do not change over an extended period of time, an approach previously also successfully employed by others, including Klein et al. (2012) and Wohlfart et al. (2016), provides a simple approach that can easily be applied to other regions. In particular, we plan to investigate ways to scale the method up to a global approach, since having annual land cover maps of the entire world for more than 30 years could be particularly valuable to the climate modeling community. A second line of

research would be to consider alternative methods for generating the reference data. Although the MODIS data provide a very effective method for selecting large numbers of training samples over multiple years, the reliability of the MODIS data is not that high (Zhao et al. 2013). Moreover, since pixels of some unchanged classes are not present in some of the regions in the training data (e.g., deciduous broadleaf forest in Western and Southern China) (**Table 2.1**), the final classification maps in these regions do not have these classes. In addition, the reference data does not distribute evenly across different classes. Some classes have larger numbers of reference data, such as grasslands, while other classes have much less reference data, such as water (**Table 2.1**). These influence the classification accuracies of the classes (**Table 2.6**). It is possible that if we could generate more reliable training data, we might improve the accuracy of the AVHRR classification. The final area of possible future research would be to establish statistically robust approaches to investigate the time series for its potential to produce change maps. This would require an evaluation of the accuracy of the change information itself, rather than only an evaluation of the accuracy of the individual dates, as we have done in this study.

In summary, this study generated annual land use and land cover maps in China from 1982 to 2013 using AVHRR GIMMS NDVI3g data. The overall accuracy from random forest classifier was high for all of the regions, except for Southern China. Based on a comparison of visual interpretation of images from Google Earth, the overall accuracy of the simplified eight-class LULC map was 73.8%, which was not statistically different from that of the simplified seven-class MODIS MCD12Q1 LULC map (71.3%). Based on temporal evolution of areas for forest, grassland, and cropland during the last three decades, the overall trend was consistent with previous studies (He and Shi 2015, Liu et al. 2014). These thirty-two years of annual maps of land cover will be an important dataset for quantifying the associations of recent LULCC with changes in the regional climate systems in East Asia, and the pre-processing, classification, and validation methods used in this study could be applied to other geographical regions where the availability of continuous LULC maps is limited.

3 Reducing uncertainties in applying remotely sensed land use and land cover maps in land-atmosphere interaction: identifying change in space and time*

3.1 Introduction

Human activities have transformed a large proportion of the plant's land surface (Foley et al. 2005) through processes such as deforestation of tropical forests, as well as intensified agricultural land-use and urbanization in China and India. Human-induced land use and land cover change (LULCC) can alter surface roughness, surface wetness, the partitioning of surface energy between sensible and latent heat fluxes, and terrestrial carbon storage (McPherson 2007, Pielke 2005, Lee et al. 2015, Foley et al. 2003, Mahmood et al. 2014). These changes are increasingly becoming a focus of concern because of their potential to influence the climate system (Bonan et al. 1992, He and Lee 2016), and as a consequence, the Intergovernmental Panel on Climate Change (IPCC) has emphasized the importance of understanding the climate response to LULCC at local, regional, and global scales (IPCC 2014). In particular, identifying and quantifying LULCC is crucial for a better understanding of land-atmosphere interaction and thereby climate change and variability (Mahmood et al. 2014).

Efforts to map land use and land cover (LULC) and its changing patterns using remotely sensed data have been a focus of much attention over the last three decades (Liu and Tian 2010, Ramankutty and Foley 1999, Liu et al. 2003, Liu 1996, Liu et al. 1998, Schneider and Mertes 2014). Remote sensing can potentially provide not only accurate and repeatable global LULC information, but also time series data that can be used to map change (Townshend et al. 1991, Running et al. 1994). However, remotely sensed LULC maps usually have very different spatial resolutions from that of climate data, including atmospheric and oceanic variables. For both physical and observational

reasons, climate data generally have much coarser spatial resolution than remotely sensed LULC data. For example, National Center for Environmental Prediction (NCEP)/ National Center for Atmospheric Research (NCAR) reanalysis, European Centre for Medium-Range Weather Forecasts (ECMWF) reanalysis (ERA-40), and Climate Research Unit Timeseries (CRU TS) high-resolution gridded datasets have a resolution of 2.5° by 2.5°, 1.125° by 1.125°, and 0.5° by 0.5°, respectively. While anthropogenic forces and other drivers (e.g., natural disturbance from fires or storms, sharp gradients of riparian vegetation) can dramatically alter LULC at fine scales, the atmosphere is often more well-mixed, with properties changing more gradually across spatial scales. Simply resampling LULC maps into the same resolution as climate data is problematic, as LULCC is complex, with heterogeneous patterns that may not be evident in simple measures, such as dominant change type, in coarse resolution data.

Problems of spatial scale mismatches are well known to the remote sensing community. For example, Woodcock and Strahler (1987) proposed local variance as a frame work for examining the effects of scale and spatial resolution in remotely sensed images. They found that traditional spectral classification that produced a single class for each pixel was appropriate where the spatial resolution of the imagery was much finer than the objects in the scene. In contrast, for images where the spatial resolution is not sufficient to resolve the objects, a mixture model, which estimates the proportion of the classes within a pixel, is required [18]. In subsequent work, a more rigorous treatment was developed using variograms (Woodcock, Strahler and Jupp 1988). Cao and Lam (1997) thoroughly reviewed scale and resolution effects that were relevant to geographic information system (GIS) and remote sensing, and usefully identified four conceptualizations of spatial scale: cartographic scale, geographic (observational) scale, operational scale, and measurement (resolution) scale. In a more recent study, Peng et al. (2017) compared several downscaling methods for remotely sensed soil moisture products, including a satellite-based fusion method, a method using geoinformation data, and model-based methods. They concluded that each method has its own advantages and disadvantages, and none of the methods can be applied everywhere across the world without any calibration or improvements [21]. In land-atmosphere interaction studies, the

potentially problematic scale effects of the spatial resolution of LULC data and issues of rescaling have been largely overlooked. For example, Community Earth System Model (CESM) adopts LULC data from Moderate Resolution Imaging Spectroradiometer (MODIS) at 0.05° (approximately 5 km) resolution (Lawrence and Chase 2007) while the original spatial resolution of MODIS LULC data is 1 km (Friedl et al. 2002). It is therefore important to identify the effect of different spatial scaling methods for LULC data on land-atmosphere interaction.

Another uncertainty in land-atmosphere interaction studies is due to insufficient LULC time-series data to detect long-term LULCC patterns. Cao et al. (2015) emphasized that longer time periods of LULC data are needed to quantify land-atmosphere interaction. The longest continuous annual LULC data is MODIS land cover data, which only covers from 2001 onward. The primary method of extracting LULCC information from remotely sensed data has been through separate classifications of imagery of two different dates, which are overlaid to obtain change information (Liu et al. 2003). For example, Rawat and Kumar (2015) used 1990 and 2010 Landsat Thematic Mapper (TM) images to classify the land surface of Hawalbagh block, Uttarakhand, India, and thus mapped LULCC over a 20-year period. Similarly, Liu et al. (2005) classified cropland based on 1990 and 2000 Landsat TM/ Enhanced Thematic Mapper Plus (ETM+) data to quantify the changing spatial patterns of cropland in China during 1990 to 2000. However, LULCC information from just two time steps or even several time periods may obscure important overall trends in land cover change, especially in regions where land cover change is dynamic. For example, temporary fluctuations in a landscape where land cover change is common, such as occurs with the logging of short-rotation forests (Qiao et al. 2016), may obscure important long term trends in land cover change. Change that is non-significant over long time periods could bias analyses that use LULCC as an input or initial forcing for the biophysical and biogeochemical processes of land-atmosphere interaction (Lee et al. 2011, Xue 1996, Fu 2003, Jones et al. 2008, Han and Yang 2013, Chen and Dirmeyer 2016). Considering this limitation in recent LULCC detection studies, a spatio-temporal analysis using a long-term time-series of LULC maps is an effective option. Such an approach can identify statistically significant spatio-

temporal LULCC, and also provide information regarding the types of LULCC and the dominant transitions among the LULC types.

In this study, we addressed these uncertainties related to the spatial and temporal resolutions of LULC data. Firstly, we used two regions in China (**Figure 3.1**): a relatively homogenous region (North China plain), and a more heterogeneous region (Sichuan basin) to explore the effect of LULC spatial resolution on the relationship of LULC data and the land surface climatic variable of latent heat flux. We aggregated the original resolution of the LULC maps from $0.0833°$ to $0.5°$, $1.0°$, and $2.5°$, which are the commonly used spatial resolutions of climatic variables. At each resolution, we investigated how the correlation of LULC data and latent heat flux is affected by three spatial aggregation methods. We used nearest neighbor and majority aggregation methods, which preserve the LULC maps as nominal maps, and a fractional method, which transforms the nominal LULC maps into fractional maps.

Using the optimal scale and scaling method identified in these experiments within the spatial domain, we then explored the temporal changes from 1982 to 2012 for croplands, forests, and grasslands, which are the dominant LULC types in China. Specifically, we used a newly developed 31-year times-series of annual LULC maps (He, Lee and Warner 2016, He, Lee and Warner 2017) to ask: Where are the statistically significant LULCC regions in China based on the long-term time-series LULC maps, and what are the dominant transitions among the different types of LULC?
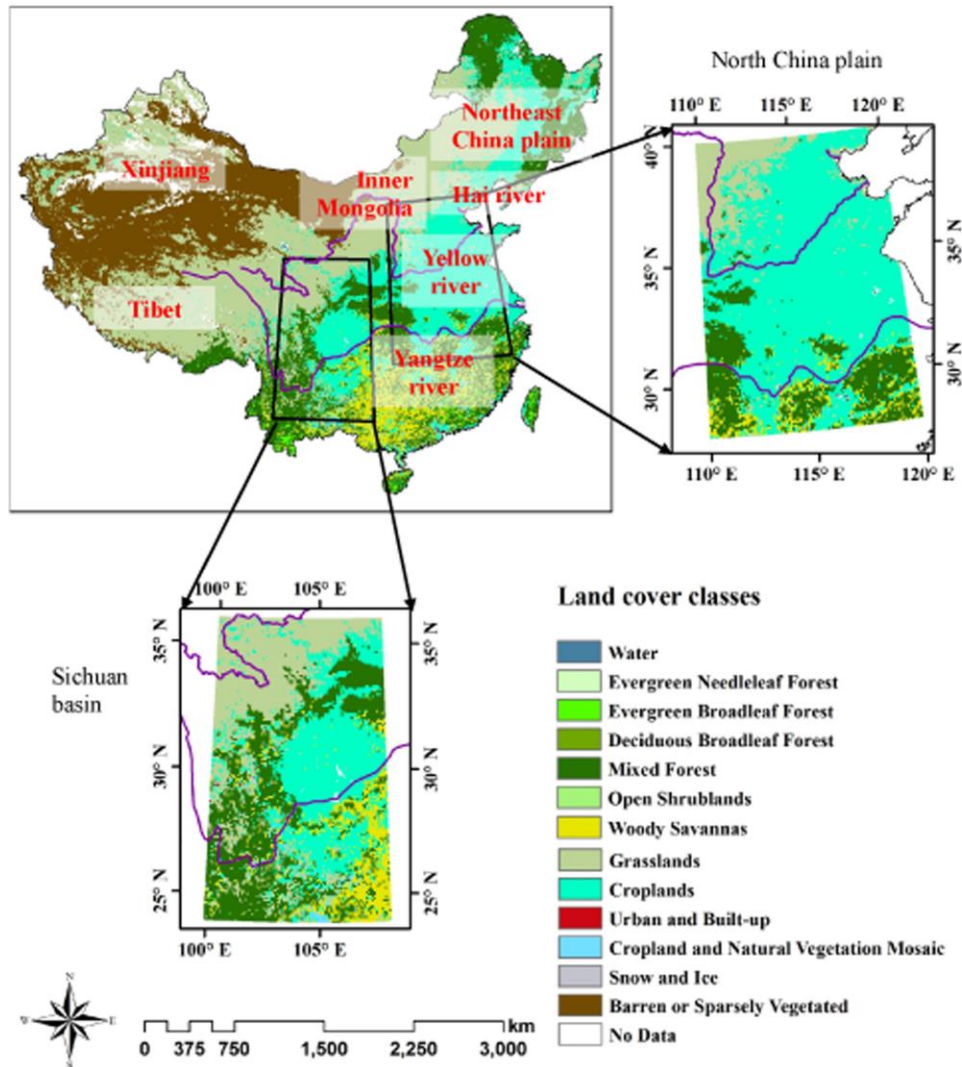
Figure 3.1. Land use and land cover map of China from 2000, with the North China plain, and Sichuan basin subsets used in the spatial rescaling experiments shown. The geographic locations labeled in red are referred to in Section 3, Results.

3.2 Materials and Methods

3.2.1 Materials

The primary dataset used in this study are continuous annual LULC maps of China, covering the period from 1982 to 2012. Figure 1 shows the LULC map of 2000 as an example. The data were generated by (He et al. 2017), using a random forest classification of 19 phenological metrics derived from AVHRR Global Inventory Modeling and Mapping Studies (GIMMS) third generation NDVI (NDVI3g) data. The 19

phenological metrics include start of growing season, end of growing season, maximum and minimum NDVI values, and so on. The classifier was trained using reference data derived from pixels within the MODIS land cover (MCD12Q1) maps that did not change over the period of 2001 to 2010. The phenological metrics were extracted using Interactive data language (IDL; Harris Geospatial Solutions, Florida, USA) and the classification was carried out using R randomForest package. The LULCC maps have a 0.0833° (approximately 8 km) spatial resolution and 13 classes, as listed in the legend of Figure 1. The overall accuracy of a simplified eight-class version of the 2012 LULC map was estimated to be 73.8% (refer to He et al. (2017) for more information). We chose LULC maps of 1982, 1988, 1994, 2000, 2006, and 2011 for spatial rescaling experiments.

As a climatic variable for exploring the effects of rescaling, we chose latent heat flux, because it links the land surface condition to the atmosphere. Latent heat flux data was obtained from the FLUXNET-Multi-Tree Ensemble (MTE). FLUXNET-MTE datasets were estimated using a machine learning approach called model tree ensemble based on FLUXNET measurements, a long-term remotely sensed monthly fraction of absorbed photosynthetically active radiation (fAPAR) dataset, near surface air temperature from Climatic Research Unit (CRU), precipitation data from the Global Precipitation Climatology Center (GPCC), an estimate of the top of the atmosphere shortwave radiation, and information on land cover (Jung et al. 2011).

The land cover map used in FLUXNET-MTE dataset was static and did not vary over time (Jung et al. 2011). In the MTE model, the land cover data were only used to stratify the data, and did not act as predictor variables for deriving data layers such as the latent heat flux in the regression equations (Jung, Reichstein and Bondeau 2009). The global estimates of latent heat flux were similar to other independent estimates (Oki and Kanae 2006, Trenberth, Fasullo and Kiehl 2009, Dirmeyer et al. 2006) and the R-squared was 0.92 when correlated with catchment water balances (Jung et al. 2010). The FLUXNET-MTE dataset has been widely used in hydrology and land-atmosphere interactions studies (Jung et al. 2010, Bonan et al. 2011, Liu et al. 2013, Koster and P. Mahanama 2012, Pan et al. 2015). The spatial resolution of the latent heat flux datasets is

0.5° by 0.5°, over the period 1982 to 2011. For consistency with the LULC data from the years 1982, 1988, 1994, 2000, 2006, and 2011, latent heat flux during the peak growing time of August in 1982, 1988, 1994, 2000, 2006, and 2011 was chosen for the analysis.

Although the latent heat flux derived from FLUXNET-MTE can be influenced by land cover types (Yang et al. 1999, Biraud et al. 2005, Williams and Torn 2015), our objective is to investigate how the relationships between latent heat flux and LULC data derived from different spatial scaling methods (i.e., fractional method, nearest neighbor method, and majority aggregation method) change over three different resolutions (i.e., 0.5°, 1.0°, and 2.5°). In doing so, we anticipate identifying the best spatial rescaling method, which can preserve the relationships between latent heat flux and LULC data among different scales.

3.2.2   Methods

3.2.2.1   *Spatial scaling methods*
To explore the suitability of different approaches for scaling LULC maps for land-atmosphere interaction studies, we compared three rescaling methods: nearest neighbor, majority aggregation, and a fractional method. The effectiveness of these methods was compared for the aggregation of LULC maps of China with an original 0.0833° spatial resolution, which we rescaled to 0.5°, 1.0°, and 2.5° spatial resolution.

Nearest neighbor and majority aggregation methods, which are commonly used for categorical data such as LULC maps, preserve the nominal nature of LULC maps. In the nearest neighbor method, the value of an output pixel is determined by the pixel nearest to it in the input data (Baboo and Devi 2010). Majority aggregation assigns the most frequently occurring value in the input data to the new pixel (He et al. 2017). The fractional method is a proportional estimate of land cover for each class at the coarser resolution. Specifically, the spatial resolution of the LULC map is aggregated from 0.0833° to 0.5°, 1.0°, and 2.5°, by calculating the proportion of the new coarse-scale pixel covered by each class within respectively a 6 x 6, 12 x 12, and 30 x 30 pixel region in the fine scale data.

We chose bilinear interpolation to resample the latent heat flux data from the original 0.5° to 1.0° and 2.5° spatial resolutions, because it is the method commonly used in the climate community to regrid interval data. In bilinear interpolation, the output pixel value is estimated through linear interpolation of the four pixel values in two orthogonal directions within the input data (Han, Li and Gong 2010).

3.2.2.2 Exploring the relationship between LULC data and latent heat flux at different spatial resolutions

For this section, we focused on croplands, because croplands are the dominant LULC type in the North China plain and the Sichuan basin (**Figure 3.1**). For fractional LULC maps, we explored relationships between LULC data and latent heat flux by exploring the correlation between the fraction of croplands and latent heat flux. The correlation coefficient is (Pearson 1895):

$$r = \frac{\sum XY - \frac{\sum X \sum Y}{N}}{\sqrt{\left(\sum X^2 - \frac{(\sum X)^2}{N}\right)\left(\sum Y^2 - \frac{(\sum Y)^2}{N}\right)}} \tag{1}$$

Where, X is the fraction of croplands at different spatial scales in each pixel, and Y is the corresponding August latent heat flux value for each pixel. The significance of the correlation coefficient was tested by Student's t test.

For nominal LULC maps, the relationship between LULC data and latent heat flux was tested by the Wilcoxon rank sum test. The Wilcoxon rank sum test was used to identify the significance of the difference in the distributions of the latent heat flux values in croplands compared to non-croplands. The Wilcoxon rank sum test is a non-parametric test and suitable for small samples (Hogg, Tanis and Zimmerman 2014). We chose the Wilcoxon rank sum test because our sample size is proportionally reduced as the spatial scale coarsened.

3.2.2.3 Linear regression trend analysis

We tested the usefulness of the fractional rescaling method for evaluating trends in land cover change. We aggregated our 31-year LULC maps using the fractional

method, and in doing so, generated fractional maps for croplands, forests, and grasslands, respectively. These 31-year fractional maps were summarized through linear regression trend analysis and spatial pattern correlation analysis to determining the long-term LULCC patterns.

Linear regression analysis is a statistical method for analyzing the relationship between two or more variables by evaluating the degree to which one variable can be predicted or explained by the others (Freund, Wilson and Sa 2006). The simple linear regression model is:

$$Y = a + b\,X + e \tag{2}$$

Parameters a and b are the regression coefficients, which are estimated by a least squares method (Walpole et al. 1993); e is the regression residual. In this study, we are interested in b, the slope of the regression line, which characterizes how the Y variables (fraction of croplands, forests, and grasslands, respectively) change over time (X). The significance of the trends was estimated using a Student's t test. A trend analysis was performed to determine the spatio-temporal changes in croplands, forests, and grasslands for each grid cell independently, and regions where LULCC is significant were thereby identified. Statistically non-significant regions were masked out, and consequently only pixels significant at the 5% level are shown in the maps.

3.2.2.4 *Spatial pattern correlation analysis*

Within four regions where statistically significant changes were identified, we performed spatial pattern correlation analysis to investigate the transitions among the LULC types (e.g., grasslands transitioning to croplands, or croplands to forests). The correlation coefficient here is the same as **Equation (1)**. However, the X and Y have a different meaning. Here, X and Y are the trend values (b in the **Equation (2)**) of croplands, forests, and grasslands at each grid cell, respectively. The significance of correlation coefficient was quantified using a adjusted Student's t test, accounting for spatial autocorrelation through a correction of the degrees of freedom of the samples (Clifford, Richardson and Hémon 1989).

3.3 Results and Discussion

3.3.1 Categorical and factional LULC maps at different spatial resolutions in the North China plain and the Sichuan basin

The North China plain is a relatively homogenous region, with croplands dominant. In contrast, the Sichuan basin is a relatively heterogeneous region, with croplands, mixed forests, and grasslands prevalent (**Figure 3.1**). The overall pattern of croplands in the North China plain and the Sichuan basin is evident in both categorical LULC maps and fractional maps at all three spatial scales (**Figure 3.2**). However, due to coarsening of the spatial scale, the heterogeneous patterns of croplands are smoothed, especially at the 2.5° scale. Generally speaking, nearest neighbor, majority aggregation, and fractional methods capture the croplands patterns better at the finest scale, 0.5°, with notable smoothing at the scales of 1.0° and 2.5°.

(a) Nearest neighbor method   (b) Majority aggregation method   (c) Fractional method
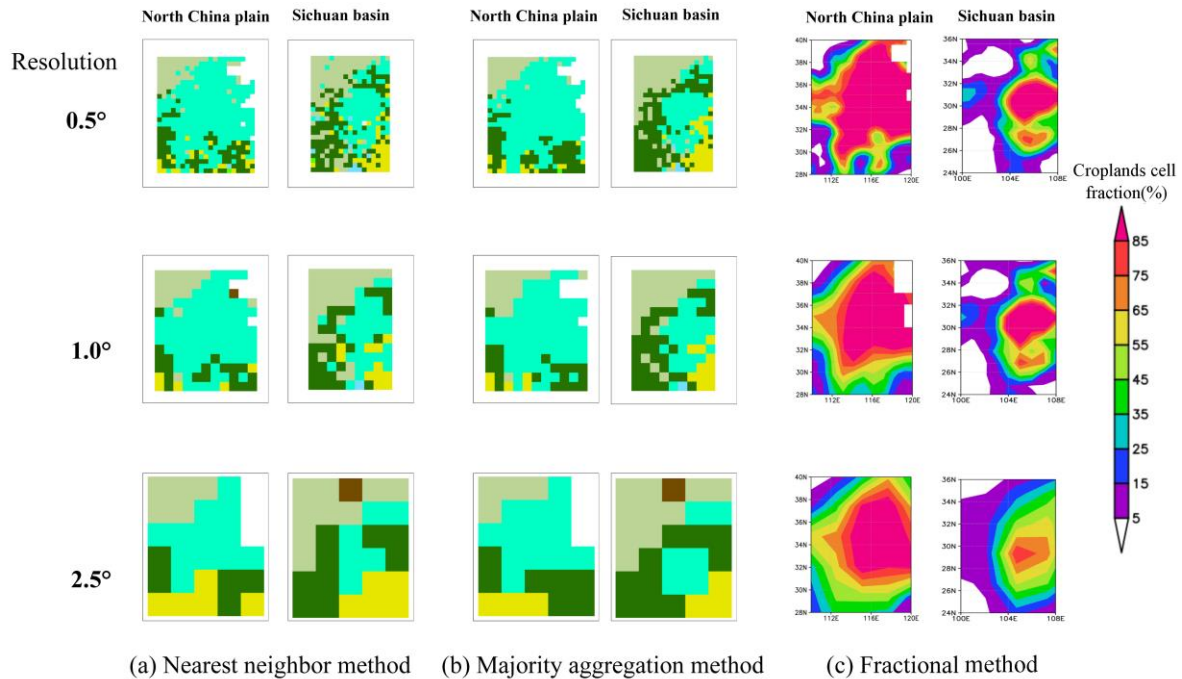
Figure 3.2. Categorical LULC and fractional maps of 2000 in North China plain and Sichuan basin at 0.5°, 1.0°, and 2.5° spatial resolution, aggregated by (a) Nearest neighbor method, (b) Majority aggregation method (Please refer to **Figure 3.1** for legend), and (c) Fractional method (Legend is the fraction of croplands in each grid cell from 0-100%)

3.3.2 Relationships of categorical and fractional LULC data with latent heat flux at different spatial resolutions in the North China plain and the Sichuan basin

The correlation coefficients for the association of fraction of croplands and latent heat flux in both the North China plain and the Sichuan basin change minimally as the spatial scale coarsened for all six years, and in each case is significant at the 1% level (**Table 3.1**). The difference in mean correlation coefficient of the six years among the values within each of these two regions is quite small (≤0.08). The significant positive correlations are associated with the increased evapotranspiration during the peak growing time of crops. In general, the correlations in the North China plain are larger than those in the Sichuan basin, which may due to the more croplands in the North China plain (**Figure 3.1**).

Table 3.1. Spatial correlations of annual fraction of croplands with August latent heat flux in 1982, 1988, 1994, 2000, 2006, and 2011 at 0.5°, 1.0°, and 2.5° spatial resolution in the North China plain and the Sichuan basin.

| Year | Correlation Coefficient, r | | | | | |
| | 0.5° spatial resolution | | 1.0° spatial resolution | | 2.5° spatial resolution | |
	North China plain	Sichuan basin	North China plain	Sichuan basin	North China plain	Sichuan basin
1982	0.50*	0.44*	0.59*	0.47*	0.53*	0.55*
1988	0.62*	0.49*	0.69*	0.56*	0.64*	0.59*
1994	0.53*	0.63*	0.62*	0.65*	0.58*	0.64*
2000	0.55*	0.44*	0.60*	0.51*	0.59*	0.54*
2006	0.65*	0.35*	0.70*	0.45*	0.70*	0.48*
2011	0.63*	0.51*	0.71*	0.57*	0.70*	0.57*
Mean	0.58	0.48	0.65	0.53	0.62	0.56

*: Significant at the 1% level.

For the relationships between categorical LULC data and latent heat flux, the distribution of latent heat flux in croplands and non-croplands is different at the 1% significance level for all six years at both the 0.5° and 1.0° scales in the North China plain and the Sichuan basin for both nearest neighbor and majority aggregation methods (**Table 3.2** and **Table 3.3**). At the 2.5° scale, the significance level varies among years in the North China plain. The difference of the distribution is significant in 2006 and 2011 and not significant in 1982 for both nearest neighbor and majority aggregation methods

(**Table 3.2**). In the Sichuan basin, the difference of the distribution is not significant at the 2.5° resolution for all six years, excepting 1994 for nearest neighbor method and 2011 for majority aggregation method, at 5% level (**Table 3.3**). In addition, the significance level decreases more in the more heterogeneous Sichuan basin than in the relative homogenous North China plain.

Table 3.2. Wilcoxon rank sum test p values for differences in the distribution of latent heat flux values over croplands and non-croplands for two spatial scaling methods in 1982, 1988, 1994, 2000, 2006, and 2011 at the 0.5°, 1.0°, and 2.5° spatial resolutions in the North China plain.

Year	*p*-value of Wilcoxon rank sum test					
	0.5° spatial resolution		1.0° spatial resolution		2.5° spatial resolution	
	Nearest neighbor	Majority aggregation	Nearest neighbor	Majority aggregation	Nearest neighbor	Majority aggregation
1982	$p < 0.01$	$p < 0.01$	$p < 0.01$	$p < 0.01$	$p = 0.51$	$p = 0.22$
1988	$p < 0.01$	$p < 0.01$	$p < 0.01$	$p < 0.01$	$p = 0.09$	$p = 0.09$
1994	$p < 0.01$	$p < 0.01$	$p < 0.01$	$p < 0.01$	$p = 0.01$	$p = 0.03$
2000	$p < 0.01$	$p < 0.01$	$p < 0.01$	$p < 0.01$	$p = 0.02$	$p = 0.07$
2006	$p < 0.01$	$p < 0.01$	$p < 0.01$	$p < 0.01$	$p < 0.01$	$p < 0.01$
2011	$p < 0.01$	$p < 0.01$	$p < 0.01$	$p < 0.01$	$p < 0.01$	$p < 0.01$

Table 3.3. Wilcoxon rank sum test *p* values for differences in the distribution of latent heat flux values over croplands and non-croplands for two spatial scaling methods in 1982, 1988, 1994, 2000, 2006, and 2011 at the 0.5°, 1.0°, and 2.5° spatial resolutions in the Sichuan basin.

Year	*p*-value of Wilcoxon rank sum test					
	0.5° spatial resolution		1.0° spatial resolution		2.5° spatial resolution	
	Nearest neighbor	Majority aggregation	Nearest neighbor	Majority aggregation	Nearest neighbor	Majority aggregation
1982	$p < 0.01$	$p < 0.01$	$p < 0.01$	$p < 0.01$	$p = 0.44$	$p = 0.41$
1988	$p < 0.01$	$p < 0.01$	$p < 0.01$	$p < 0.01$	$p = 0.07$	$p = 0.12$
1994	$p < 0.01$	$p < 0.01$	$p < 0.01$	$p < 0.01$	$p = 0.02$	$p = 0.06$
2000	$p < 0.01$	$p < 0.01$	$p < 0.01$	$p < 0.01$	$p = 0.11$	$p = 0.09$
2006	$p < 0.01$	$p < 0.01$	$p < 0.01$	$p < 0.01$	$p = 0.07$	$p = 0.08$
2011	$p < 0.01$	$p < 0.01$	$p < 0.01$	$p < 0.01$	$p = 0.17$	$p = 0.03$

In summary, the fractional method preserves the significant relationship between LULC data and latent heat flux for all six years and all three resolutions in both the North China plain and the Sichuan basin, while the nearest neighbor and majority aggregation methods cause these correlations to diminish and even become statistically insignificant at coarser scales in some years. Therefore, we recommend rescaling using fractional maps in land-atmosphere studies.

3.3.3   Fractional maps of croplands, forests, and grasslands

Based on the aforementioned analyses, the fractional method preserves the significant relationship between LULC data and latent heat flux, and the finer scale (i.e. 0.5° resolution in this study) best captures the spatial patterns. Therefore we used the fractional method to resample LULC maps to the spatial resolution of 0.5° to identify spatio-temporal changes of croplands, forests, and grasslands from 1982 to 2012 in China. Figure 3.3 shows the mean fractional maps of croplands, forests, and grasslands averaged over the period of 1982 to 2012. The maps are color-coded by the fraction of croplands, forests, and grasslands in each 0.5° grid cell. **Figure 3.3 (a)** indicates that croplands dominate in the Northeast China plain, the Hai river basin, the Yellow river basin, the Yangtze river basin, and the Sichuan basin (refer to Figure 1 for the locations of these regions). All of these regions have been recognized as important Chinese agricultural regions since the 11th century (Deng, Chuangjun and Zhikang 1983, Liu et al. 2005, Korontzi et al. 2006, Liu et al. 2010).

Forests dominate along the borders of the Northeast China, including the mountain ranges of Daxing'anling, Xiaoxing'anling, and Changbaishan, as well as southeast and southwest mountainous regions (**Figure 3.3 (b)**). This overall spatial pattern of the distribution of forests in China is consistent with the findings of Yin et al. (2015) and Fenning (2014). Grasslands are distributed in a belt, stretching from the Northeast China plain adjacent to Inner Mongolia, to the Tibetan Plateau. This region covers the major grassland regions of China, including the Hulun Buir and Xilin Gol grasslands in Inner Mongolia and the Naqu grassland in Tibet (**Figure 3.3 (c)**). The

additional grasslands identified in this study, such as the Narat and Bayinbuluke grasslands in northern Xinjiang province, in far northwestern China, were also identified by Kang et al. (2007).
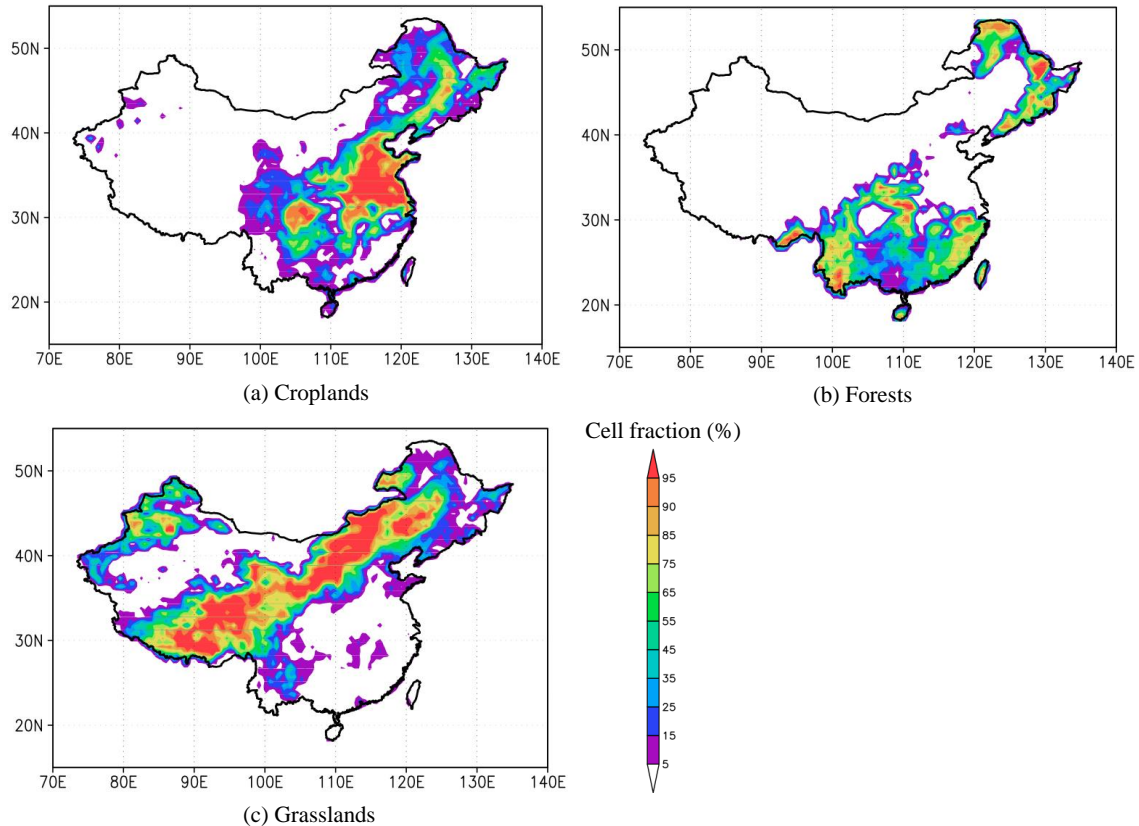
Figure 3.3. Mean fraction of (a) croplands, (b) forests, and (c) grasslands averaged over the period from 1982 to 2012. The map depicts the fraction of croplands, forests, and grasslands in each 0.5° grid cell.

3.3.4 Spatio-temporal changes of croplands, forests, and grasslands during the last three decades

The linear regression trend analysis indicates how the fraction of croplands, forests, and grasslands changed from 1982 to 2012 at each grid cell (**Figure 3.4**). The color bar represents the slope of the linear regression model over time (i.e., years) for locations where the change is statistically significant at the 5% level. Croplands significantly increased in the Northeast China plain and the Yellow river basin and decreased in the Yangtze river basin (**Figure 3.4 (a)**). The highest rate of increase, greater than 1.5%/year, occurred in the Northeast China plain. The increase in croplands

in the Northeast China plain may due to the increase in population, and the associated increase in demand for food (Liu et al. 2014). Furthermore, policy regulations, such as scrapping the agriculture tax in 2006 and increasing agricultural investment in Northeast China to improve cropland yields in 2008, as well as scientific and technological progress in agriculture, including increased access to fertilizer and irrigation, as well as the mechanization of agriculture, may also have all contributed to the increase in croplands (Man et al. 2016). There are also some small isolated areas of significantly increased croplands in the northern part of Xinjiang province, in northwestern China, which may be attributed to the successful promotion of modern agronomic technology (Liu et al. 2010, Yin 2008). The decreased croplands in the Yangtze river basin may be due to increasing forests (**Figure 3.4 (b)**), and also the expansion of industry in that region, which has resulted in arable lands being converted to built-up areas (Liu et al. 2010). The overall changing patterns of croplands, especially the increase in North China and the decrease in South China, are consistent with those in Liu, et al. (2010).

(a) Croplands

(b) Forests

Regression slope (%/year)

(c) Grasslands

58
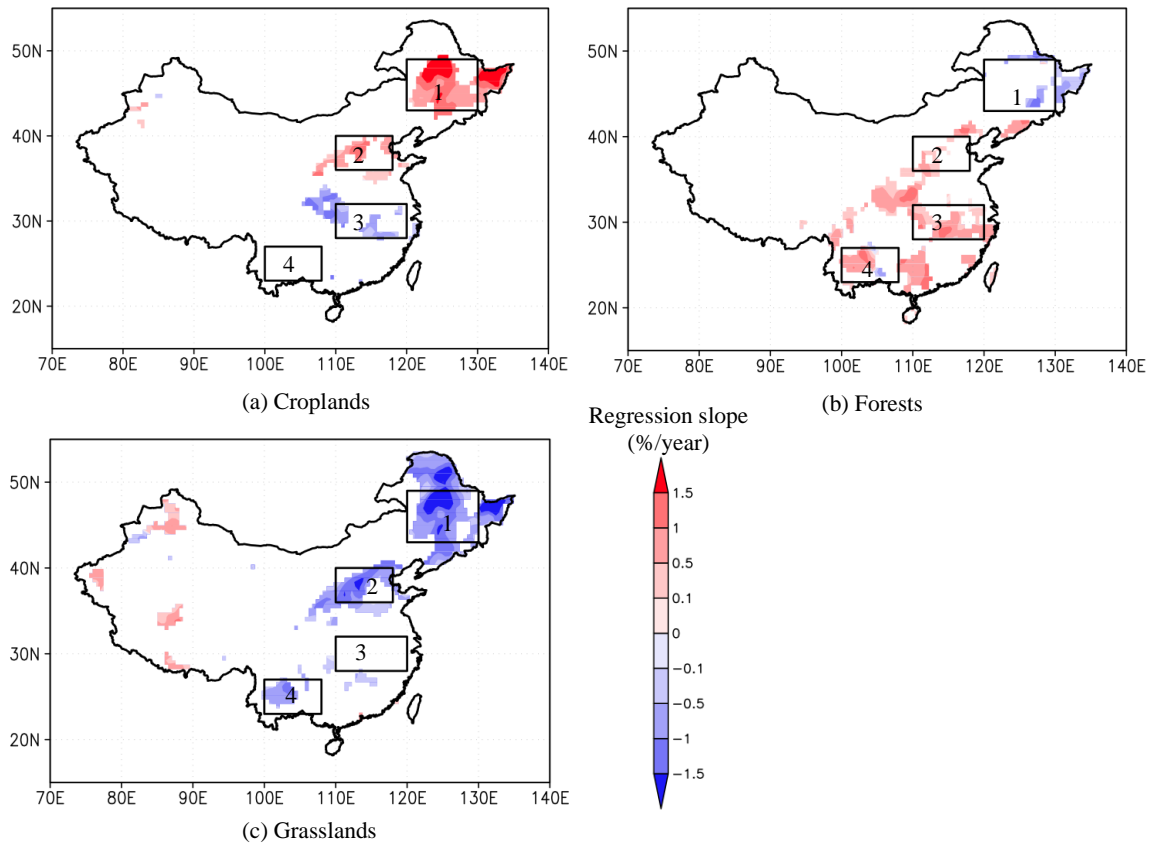
Figure 3.4. Spatial linear regression trends of fraction (%/year) for (a) croplands, (b) forests, and (c) grasslands from 1982 to 2012. The color is the slope of linear regression model. Statistically non-significant areas are masked out and significant areas at the 5% level are shaded. Rectangle 1: Northeast China plain, 2: Yellow river basin, 3: Yangtze river basin, and 4: Southwest China.

In contrast to the trend for croplands, forests significantly decreased along the borders of Northeast China, and increased in the Hai river basin, the Yangtze river basin, and Southwest China (**Figure 3.4 (b)**). The increasing trend of forest cover in the Yangtze river basin may be due to the national forest protection project after the catastrophic flood of 1998 (Liu et al. 2010) and the construction of the forest shelter-belt system (Liu et al. 2014), which converted other types of LULC, such as croplands, into forest. The increasing trend of forests in southern mountainous areas may be attributed to the "Grain for Green" program and related afforestation activities (Liu et al. 2014, Tong et al. 2018) The reclamation of forests to control sandstorms in the Hai river basin, including the cities of Beijing and Tianjin, is a likely cause of the increasing forests in areas neighboring these two cities.

Grasslands significantly decreased in the Northeast China plain, the Yellow river basin, and Southwest China, and increased in some parts of Western China (**Figure 3.4 (c)**). Grassland degradation, which is closely associated with desertification, is a long-term environmental concern in China. The main factors causing grassland degradation are over-grazing and cultivation, processes that are common in, for example, Inner Mongolia (Waldron, Brown and Longworth 2008). However, a revision of the Grassland Law in 2002, which controls all aspects of livestock grazing, may yet result in recovery of grasslands in Western China (**Figure 3.4 (c)**) (Waldron et al. 2008). The pattern of decreasing grasslands also seems to correspond with an increase in croplands and forests.

Figure 3.5 summarizes the relative frequency of fraction of croplands, forests and grasslands for grid cells where the LULCC trend is significant. The histograms show that for all three LULC types, regions with lowest fractions of LULC (i.e., 0-20%) have the

largest number of grid cells with significantly changed LULC, whether the trend is decreasing or increasing, indicating that change trends to occur in cover classes that are a minority proportion of the landscape, rather than the dominant fraction. For croplands and forests, increasing trends are the most common, even where forests and croplands already dominate. For grasslands, decreasing trends dominate, especially for areas where grasslands are a low percentage of the land cover even before the additional loss of grassland. In contrast, in areas of moderate percentages of grassland cover (40-80%), increasing and decreasing trends somewhat balance resulting in only a small net loss of grasslands in such areas.

(a)

(b)

(c)
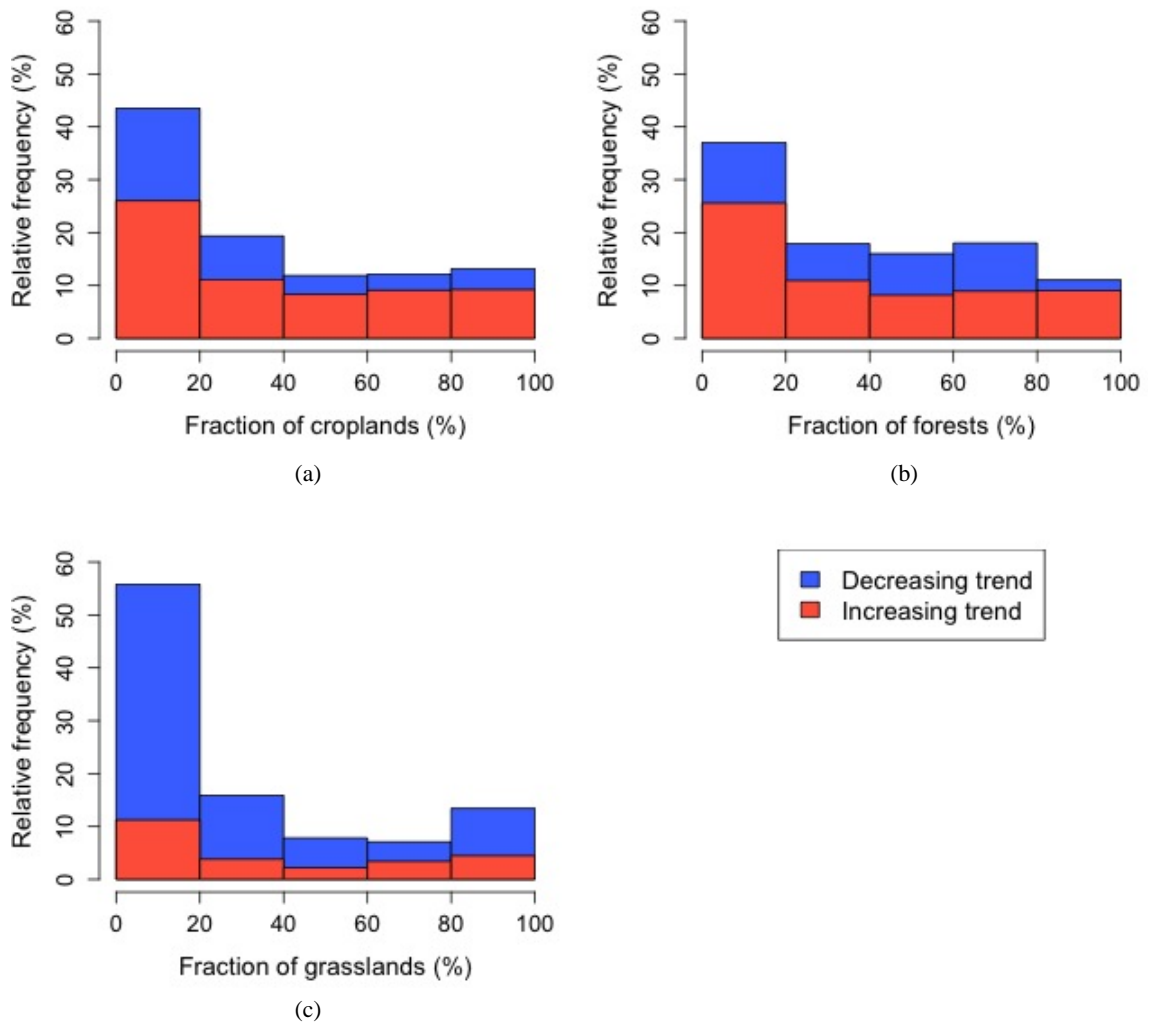
Figure 3.5. Relative frequency of fraction of (a) croplands, (b) forests, and (c) grasslands for the gird cells where the LULCC trend is significantly changed, as shaded in Figure 4.

Blue color represents significantly decreasing trend and red is significantly increasing trend.

3.3.5 Transitions between croplands, forests, and grasslands

To examine the underlying relationships among the changes in croplands, forests, and grasslands during the last three decades, we performed spatial pattern correlation analysis, drawing only on grid cells with trends significant at the 5% level. We studied the three LULC types in the selected regions (shown as rectangles in **Figure 3.4**): the Northeast China plain (Rectangle 1 in **Figure 3.4**), the Yellow river basin (Rectangle 2), the Yangtze river basin (Rectangle 3), and Southwest China (Rectangle 4). Scatterplots and spatial correlation coefficients for the linear regression trends (%/year) of croplands, forests, and grasslands are shown in **Figure 3.6**.

The spatial correlations coefficients between croplands, forests, and grasslands in the four regions show very different associations. In the Northeast China plain and the Yellow river basin, grid cells with increasing croplands generally correspond to decreasing grasslands, with a significant negative correlations of r= -0.934 in the Northeast China plain (**Figure 3.6 (b)**) and r= -0.894 in the Yellow river basin (**Figure 3.6 (e)**). Trends of increased forests are significantly correlated with trends of decreased grasslands in the Yellow river basin (**Figure 3.6 (f)**) and the Northeast China plain (**Figure 3.6 (c)**). From **Figure 3.6**, together with the spatial trends shown in **Figure 3.4**, we can draw the general inference that in the Northeast China plain and the Yellow river basin the dominant transition was replacement of grasslands by croplands. In addition, in the Yellow river basin, grasslands also appear to have been converted to forest cover, though the pattern is less strong than with croplands. In the Yangtze river basin, the only significant association is between decreasing croplands and increasing forests (r= -0.545) (**Figure 3.6 (g)** and **Figure 3.4**). In Southwest China, the transition between forests and grasslands has the strongest association (r= -0.668) (**Figure 3.6 (l)**), followed by a transition between croplands and forests (r= -0.433) (**Figure 3.6 (j)** and **Figure 3.4**).
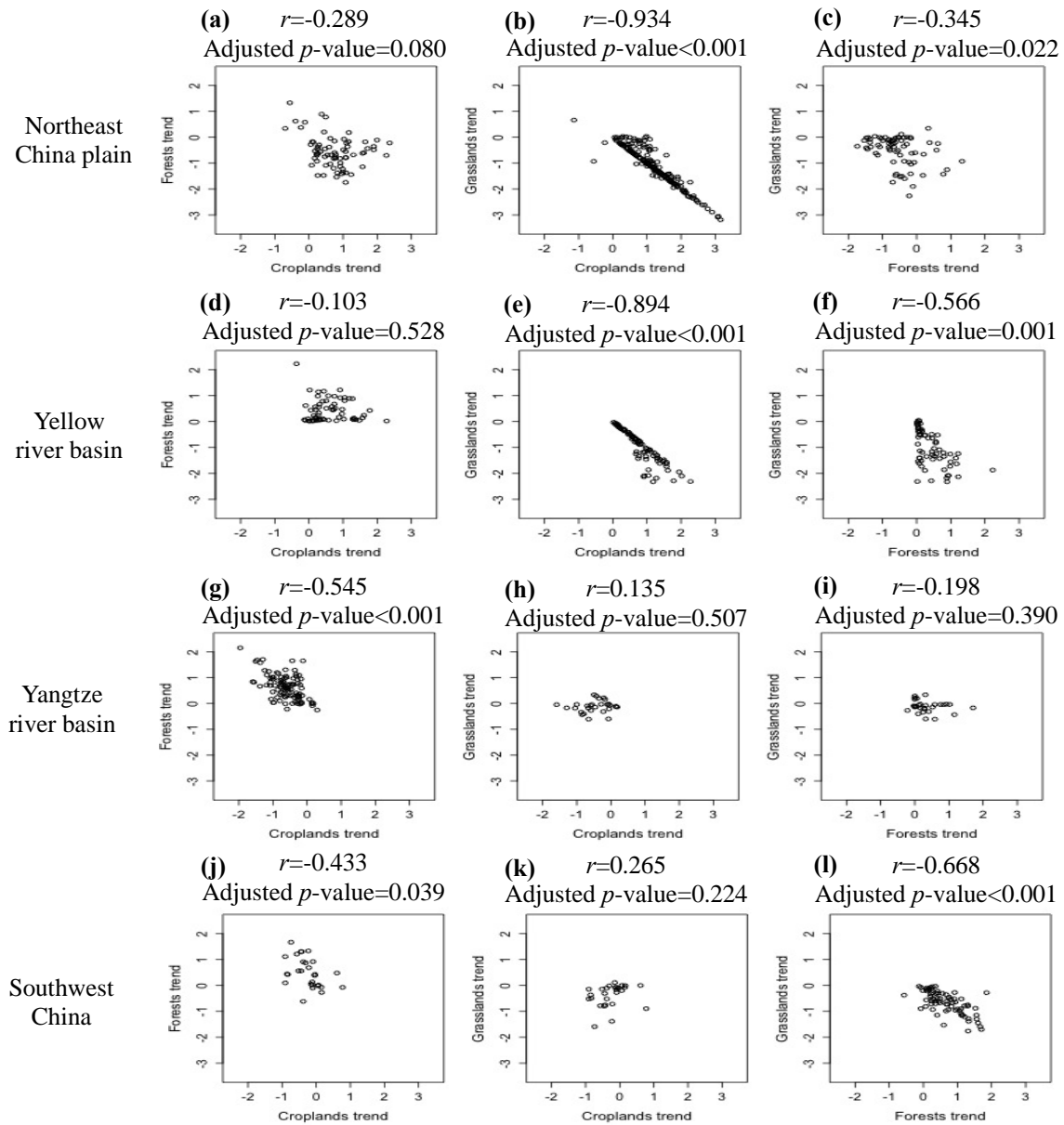
Figure 3.6. Scatterplots and spatial correlation coefficients among the trends of croplands, forests, and grasslands for the four selected regions shown in Figure 4. Each data point represents the significant trends at the 5% level over the 31-year for a particular $0.5°$ grid cell.

3.4 Summary

Remotely sensed LULC maps have been widely used in land-atmosphere interaction studies, and this research identified key uncertainties related to scale mismatches in the spatial and temporal domains. Both categorical LULC maps and fractional maps capture the overall pattern of croplands in the relatively homogenous North China plain and the comparatively heterogeneous Sichuan basin at all of the three spatial resolutions studied (0.5°, 1.0°, and 2.5°). The significant positive correlation between fraction of croplands and latent heat flux in August of 1982, 1988, 1994, 2000, 2006, and 2011 at the three spatial resolutions is quite similar in the two study areas, although the difference in r values between 0.5° and 2.5° is greater in the Sichuan basin than in the North China plain. For the categorical LULC maps, the distribution of latent heat flux values over croplands and non-croplands is significantly different at the 1% level at the 0.5° and 1.0° spatial resolutions for both nearest neighbor and majority aggregation methods in North China plain and Sichuan basin for all of the six years. However, at the 2.5° spatial resolution, the significance level varies among years. Nevertheless, both the nearest neighbor and majority aggregation methods are particularly problematic in regions with more heterogeneous, fine-grained spatial patterns of LULC. In contrast, for both the relatively homogeneous North China plain and heterogeneous Sichuan basin, the fractional maps preserved the relationships between LULC data and latent heat flux at all the spatial scales. Therefore, we recommend rescaling using fractional maps in observational land-atmosphere studies. In summary, the fractional scaling method preserves significant correlations among LULC data and latent heat flux at all three studied scales (0.5°, 1.0°, and 2.5°), while nearest neighbor and majority aggregation methods cause these correlations to diminish and even become statistically insignificant at coarser scales.

Based on the optimal spatial scaling method, this study explored spatio-temporal changes in croplands, forests, and grasslands from 1982 to 2012 through 31-year LULC maps, which were aggregated to 0.5° using the fractional method. The annual LULC maps enable a time-series analysis of changes in LULC, which is the key attribute compared to the previous LULCC studies of China. Croplands significantly increased in

the Northeast China plain and the Yellow river basin, and decreased in the Yangtze river basin. Forests significantly decreased along the border of Northeast China, and increased in the Yangtze river basin and Southwest China. Grasslands significantly decreased in the Northeast China plain, the Yellow river basin, and Southwest China, and increased in some parts of Western China. The analysis of transitions among significant changes in croplands, forests, and grasslands shows that decreasing grasslands in the Northeast China plain and the Yellow river basin are significantly associated with increasing croplands. Similarly, increasing forests in the Yangtze river basin are significantly associated with decreasing croplands. In Southwest China, decreasing grasslands and, to a lesser extent, decreasing croplands, are significantly correlated with the increasing forests.

The time-series analysis of annual LULC maps in China suggests a complex pattern of spatio-temporal changes in croplands, forests, and grasslands from 1982 to 2012. The analysis facilitates the identification of regions where change is extensive and statistically significant, such as North China, where croplands have increased significantly, and South China, where forest have increased significantly. Compared to previous studies, which relied on overlaying LULC maps covering a short-time period (Fan, Weng and Wang 2007), the statistically significant patterns of spatio-temporal changes from our study provide a robust approach for capturing LULCC in China.

The identified LULCC patterns in this study have the potential to influence the regional climate in China. The increasing forest in the Yangtze river basin and Southwest China, associated respectively with decreasing of croplands and grasslands, is likely decreasing the region's albedo, because of the higher albedo of croplands and grasslands, compared to forest. A decreased albedo would induce higher net radiation, and consequently promote higher temperatures (Bonan et al. 1992). On the other hand, the conversions from croplands and grasslands to forests may reduce surface air temperature due to the cooling effects from the higher evapotranspiration of forest (Li et al. 2015, Betts 2011). The transitions of LULC types within the regions of extensive significant LULCC revealed by this study can potentially alter surface heat and moisture conditions

and thereby induce changes in the regional climate system. Previous studies have explored the climatic impacts of LULCC in China. For examples, Cao, *et al.* [24] used the weather research and forecasting (WRF) model to investigate how different LULCC types affect regional climate in the ago-pastoral transitional zone of North China. Ma et al. (2013b) simulated afforestation impacts on the regional climate in Jiangxi province, China using WRF. Fu (2003) applied a regional integrated environmental model system (RIEMS) to investigate the effects of human-induced land cover change on the East Asia monsoon. However, most previous studies have not been able to incorporate long-term temporal LULCC patterns due to lack of long-term time-series LULC data. Incorporating long-term LULCC pattern, such as that produced in this study, could therefore be useful for future empirical and modeling studies investigating how LULCC affects regional climate.

4 Observational cooling effects of croplands expansion in the troposphere over Northeast China during late growing season*

* To be submitted to *Geophysical Research Letter*

4.1 Introduction

Northeast China is one of the agriculture heartlands of China (USDA 2016, Sun et al. 2007, Ye and Fang 2009). With good soil quality, Northeast China accounts for almost 20% of the total grain production in China (Yang et al. 2014). In the past four decades, summer and autumn rainfall in Northeast China has significantly decreased (Piao et al. 2010, Ye 2014, Wang et al. 2015), resulting in severe drought. In 2014, a drought in Liaoning Province of Northeast China affected 1.8 million hectares of crops (Yi 2014). Irrigation has been practiced to mitigate the negative effects of drought in crop production (Yin et al. 2016, Chen et al. 2017). The irrigated area has increased from 27,000 ha in 1995 to 667,000 in 2005 in western part of Jilin province in Northeast China (Li et al. 2005). The human-induced land use and land cover changes due to the expansion and intensification of agricultural practices might affect heat and moisture fluxes which could influence regional climatic conditions. Northeast China as the largest plain of China is surrounded by the mountains of Daxing'anling Mountain in the west, Xiaoxing'anling Mountain in the north, and Changbai Mountain in the east. Considering the isolated geography to the surrounding oceans, Northeast China is an ideal place to explore the land-atmosphere interaction associated cropland expansion.

Both modeling and observational studies have shown that agriculture practices, including conversion of non-croplands to croplands and intensification of irrigation or fertilization, could significantly impact the climate system through biogeophysical and biogeochemical processes in the land-atmosphere interaction (Cook, Puma and Krakauer 2011, Mahmood et al. 2006, Wei et al. 2013, Lee et al. 2011, Lobell, Bonfils and Faurès 2008, Zhao et al. 2016). Agriculture activities may reduce surface air temperature through altering the Bowen ratio from sensible to latent heat flux (Bonan 2001, Han and Yang 2013), increasing moisture content in the atmosphere by increasing the

transpiration rate (Zhang et al. 2013), and decreasing monsoon rainfall by reducing the land-ocean heat contrast (Lee et al. 2009, Puma and Cook 2010). With irrigated and dry simulations using a regional atmospheric model of the U.S. High Plains, Adegoke et al. (2003) found a 15% decrease in sensible heat flux and 36% increase in latent heat flux, and thereby 1.2°C decrease in the near-ground temperature. From an observational perspective, Zhang et al. (2013) showed that the wetting effects of cropland greenness changes accounted for about 48% of the spatial variance of daily minimum specific humidity change for the spring in the North China Plain. Puma and Cook (2010) explored the effects of irrigation on the global climate during the 20th century using an atmosphere general circulation model and found precipitation increased downwind of major irrigation areas, and decreased in India due to a weaker summer monsoon. A modeling study of the impact of agriculture intensification and irrigation on land-atmosphere interactions indicated that irrigation caused reduction in the surface temperature and led to a modified regional circulation pattern and changes in mesoscale precipitation (Douglas et al. 2009).

The observational evidence of cooling effect of agriculture activities in near-surface atmosphere in China has been documented. By using 90 meteorological stations, Han and Yang (2013) found the trends in daily average surface temperature for May-September were expected to decrease by -0.018 ^{o}C per decade along with a 10% increase in cultivated land proportion over Xinjiang, Northwest China. Zhu, Liang and Pan (2012) found the difference in the magnitude of daytime land surface temperature between areas with irrigation percentages of more than 50 and less than 50, was as high as 2.7 K during the driest year over Jilin, Northeast China. Zhao et al. (2016) stated the stations with large cultivated land fraction experienced a less significant increase in air temperature, especially in daily maximum temperature during growing season from May to September in Northeast China. Although the near-surface cooling effect of enhanced agricultural activities have been observed, how agriculture activities can influence the climatic conditions in the mid and upper troposphere is rarely studied through observational perspective and to our knowledge it has not yet been explored in China.

Another limitation in many previous observational studies is access to multi-temporal data to detect the year-to-year as well as long-term variations of cropland cover. Consequently, previous studies have used a map of a specific year to represent the croplands of the entire study period (Zhu et al. 2012, Han and Yang 2013, Zhang et al. 2013). This may ignore the tremendous change in agriculture practices, such as croplands expansion or abandonment, leading to uncertainties in estimating of the climatic effects of agriculture activities. The impacts of agriculture activities on climate might be overestimated or underestimated. Therefore, observational studies with more realistic croplands variations derived from more robust data (e.g., remotely sensed imagery) over longer temporal periods are needed to better understand the climatic effects of agriculture activities.

This study applied a newly developed, 29-year continuous annual land use and land cover maps from 1982 to 2010 derived from remotely sensed data to extract cropland cover change information in Northeast China. Based on the identified significantly changed regions, this study explored the impacts of agriculture activities on atmospheric conditions in the Northeast China during the late growing season (August and September: AS) not only near the surface but also in the mid and upper troposphere.

4.2 Data and Methods

4.2.1 Data

Annual fractional maps of croplands were used to detect croplands change in Northeast China. Fractional maps of croplands were generated from a time-series of land use and land cover (LULC) maps from 1982 to 2013 produced by He et al. (2017), using a random forest classification based on 19 phenological metrics derived from AVHRR Global Inventory Modeling and Mapping Studies (GIMMS) third generation NDVI (NDVI3g) data. The consistency values between AVHRR LULC maps and Moderate Resolution Imaging Spectroradiometer (MODIS) LULC maps for the years 2001-2012 range from 69.3% to 72.5%, and the overall accuracy of the 2012 LULC map was 73.8%. The LULC maps have a spatial resolution of $1/12°$. We displayed LULC map of the Northeast China in 2012 as an example (**Figure 4.1 (a)**). We aggregated the 32-year

LULC maps to 0.5^0 using a fractional method, as a fractional method preserves the significant relationship between LULC data and climate variable in China (He et al. 2018). In doing so, this study generated fractional maps of croplands from 1982 to 2013.
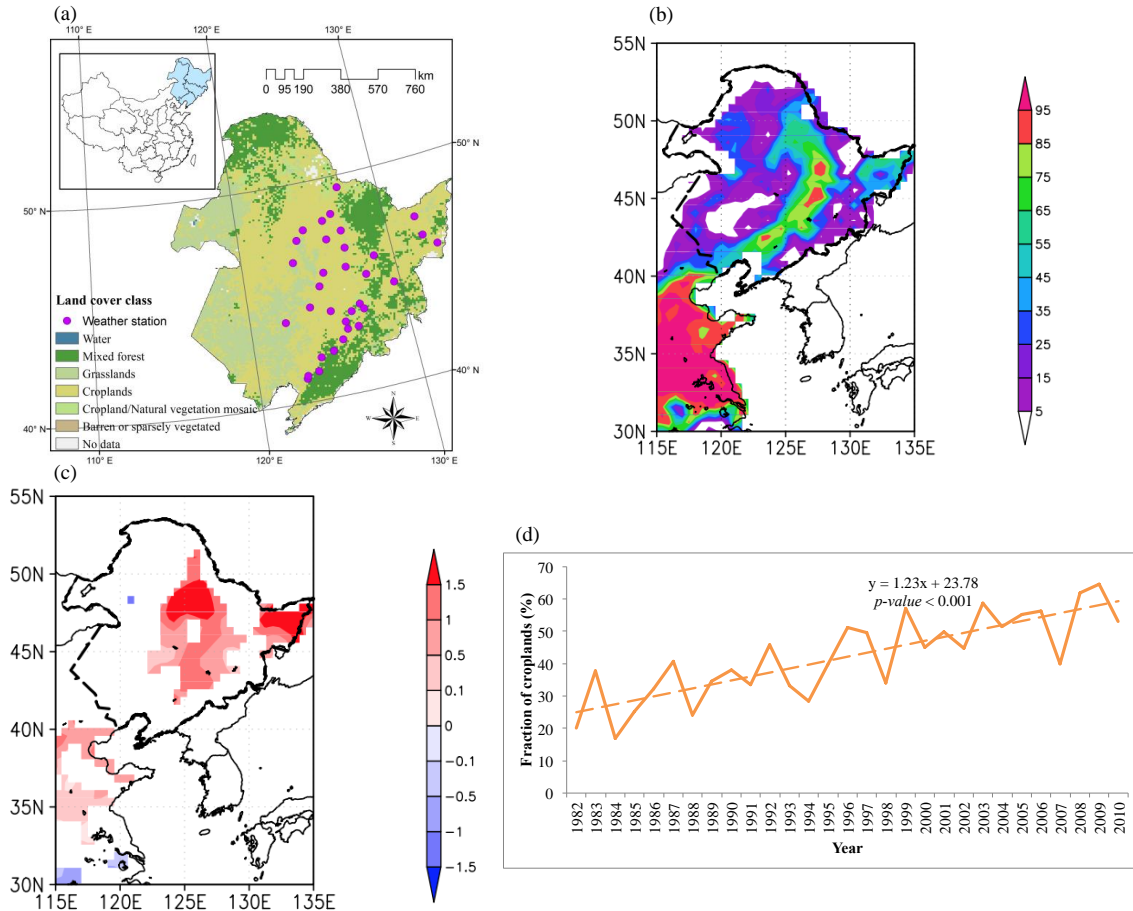
Figure 4.1. (a) The location of Northeast China (the background is land use and land cover map in 2012 from (He et al. 2017)), (b) mean fraction of croplands averaged over the period from 1982 to 2010 (the color bar is the fraction of croplands in each 0.5° grid cell), (c) spatial linear regression trend of fraction (%/year) for croplands from 1982 to 2010 (the color bar is the slope of linear regression model, statistically non-significant regions were masked out and only pixels significant at the 10% level are shown in the map), and (d) temporal linear regression trend of fraction for croplands from 1982 to 2010 (the fraction of croplands was area-averaged for each year over the regions with significantly increased croplands in Northeast China, as shown in Figure 4.1 (c)). The black dashed polygon in (b) and (c) indicates the Northeast China study region.

Daily mean of surface air temperature ($^{\circ}$C) date from Chinese Meteorological Data Sharing Service System of the China Meteorological Administration (CMA) were used to calculate the averaged AS temperature in Northeast China at each weather station. This dataset includes records from January 1954 to July 2011 (Meng et al. 2014) for approximately 120 weather stations in Northeast China. To determine the influence of croplands expansion on mid and upper level atmospheric conditions, we used temperature (^{0}K) and geopotential height (m^2/s^2) data at different pressure levels (27 levels from 1000 to 100 hPa) from European Center for Medium-Range Weather Forecasts (ECMWF) re-analysis (ERA)-Interim. ERA-Interim uses sets of observations and boundary forcing fields acquired for ERA-40 through 2001, and from ECMWF operations hereafter. ERA-Interim also utilizes other data sources, such as European Remote Sensing Satellite (ERS) altimeter wave heights and European Organisation for the Exploitation of Meteorological Satellites (EUMETSAT) reprocessed winds and clear-sky radiances (Dee et al. 2011). ERA-Interim covers the period from 1979 onwards with spatial resolution of 0.703°. The monthly data was used in this study. In order to explore physical mechanisms linking croplands expansion to climate, we used latent heat flux and sensible heat flux derived from FluxNet-Multi-Tree Ensemble (MTE). Fluxnet-MTE datasets are based on remotely sensed indices, climate and meteorological data, and information on land use (Jung et al. 2011). The spatial resolution of Fluxnet-MTE datasets is 0.5° by 0.5°, over the period 1982 to 2011.

The common periods of 1982 to 2010 of these datasets were used in this study. The unit of ERA-interim temperature ($^{\circ}$K) and geopotential height (m^2/s^2) is converted to $^{\circ}$C and geopotential meter (m), respectively. The latent heat flux and sensible heat flux were extracted at weather stations.

4.2.2 Statistical Methods
Linear regression analysis

Linear regression analysis is a statistical method for analyzing the relationship between two or more variables by evaluating the degree to which one variable can be predicted or explained by the others (Freund et al. 2006). In this study, we performed linear regression trend analysis to determine the spatio-temporal changes of croplands in

Northeast China at each grid point. We were interested in the slope of the regression line, which characterizes how the dependent variable (i.e., fraction of croplands) changes over time. The significantly changed regions for croplands in Northeast China are thereby determined.

We also applied linear regression analysis for croplands fraction with latent heat flux, sensible heat flux, and surface temperature in order to determine the magnitude of impacts of croplands expansion on these variables. The dependent variable is the area-averaged croplands fraction at all grid points of weather stations over the significantly increased regions. The area-averaged latent heat flux, sensible heat flux, and surface temperature over the same grid points were used as an independent variable, respectively. Both independent and dependent variables were detrended by subtracting n* slope from their original values (n is 1, 2, 3, . . . , 29). The slopes were estimated from linear regression trend analysis. The significance of linear regression was estimated using a Student's *t* test.

Detrended correlation analysis

This study applied correlation analysis (Pearson correlation coefficients) to examine relationships of the croplands fraction with the climatic variables from near the surface to top of the troposphere, including latent heat flux, sensible heat flux, surface air temperature, multi-level temperatures, and geopotential height, during the late growing season of AS. The trends in the cropland and climate variables were removed using the detrended method as described above. The significances of correlation coefficients were tested by Student's *t* test.

Detrended composite analysis

Composite difference analysis is a sampling technique based on the conditional probability of a certain event occurring (NOAA 2005). Composite analysis is commonly combined with correlation analysis to explore relationship between two variables (Grantz et al. 2005). In this study, we defined the eight high (top 25th percentile) years of detrended croplands fraction as the conditional event. Composite differences of

71

temperature and geopotential height at 850, 500, and 300 hPa were calculated by subtracting the mean value for the eight high years from the climatological mean value for the 29 years of study period. Composite difference analysis was applied to each grid cell. The significance for composite difference analysis was also estimated using a Student's *t* test.

Granger causality test

Granger-causality test could be used to assess potential causality among different variables. Granger-causality was defined by Granger (1969) as follows: A variable *Y* is Granger-causal for another variable *X* if knowledge of the past history of *Y* is useful for predicting the future state of *X* over and above knowledge of the past history of *X* itself. So if the predicting of *X* is improved by including *Y* as a predictor, then *Y* is said to be Granger-causal for *X*. Granger-causality test have been widely used in climate studies (Jiang, Liang and Yuan 2015, Elsner 2007, He and Lee 2016). In this study, we explored the granger causal associations of croplands fraction with near surface temperature.

4.3   Results and Discussion

4.3.1   Croplands expansion in Northeast China

Within Northeast China, cropland cover varies from less than 5% to over 85%, with the highest values (>55%) concentrating in the east (**Figure 4.1 (b)**). Croplands significantly increased in the central part of Northeast China, with the highest value of an increase of 1.5%/year in the north and east parts (**Figure 4.1 (c)**). The temporal trend of fraction in Northeast China for cropland cover shows croplands increased around 1.23%/year (**Figure 4.1 (d)**) in the regions with significantly increasing croplands. The time-series of croplands fraction was area-averaged over the regions with significantly increased croplands in Northeast China as shown in **Figure 4.1 (c)**.

4.3.2   Impacts of croplands expansion on near-surface climate in Northeast China

As 33 stations among 120 weather stations in Northeast China fall into the region with significantly increased croplands (**Figure 4.1 (c)**), this section only focuses on these 33 stations (**Figure 4.1 (a)**). **Figure 4.2** shows the spatial patterns of correlations between

detrended time-series of croplands fraction with detrended latent heat flux, sensible heat flux, and surface temperature in each station during the late growing season. Most of the stations show that the fraction of croplands is positively correlated with latent heat flux, including a significant correlation in the central and southern parts of Northeast China (**Figure 4.2 (a)**). Correspondingly, the fraction of croplands has a negative correlation with sensible heat flux over the majority of the stations (**Figure 4.2 (b)**). There is a negative relationship between fraction of croplands and surface temperature during the late growing season (**Figure 4.2 (c)**), demonstrating the cooling effects of croplands expansion.

(a)

(b)

(c)
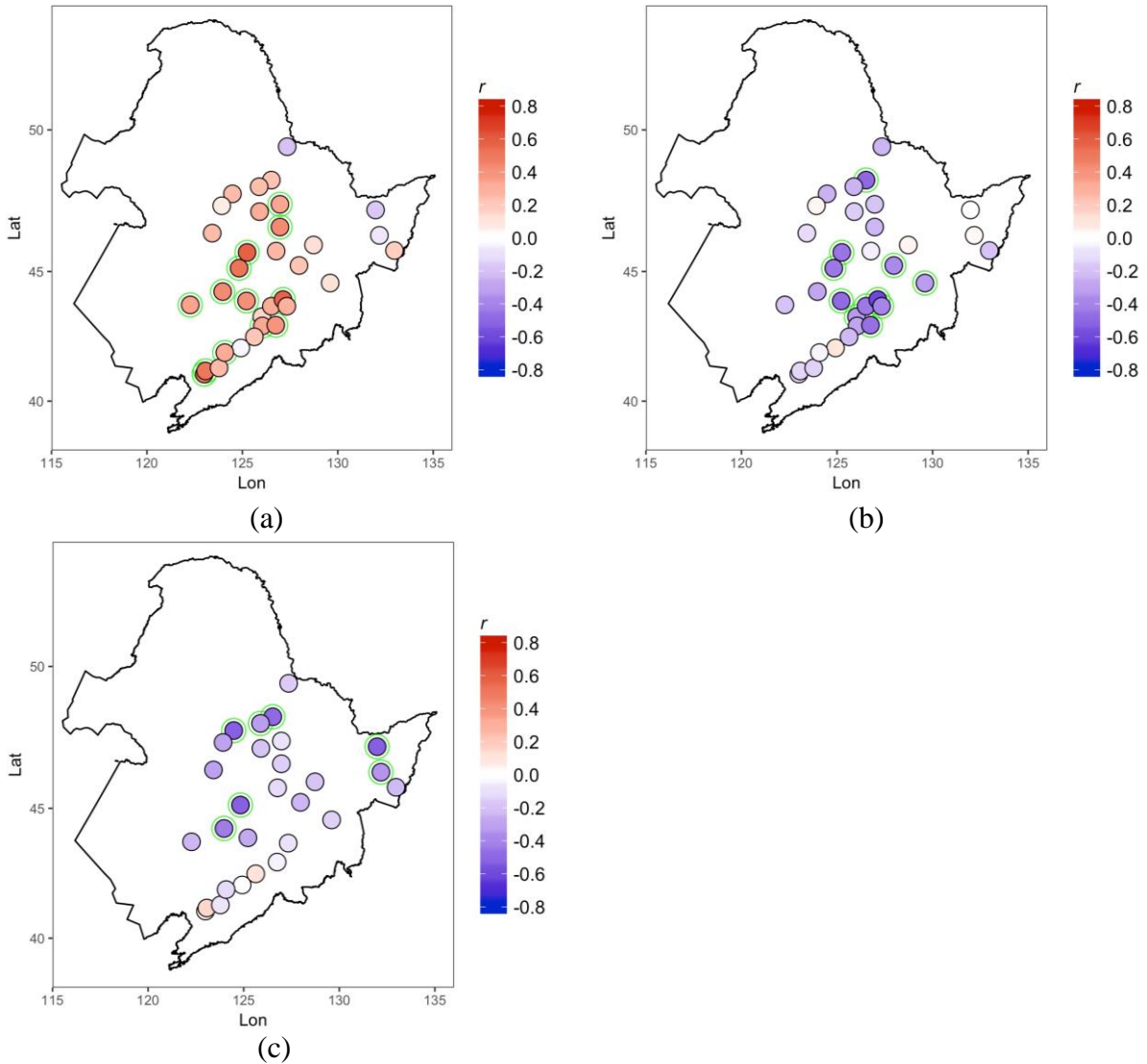
Figure 4.2. Correlation patterns of detrended time-series of croplands fraction from 1982 to 2010 with detrended (a) latent heat flux, (b) sensible heat flux, and (c) surface temperature at each station point during the late growing season of AS. The green circle is significant at 10% level.

To determine the magnitude of croplands expansion impacts on heat fluxes and surface temperature, we then conducted linear regression analysis for croplands fraction with latent heat flux, sensible heat flux, and surface temperature, respectively (**Figure 4.3**). The croplands fraction, latent heat flux, sensible heat flux, and surface temperature during AS were averaged over the 33 weather stations. The latent heat flux increases 0.76 W/m^2 along with a 10% increase in croplands, while the sensible heat flux and surface temperature decrease 0.58 W/m^2 and 0.21 ^{o}C, respectively.
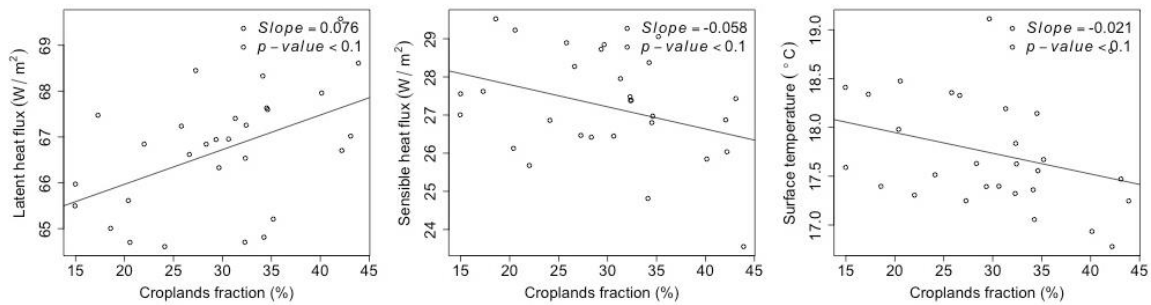
Figure 4.3. Linear associations of croplands fraction with latent heat flux, sensible heat flux, and surface temperature.

The causal association between croplands expansion and surface temperature cooling was tested by Granger-causality analysis. As shown in Test 1 in **Table 4.1**, the null hypothesis that croplands fraction does not granger-cause surface temperature is rejected at 10% significance level (p-value = 0.067), which indicates that croplands expansion does granger-cause surface cooling in Northeast China.

Table 4.1. Granger-causality test between croplands fraction with AS surface temperature.

Model	Residual Df	Df	F-statistic	P-value
Test 1: AS temperature ~ AS temperature + croplands fraction				

Unrestricted	25			
Restricted	26	1	3.67	0.067

4.3.3 Impacts on upper-level climate in Northeast China

The cooling effect of croplands expansion is not confined to the near-surface atmosphere, but it spreads vertically. **Figure 4.4 (a)** shows the spatial patterns of correlations between detrended time-series of area-averaged croplands fraction over the regions with significantly increased croplands (**Figure 4.1 (c)**) with detrended temperature in each grid cell at the 850, 500, and 300 hPa levels over the northern East Asia, respectively. The fraction of croplands is negatively correlated with temperature from lower (850 hPa) to upper troposphere (300 hPa) in the Northeast China. The negative correlation is significant in the north part of Northeast China at 5% level (**Figure 4.4 (a)**). The spatial patterns of multi-level temperatures from detrended composite analysis are consistent with those from correlation by indicating the significant cooling at the 850, 500, and 300 hPa levels during the years of high croplands fraction (**Figure 4.4 (b)**).
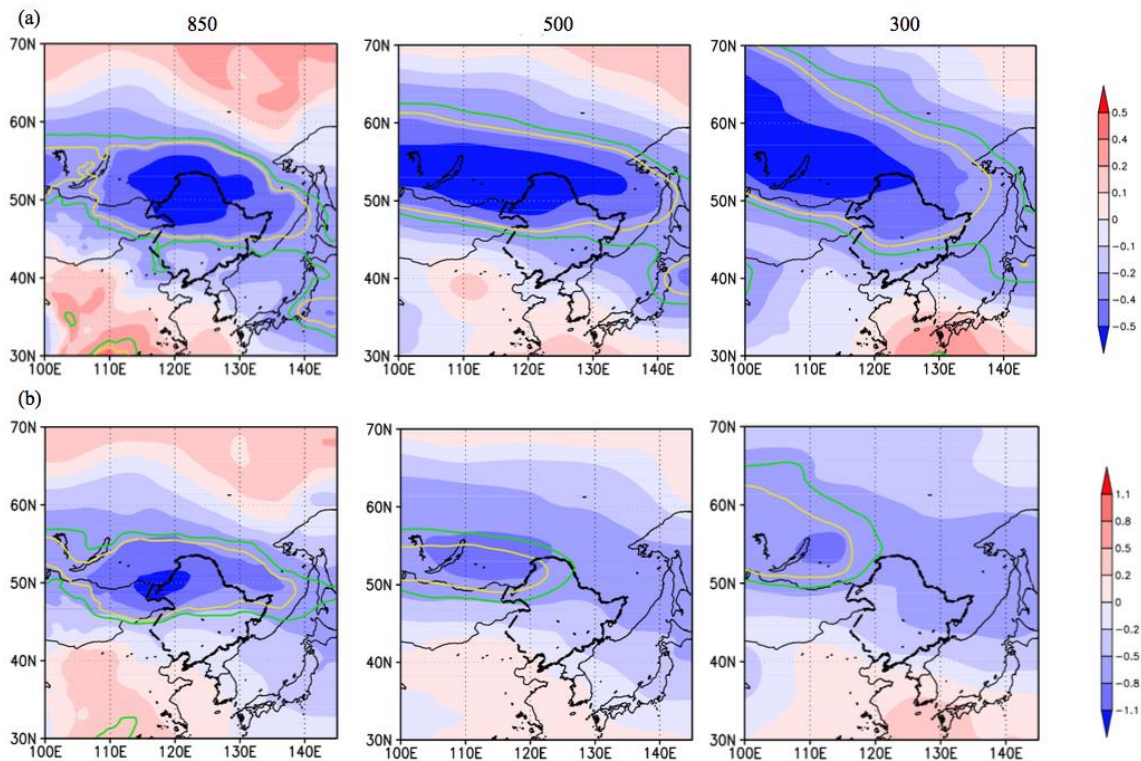
Figure 4.4. (a) Correlation patterns of detrended time-series of croplands fraction, area-averaged over the regions with significantly increased croplands from 1982 to 2010, with detrended temperatures and (b) composite differences patterns for temperature (°C) between eight high detrended croplands fraction years and 29 years of study period, at the 850, 500, and 300 hPa levels at each grid point during the late growing season of AS. The yellow contour is the 5% significant level and the green contour is the 10% significant level. Black dashed polygon indicates the Northeast China study region.

At the mid (500 hPa) and upper (300 hPa) levels, there are a negative relationship of the fraction of croplands with geopotential height in the Northeast China, with significant regions at 10% level in the central and northern parts, during AS (**Figure 4.5 (a)**). At the lower level (850 hPa), the significant negative correlation at both 10% and 5% levels is in the northern region of Northeast China. The spatial patterns of composite difference are consistent with the spatial correlation patterns by indicating the significantly reduced geopotential height at the troposphere during the years of high croplands fraction compared to climatological mean (**Figure 4.5 (b)**).
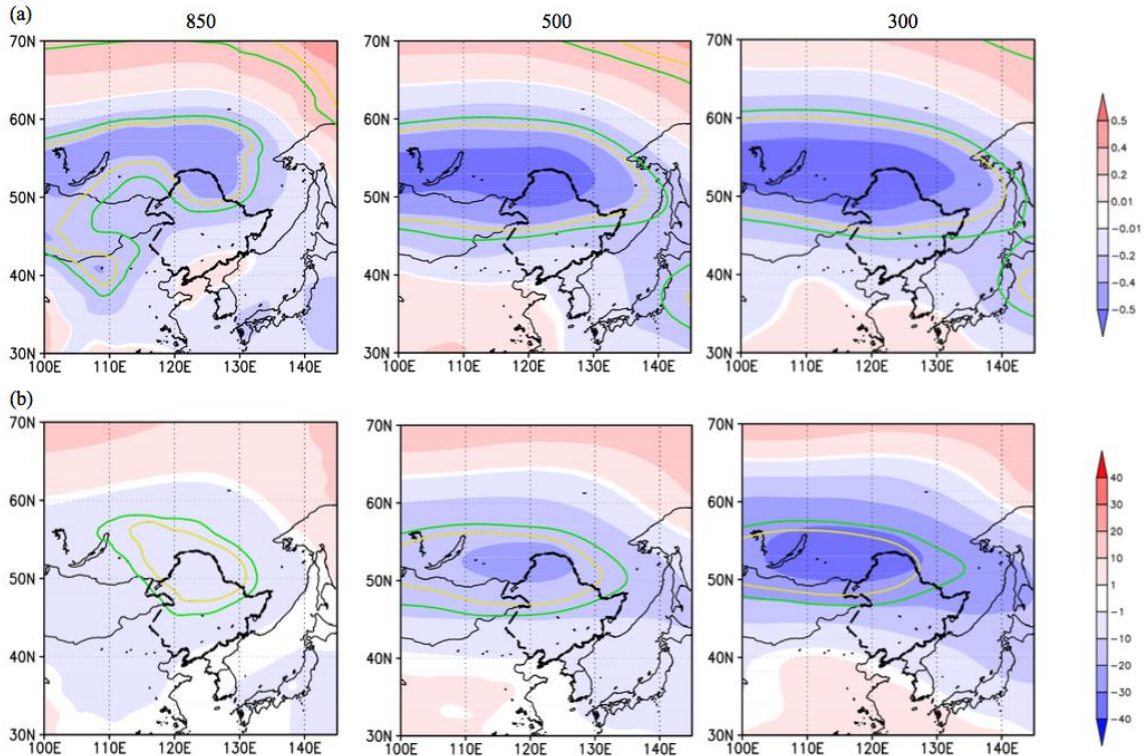
Figure 4.5. Same as in Figure 4.4 but for geopotential height (m).

Meridional vertical cross sections of correlations of croplands fraction with temperature and geopotential height are shown in **Figure 4.6**. They are zonally averaged over the regions with significantly increased croplands (122°E ~ 135°E). In the Northeast China, the significantly negative correlation between croplands fraction and temperature extends up to top of the troposphere (200 hPa). Interestingly, inverse correlation (significant positive correlation) was observed in the lower stratosphere (above 200 hPa). Correspondingly, there are significantly negative correlations between croplands fraction and geopotential height at the entire troposphere, especially mid- and upper-levels. The significantly decreased geopotential height with increased croplands fraction could be explained by compressed air column due to the significant cropland-induced cooling in the troposphere (Pielke et al. 1998). The modeling study showed that the irrigation-induced cooling in the lower troposphere could significantly reduce the geopotential height in the upper troposphere over the Middle East and central Asia, the High Mountain Asia, and Huang-Huai-Hai plain in China (Yang et al. 2016, de Kok et al. 2018, Lee et al. 2011). The observed patterns of vertical cross sections support the tropospheric cooling effects of cropland expansion over Northeast China and consequent lower geopotential height over the northern East Asia.
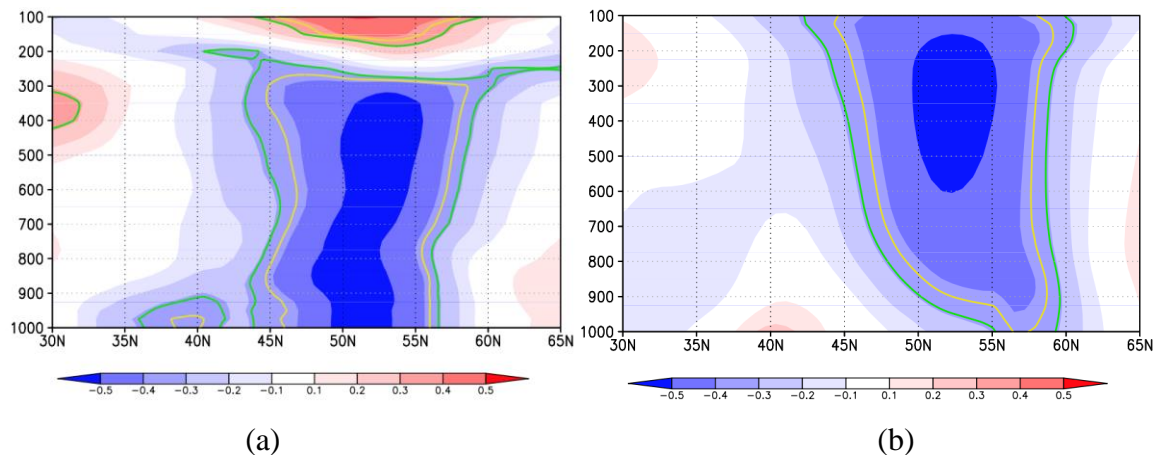
**Figure 4.6.** Meridional cross sections of correlation patterns of detrended time-series of croplands fraction, area-averaged over the regions with significantly increased croplands from 1982 to 2010, with (a) temperature and (b) geopotential height zonally averaged

over 122°E~135°E for AS. The yellow contour is the 5% significant level and the green contour is the 10% significant level.

4.4   Summary

The land surface condition is one of the important factors in determining regional climate system. The changed land surface conditions (e.g. albedo, soil moisture, surface roughness, and leaf area index) due to land use and land cover change (LULCC) have brought significant impacts to the regional climate system. Understanding the influences of LULCC on regional climate can greatly improve predictive skills in seasonal climate forecasting (Lee, Chase and Rajagopalan 2008), which could benefit the end-users including famers and water resources managers.

This study examined the impacts of croplands expansion on regional climate in Northeast China during later growing season over the last three decades. By using a newly developed 29-year time-series of land use and land cover maps, this study found croplands significantly increased in Northeast China, at an average increasing rate of 1.23%/year (**Figure 4.1(d)**). This croplands expansion is highly correlated with increased latent heat flux and decreased sensible heat flux in Northeast China (**Figure 4.2 (a)** and **(b)**), which leads to decreasing surface air temperature in this region (**Figure 4.2 (c)**). The cooling effect of croplands expansion in near surface atmosphere has been documented in the previous observational studies, while the magnitude of cooling captured by this study is more reliable compared to the previous studies, as their studies were only based on one year map to indicate cropland cover, which overlooks its dynamics. This study further explored the impacts of croplands expansion on mid and upper atmospheric conditions, and found the cooling effects of croplands expansion extent up to top of the troposphere and thereby decrease the geopotential height. The observed results suggest that expansion and intensification of agricultural practices could influence regional climatic conditions through cropland-induced cooling as well as the resultant lower height in the troposphere. The lower geopotential height in the upper troposphere may alter upper-level atmospheric circulation, such as Asian jet, which may subsequently induce a large impact on Asian climate (Lee et al. 2011).

5 Conclusions and future study

5.1 Conclusions

This dissertation addresses three research gaps in current LULCC-atmosphere interaction studies: 1) a lacking of long-term continuous LULC maps, 2) a spatial scale mismatch between LULC data and climate data, and 3) limited understanding in observational studies related to climatic effects of croplands expansion. To address the first research question, this dissertation produced a continuous series of annual LULC maps of China from 1982 to 2013 using random forest classification of 19 phenological metrics derived from AVHRR GIMMS NDVI3g data. The classifier was trained using reference data derived from the MODIS land cover type product (MCD12Q1). Based on a comparison with Google Earth images, the overall accuracy of a simplified eight-class version of our 2012 LULC map is 73.8%, which is not significantly different from the accuracy of the MODIS map of the same year.

To fulfill the second research question, I explored the effect of three spatial scaling methods, nearest neighbor method, majority aggregation method, and a fractional method, on correlations among LULC data and a land surface climatic variable, latent heat flux. Scaling by the fractional method preserved significant correlations among LULC data and latent heat flux at all three studied scales (0.5°, 1.0°, and 2.5°), whereas nearest neighbor and majority aggregation methods caused these correlations to diminish, and even become statistically non-significant, at coarser spatial scales (i.e., 2.5°). Therefore, we recommend rescaling using fractional maps in observational LULCC-atmosphere studies.

This dissertation then resampled a newly developed time-series of LULC maps to 0.5° using the fractional method and identified fractional changes in croplands, forests, and grasslands in China from 1982 to 2012. I found that decreasing grasslands in the Northeast China plain and the Yellow river basin are significantly associated with increasing croplands. Similarly, increasing forests in the Yangtze river basin are significantly associated with decreasing croplands. In Southwest China, decreasing

grasslands and, to a lesser extent, decreasing croplands, are significantly correlated with the increasing forests.

In order to improve understanding of the physical mechanism behind impacts of croplands expansion on regional climate in China, I applied several statistical methods (e.g., linear regression analysis, correlation analysis, and granger-causality test) to explore the associations between croplands fraction and atmospheric variables (e.g., latent heat flux, sensible heat flux, surface temperature, multi-level temperature, and geopotential height). With the more robust croplands dynamic information identified in second chapter, this dissertation finds that croplands significantly increased in Northeast China during last three decades. The increased croplands result in increased latent heat flux in the regions within significantly increased croplands. The increased latent heat flux decreases surface temperature. This cooling effect of croplands expansion in Northeast China extends to the upper-level troposphere.

5.2 Future study
Considering the scope and limitation in this dissertation, there are several opportunities for future research.

1) *Production of continuous global land use and land cover maps dating back to the 1980s.* Land use and land cover map is a key component in land-atmosphere interaction studies. Currently, a long-term time series of global land use and land cover maps is very rare. The methodology in the first chapter can be applied to generate global land cover maps, which could improve accuracy of land surface information for global climate studies.

2) *Incorporation of alternative heat flux data for analyzing spatial scale mismatch between climate data and LULC data.* The latent heat flux data from FLUXNET-MTE in the second chapter used land use information, which may bias the results. Obtaining more reliable data is needed to better understand the spatial scale effects for LUCC data.

3) *Exploration the impacts of different LULCC types on climate using both observational methods and climate models.* The third chapter in this dissertation

only focused on cropland expansion due to time limitation. The second chapter showed that forests significantly increased in Southern China. An exploration of the afforestation impacts on regional climate would be very interesting. In doing so, we could understand how different LULCC types influence climate. In addition, in the third chapter, we only used observational methods. Comparing the results from climate models could improve the understanding of physical mechanism related to LULCC affects on climate.

6 Reference

Adegoke, J. O., R. A. Pielke Sr, J. Eastman, R. Mahmood & K. G. Hubbard (2003) Impact of irrigation on midsummer surface fluxes and temperature under dry synoptic conditions: A regional atmospheric model study of the US High Plains. *Monthly Weather Review,* 131**,** 556-564.

An, Y., W. Gao, Z. Gao, C. Liu & R. Shi (2015) Trend analysis for evaluating the consistency of Terra MODIS and SPOT VGT NDVI time series products in China. *Frontiers of earth science,* 9**,** 125-136.

Andres, L., W. A. Salas & D. Skole (1994) Fourier analysis of multi-temporal AVHRR data applied to a land cover classification. *TitleREMOTE SENSING,* 15**,** 1115-1121.

Baboo, S. S. & M. R. Devi (2010) An analysis of different resampling methods in Coimbatore, District. *Global Journal of Computer Science and Technology,* 10**,** 61-66.

Baker, B. A., T. A. Warner, J. F. Conley & B. E. McNeil (2013) Does spatial resolution matter? A multi-scale comparison of object-based and pixel-based methods for detecting change associated with gas well drilling operations. *International journal of remote sensing,* 34**,** 1633-1651.

Baudron, P., F. Alonso-Sarría, J. L. García-Aróstegui, F. Cánovas-García, D. Martínez-Vicente & J. Moreno-Brotóns (2013) Identifying the origin of groundwater samples in a multi-layer aquifer system with Random Forest classification. *Journal of Hydrology,* 499**,** 303-315.

Betts, R. A. (2011) Climate science: Afforestation cools more or less. *Nature Geoscience,* 4**,** 504-505.

Biraud, S. C., W. J. Riley, M. L. Fischer, M. S. Torn & J. A. Berry. 2005. Spatially Distributed CO2, Sensible, and Latent Heat Fluxes over the Southern Great Plains. Lawrence Berkeley National Laboratory
.

Bonan, G. B. (2001) Observational evidence for reduction of daily maximum temperature by croplands in the Midwest United States. *Journal of Climate,* 14**,** 2430-2442.

Bonan, G. B., P. J. Lawrence, K. W. Oleson, S. Levis, M. Jung, M. Reichstein, D. M. Lawrence & S. C. Swenson (2011) Improving canopy processes in the Community Land Model version 4 (CLM4) using global flux fields empirically inferred from FLUXNET data. *Journal of Geophysical Research: Biogeosciences,* 116**,** G02014.

Bonan, G. B., D. Pollard & S. L. Thompson (1992) Effects of boreal forest vegetation on global climate. *Nature,* 359**,** 716-718.

Boyd, D. S., S. Almond, J. Dash, P. J. Curran & R. A. Hill (2011) Phenology of vegetation in Southern England from Envisat MERIS terrestrial chlorophyll index (MTCI) data. *International journal of remote sensing,* 32**,** 8421-8447.

Breiman, L. (2001) Random forests. *Machine learning,* 45**,** 5-32.

Cao, C. & N. S.-N. Lam. 1997. Understanding the scale and resolution effects in remote sensing and GIS. In *Scale in Remote Sensing and GIS,* eds. D. A. Quattrochi & M. F. Goodchild, 57-72. CRC Press.

Cao, Q., D. Yu, M. Georgescu, Z. Han & J. Wu (2015) Impacts of land use and land cover change on regional climate: a case study in the agro-pastoral transitional zone of China. *Environmental Research Letters,* 10**,** 124025.

Channan, S., K. Collins & W. Emanuel (2014) Global mosaics of the standard MODIS land cover type data. *University of Maryland and the Pacific Northwest National Laboratory, College Park, Maryland, USA.*

Chao, L. 2004. Flooding and droughts plague China, together. China Daily.

Chen, H., Z. Gao, W. Zeng, J. Liu, X. Tan, S. Han, S. Wang, Y. Zhao & C. Yu (2017) Scale Effects of Water Saving on Irrigation Efficiency: Case Study of a Rice-Based Groundwater Irrigation System on the Sanjiang Plain, Northeast China. *Sustainability,* 10**,** 47.

Chen, L. & P. A. Dirmeyer (2016) Adapting observationally based metrics of biogeophysical feedbacks from land cover/land use change to climate modeling. *Environmental Research Letters,* 11**,** 034002.

Chen, T., G. Wang, W. Yuan, A. Li & Y. Y. Liu (2016) Asymmetric NDVI trends of the two cropping seasons in the Huai River basin. *Remote Sensing Letters,* 7**,** 61-70.

Clark, M. L., T. M. Aide, H. R. Grau & G. Riner (2010) A scalable approach to mapping annual land cover at 250 m using MODIS time series data: A case study in the Dry Chaco ecoregion of South America. *Remote Sensing of Environment,* 114**,** 2816-2832.

Cleveland, R. B., W. S. Cleveland, J. E. McRae & I. Terpenning (1990) STL: A seasonal-trend decomposition procedure based on loess. *Journal of Official Statistics,* 6**,** 3-73.

Clifford, P., S. Richardson & D. Hémon (1989) Assessing the significance of the correlation between two spatial processes. *Biometrics,* 45**,** 123-134.

Cook, B. I., M. J. Puma & N. Y. Krakauer (2011) Irrigation induced surface cooling in the context of modern and increased greenhouse gas forcing. *Climate Dynamics,* 37**,** 1587-1600.

Cutler, D. R., T. C. Edwards Jr, K. H. Beard, A. Cutler, K. T. Hess, J. Gibson & J. J. Lawler (2007) Random forests for classification in ecology. *Ecology,* 88**,** 2783-2792.

Dappen, P. (2003) Using Satellite Imagery to Estimate Irrigated Land: A Case Study in Scotts Bluff and Kearney Counties, Summer 2002.

de Jong, R., S. de Bruin, A. de Wit, M. E. Schaepman & D. L. Dent (2011) Analysis of monotonic greening and browning trends from global NDVI time-series. *Remote Sensing of Environment,* 115**,** 692-702.

de Kok, R. J., O. A. Tuinenburg, P. N. Bonekamp & W. W. Immerzeel (2018) Irrigation as a potential driver for anomalous glacier behavior in High Mountain Asia. *Geophysical Research Letters,* 45**,** 2047-2054.

de Leeuw, J., H. Jia, L. Yang, X. Liu, K. Schmidt & A. Skidmore (2006) Comparing accuracy assessments to infer superiority of image classification methods. *International Journal of Remote Sensing,* 27**,** 223-232.

Dee, D. P., S. Uppala, A. Simmons, P. Berrisford, P. Poli, S. Kobayashi, U. Andrae, M. Balmaseda, G. Balsamo & P. Bauer (2011) The ERA‐Interim reanalysis: Configuration and performance of the data assimilation system. *Quarterly Journal of the royal meteorological society,* 137**,** 553-597.

DeFries, R., M. Hansen & J. Townshend (1995) Global discrimination of land cover types from metrics derived from AVHRR Pathfinder data. *Remote Sensing of Environment,* 54**,** 209-222.

DeFries, R. & J. Townshend (1994) NDVI-derived land cover classifications at a global scale. *International Journal of Remote Sensing,* 15**,** 3567-3586.

Deng, J., W. Chuangjun & X. Zhikang. 1983. *General view of agriculture geography of China*. Beijing: Science Press

Dirmeyer, P. A., X. Gao, M. Zhao, Z. Guo, T. Oki & N. Hanasaki (2006) The Second Global Soil Wetness Project (GSWP-2): Multi-model analysis and implications for our perception of the land surface. *Bull. Am. Meteorol. Soc,* 87**,** 1381-1397.

Douglas, E., A. Beltrán-Przekurat, D. Niyogi, R. Pielke Sr & C. Vörösmarty (2009) The impact of agricultural intensification and irrigation on land–atmosphere interactions and Indian monsoon precipitation—A mesoscale modeling perspective. *Global and Planetary Change,* 67**,** 117-128.

Douglas, E. M., D. Niyogi, S. Frolking, J. Yeluripati, R. A. Pielke, N. Niyogi, C. Vörösmarty & U. Mohanty (2006) Changes in moisture and energy fluxes due to agricultural land use and irrigation in the Indian Monsoon Belt. *Geophysical Research Letters,* 33.

Eklundh, L. & P. Jönsson. 2015. TIMESAT 3.2 with parallel processing Software Manual. ed. S. Lund and Malmö University.

Elsner, J. B. (2007) Granger causality and Atlantic hurricanes. *Tellus A,* 59**,** 476-485.

Eltahir, E. A. (1996) Role of vegetation in sustaining large‐scale atmospheric circulations in the tropics. *Journal of Geophysical Research: Atmospheres,* 101**,** 4255-4268.

Fan, F., Q. Weng & Y. Wang (2007) Land use and land cover change in Guangzhou, China, from 1998 to 2003, based on Landsat TM/ETM+ imagery. *Sensors,* 7**,** 1323-1342.

Fenning, T. 2014. *Challenges and Opportunities for the World's Forests in the 21st Century*. Netherlands: Springer.

Foley, J. A., M. H. Costa, C. Delire, N. Ramankutty & P. Snyder (2003) Green surprise? How terrestrial ecosystems could affect earth's climate. *Frontiers in Ecology and the Environment,* 1**,** 38-44.

Foley, J. A., R. DeFries, G. P. Asner, C. Barford, G. Bonan, S. R. Carpenter, F. S. Chapin, M. T. Coe, G. C. Daily & H. K. Gibbs (2005) Global consequences of land use. *science,* 309**,** 570-574.

Freund, R. J., W. J. Wilson & P. Sa. 2006. *Regression analysis*. Academic Press.

Friedl, M. A., D. K. McIver, J. C. Hodges, X. Zhang, D. Muchoney, A. H. Strahler, C. E. Woodcock, S. Gopal, A. Schneider & A. Cooper (2002) Global land cover mapping from MODIS: algorithms and early results. *Remote Sensing of Environment,* 83**,** 287-302.

Friedl, M. A., D. Sulla-Menashe, B. Tan, A. Schneider, N. Ramankutty, A. Sibley & X. Huang (2010) MODIS Collection 5 global land cover: Algorithm refinements and characterization of new datasets. *Remote Sensing of Environment,* 114**,** 168-182.

Fu, C. (2003) Potential impacts of human-induced land cover change on East Asia monsoon. *Global and Planetary Change,* 37**,** 219-229.

Gao, F., J. T. Morisette, R. E. Wolfe, G. Ederer, J. Pedelty, E. Masuoka, R. Myneni, B. Tan & J. Nightingale (2008) An algorithm to produce temporally and spatially continuous MODIS-LAI time series. *IEEE Geoscience and Remote Sensing Letters,* 5**,** 60-64.

Ge, Q., J. Dai, F. He, J. Zheng, Z. Man & Y. Zhao (2004) Spatiotemporal dynamics of reclamation and cultivation and its driving factors in parts of China during the last three centuries. *Progress in Natural Science,* 14**,** 605-613.

Granger, C. W. (1969) Investigating causal relations by econometric models and cross-spectral methods. *Econometrica: Journal of the Econometric Society***,** 424-438.

Grantz, K., B. Rajagopalan, M. Clark & E. Zagona (2005) A technique for incorporating large‐scale climate information in basin‐scale ensemble streamflow forecasts. *Water Resources Research,* 41.

Gu, C., L. Hu, X. Zhang, X. Wang & J. Guo (2011) Climate change and urbanization in the Yangtze River Delta. *Habitat International,* 35**,** 544-552.

Han, P., Z. Li & J. Gong. 2010. Effects of aggregation methods on image classification. In *Geospatial Technology for Earth Observation*, 271-288. Springer.

Han, S. & Z. Yang (2013) Cooling effect of agricultural irrigation over Xinjiang, Northwest China from 1959 to 2006. *Environmental Research Letters,* 8**,** 024039.

Hansen, M., R. DeFries, J. R. Townshend & R. Sohlberg (2000) Global land cover classification at 1 km spatial resolution using a classification tree approach. *International journal of remote sensing,* 21**,** 1331-1364.

He, H. & X. Shi (2015) Spatio-Temporal Characteristics of Land Cover Changes in China During 1990-2010. *Journal of Geo-information Science,* 11**,** 008.

He, Y. & E. Lee (2016) Empirical relationships of sea surface temperature and vegetation activity with summer rainfall variability over the Sahel. *Earth Interactions,* 20**,** 1-18.

He, Y., E. Lee & T. A. Warner. 2016. Continuous annual land use and land cover mapping using AVHRR GIMMS NDVI3g and MODIS MCD12Q1 datasets over China from 1982 to 2012. In *IEEE International Geoscience and Remote Sensing Symposium (IGARSS)*, 5470-5472. Beijing, China: IEEE.

--- (2017) A time series of annual land use and land cover maps of China from 1982 to 2012 generated using AVHRR GIMMS NDVI3g data. *Remote Sensing of Environment,* 199**,** 201-217.

He, Y., T. A. Warner, B. E. McNeil & E. Lee (2018) Reducing uncertainties in applying remotely sensed land use and land cover maps in land-atmosphere interaction: identifying change in space and time. *Remote Sensing,* 10**,** 506.

Heumann, B. W., J. Seaquist, L. Eklundh & P. Jönsson (2007) AVHRR derived phenological change in the Sahel and Soudan, Africa, 1982–2005. *Remote Sensing of Environment,* 108**,** 385-392.

Hogg, R. V., E. Tanis & D. Zimmerman. 2014. *Probability and statistical inference*. Pearson Higher Ed.

Holben, B. N. (1986) Characteristics of maximum-value composite images from temporal AVHRR data. *International journal of remote sensing,* 7**,** 1417-1434.

Hou, X. (1981) A further discussion on the principle and scheme for vegetation regionalization of China. *Acta Phytoecologica et Geobotanica Sinica,* 5**,** 290-301.

Houghton, R. & J. Hackler (2003) Sources and sinks of carbon from land‐use change in China. *Global Biogeochemical Cycles,* 17.

IPCC. 2014. Climate Change: Impacts, Adaptation, and Vulnerability. United Kingdom and New York, USA: Cambridge University Press.

James, M. & S. N. Kalluri (1994) The Pathfinder AVHRR land data set: an improved coarse resolution data set for terrestrial monitoring. *International Journal of Remote Sensing,* 15**,** 3347-3363.

Jensen, J. R. 2016. *Introductory digital image processing: a remote sensing perspective (4th Edition).* Gleview, IL.: Pearson.

Jiang, B., S. Liang & W. Yuan (2015) Observational evidence for impacts of vegetation change on local surface climate over northern China using the Granger causality test. *Journal of Geophysical Research: Biogeosciences,* 120**,** 1-12.

Jones, P., D. Lister & Q. Li (2008) Urbanization effects in large‐scale temperature records, with an emphasis on China. *Journal of Geophysical Research: Atmospheres (1984‐2012),* 113.

Jönsson, P. & L. Eklundh (2002) Seasonality extraction by function fitting to time-series of satellite sensor data. *Geoscience and Remote Sensing, IEEE Transactions on,* 40**,** 1824-1832.

--- (2004) TIMESAT—a program for analyzing time-series of satellite sensor data. *Computers & Geosciences,* 30**,** 833-845.

Jung, M., M. Reichstein & A. Bondeau (2009) Towards global empirical upscaling of FLUXNET eddy covariance observations: validation of a model tree ensemble approach using a biosphere model. *Biogeosciences,* 6**,** 2001-2013.

Jung, M., M. Reichstein, P. Ciais, S. I. Seneviratne, J. Sheffield, M. L. Goulden, G. Bonan, A. Cescatti, J. Chen & R. De Jeu (2010) Recent decline in the global land evapotranspiration trend due to limited moisture supply. *Nature,* 467**,** 951.

Jung, M., M. Reichstein, H. A. Margolis, A. Cescatti, A. D. Richardson, M. A. Arain, A. Arneth, C. Bernhofer, D. Bonal & J. Chen (2011) Global patterns of land‐atmosphere fluxes of carbon dioxide, latent heat, and sensible heat derived from eddy covariance, satellite, and meteorological observations. *Journal of Geophysical Research: Biogeosciences,* 116**,** G00J07.

Kang, L., X. Han, Z. Zhang & O. J. Sun (2007) Grassland ecosystems in China: review of current knowledge and research advancement. *Philosophical Transactions of the Royal Society of London B: Biological Sciences,* 362**,** 997-1008.

Kaufmann, R. K. & D. I. Stern (1997) Evidence for human influence on climate from hemispheric temperature relations. *Nature,* 388**,** 39-44.

Kim, D.-H., J. O. Sexton, P. Noojipady, C. Huang, A. Anand, S. Channan, M. Feng & J. R. Townshend (2014) Global, Landsat-based forest-cover change from 1990 to 2000. *Remote Sensing of Environment,* 155**,** 178-193.

Korontzi, S., J. McCarty, T. Loboda, S. Kumar & C. Justice (2006) Global distribution of agricultural fires in croplands from 3 years of Moderate Resolution Imaging Spectroradiometer (MODIS) data. *Global Biogeochemical Cycles,* 20**,** GB2021.

Koster, R. D. & S. P. P. Mahanama (2012) Land surface controls on hydroclimatic means and variability. *Journal of Hydrometeorology,* 13**,** 1604-1620.

Lawrence, P. J. & T. N. Chase (2007) Representing a new MODIS consistent land surface in the Community Land Model (CLM 3.0). *Journal of Geophysical Research: Biogeosciences,* 112.

--- (2010) Investigating the climate impacts of global land cover change in the community climate system model. *International Journal of Climatology,* 30**,** 2066-2087.

Lawrence, P. J., J. J. Feddema, G. B. Bonan, G. A. Meehl, B. C. O'Neill, K. W. Oleson, S. Levis, D. M. Lawrence, E. Kluzek & K. Lindsay (2012) Simulating the biogeochemical and biogeophysical impacts of transient land cover change and wood harvest in the Community Climate System Model (CCSM4) from 1850 to 2100. *Journal of Climate,* 25**,** 3071-3095.

Lee, E., T. N. Chase & B. Rajagopalan (2008) Highly improved predictive skill in the forecasting of the East Asian summer monsoon. *Water resources research,* 44.

Lee, E., T. N. Chase, B. Rajagopalan, R. G. Barry, T. W. Biggs & P. J. Lawrence (2009) Effects of irrigation and vegetation activity on early Indian summer monsoon variability. *International Journal of Climatology,* 29**,** 573-581.

Lee, E., Y. He, M. Zhou & J. Liang (2015) Potential feedback of recent vegetation changes on summer rainfall in the Sahel. *Physical Geography,* 36**,** 449-470.

Lee, E., W. J. Sacks, T. N. Chase & J. A. Foley (2011) Simulated impacts of irrigation on the atmospheric circulation over Asia. *Journal of Geophysical Research: Atmospheres* 116**,** D08114.

Li, Q. S., L. S. Willardson, W. Deng, X. J. Li & C. J. Liu (2005) Crop water deficit estimation and irrigation scheduling in western Jilin province, Northeast China. *Agricultural water management,* 71**,** 47-60.

Li, Y., M. Zhao, S. Motesharrei, Q. Mu, E. Kalnay & S. Li (2015) Local cooling and warming effects of forests based on satellite observations. *Nature communications,* 6**,** 6603.

Liaw, A., M. Wiener, L. Breiman & A. Cutler (2009) Package "randomforest". *Retrieved December,* 12**,** 2009.

Lin, G. & S. P. Ho (2003) China's land resources and land-use change: insights from the 1996 land survey. *Land Use Policy,* 20**,** 87-107.

Liu, J. 1996. *Macro-scale survey and dynamic study of natural resources and environment of China by remote sensing.* Beijing: China Science and Technology Press.

Liu, J., W. Kuang, Z. Zhang, X. Xu, Y. Qin, J. Ning, W. Zhou, S. Zhang, R. Li & C. Yan (2014) Spatiotemporal characteristics, patterns, and causes of land-use changes in China since the late 1980s. *Journal of Geographical Sciences,* 24**,** 195-210.

Liu, J., M. Liu, H. Tian, D. Zhuang, Z. Zhang, W. Zhang, X. Tang & X. Deng (2005) Spatial and temporal patterns of China's cropland during 1990–2000: an analysis based on Landsat TM data. *Remote Sensing of Environment,* 98**,** 442-456.

Liu, J., M. Liu, D. Zhuang, Z. Zhang & X. Deng (2003) Study on spatial pattern of land-use change in China during 1995–2000. *Science in China Series D: Earth Sciences,* 46**,** 373-384.

Liu, J., Z. Zhang, X. Xu, W. Kuang, W. Zhou, S. Zhang, R. Li, C. Yan, D. Yu & S. Wu (2010) Spatial patterns and driving forces of land use change in China during the early 21st century. *Journal of Geographical Sciences,* 20**,** 483-494.

Liu, J., D. Zhuang, Y. Ling & A. Y (1998) Vegetation Integrated Classification and Mapping Using Remote Sensingand GIS Techniques in Northeast China. *Journal of Remote Sensing,* 2**,** 285–291.

Liu, M. & H. Tian (2010) China's land cover and land use change from 1700 to 2005: Estimations from high‐resolution satellite data and historical archives. *Global Biogeochemical Cycles,* 24**,** GB3003.

Liu, M., H. Tian, Q. Yang, J. Yang, X. Song, S. E. Lohrenz & W. J. Cai (2013) Long‐term trends in evapotranspiration and runoff over the drainage basins of the Gulf of Mexico during 1901–2008. *Water Resources Research,* 49**,** 1988-2012.

Lobell, D. B., C. Bonfils & J.-M. Faurès (2008) The role of irrigation expansion in past and future temperature trends. *Earth Interactions,* 12**,** 1-11.

Loveland, T., B. Reed, J. Brown, D. Ohlen, Z. Zhu, L. Yang & J. Merchant (2000) Development of a global land cover characteristics database and IGBP DISCover from 1 km AVHRR data. *International Journal of Remote Sensing,* 21**,** 1303-1330.

Lunetta, R. S., J. F. Knight, J. Ediriwickrema, J. G. Lyon & L. D. Worthy (2006) Land-cover change detection using multi-temporal MODIS NDVI data. *Remote sensing of environment,* 105**,** 142-154.

Ma, D., M. Notaro, Z. Liu, G. Chen & Y. Liu (2013a) Simulated impacts of afforestation in East China monsoon region as modulated by ocean variability. *Climate dynamics,* 41**,** 2439-2450.

Ma, E., A. Liu, X. Li, F. Wu & J. Zhan (2013b) Impacts of vegetation change on the regional surface climate: a scenario-based analysis of afforestation in Jiangxi Province, China. *Advances in Meteorology,* 2013.

Mahmood, R., S. A. Foster, T. Keeling, K. G. Hubbard, C. Carlson & R. Leeper (2006) Impacts of irrigation on 20th century temperature in the northern Great Plains. *Global and Planetary Change,* 54**,** 1-18.

Mahmood, R., R. A. Pielke, K. G. Hubbard, D. Niyogi, P. A. Dirmeyer, C. McAlpine, A. M. Carleton, R. Hale, S. Gameda & A. Beltrán‐Przekurat (2014) Land cover changes and their biogeophysical effects on climate. *International Journal of Climatology,* 34**,** 929-953.

Man, W., Z. Wang, M. Liu, C. Lu, M. Jia, D. Mao & C. Ren (2016) Spatio-temporal dynamics analysis of cropland in Northeast China during 1990-2013 based on remote sensing. *Transactions of the Chinese Society of Agricultural Engineering,* 32**,** 1-10.

Maxwell, A. E. & T. A. Warner (2015) Differentiating mine-reclaimed grasslands from spectrally similar land cover using terrain variables and object-based machine learning classification. *International Journal of Remote Sensing,* 36**,** 4384-4410.

Maxwell, A. E., T. A. Warner & M. P. Strager (2016) Predicting Palustrine Wetland Probability Using Random Forest Machine Learning and Digital Elevation Data-Derived Terrain Variables. *Photogrammetric Engineering & Remote Sensing,* 82**,** 437-447.

McPherson, R. A. (2007) A review of vegetation—atmosphere interactions and their influences on mesoscale phenomena. *Progress in Physical Geography,* 31**,** 261-285.

Meng, L., D. Long, S. M. Quiring & Y. Shen (2014) Statistical analysis of the relationship between spring soil moisture and summer precipitation in East China. *International Journal of Climatology,* 34**,** 1511-1523.

Nellis, M. D., K. P. Price & D. Rundquist (2009) Remote sensing of cropland agriculture. *The SAGE handbook of remote sensing,* 1**,** 368-380.

NOAA. 2005. Composite Analysis Instructions.

Oki, T. & S. Kanae (2006) Global hydrological cycles and world water resources. *science,* 313**,** 1068-1072.

Olofsson, P., G. M. Foody, M. Herold, S. V. Stehman, C. E. Woodcock & M. A. Wulder (2014) Good practices for estimating area and assessing accuracy of land change. *Remote Sensing of Environment,* 148**,** 42-57.

Palacios-Orueta, A., M. Huesca, M. L. Whiting, J. Litago, S. Khanna, M. Garcia & S. L. Ustin (2012) Derivation of phenological metrics by function fitting to time-series of Spectral Shape Indexes AS1 and AS2: Mapping cotton phenological stages using MODIS time series. *Remote Sensing of Environment,* 126**,** 148-159.

Palmer, S., D. Odermatt, P. Hunter, C. Brockmann, M. Presing, H. Balzter & V. Tóth (2015) Satellite remote sensing of phytoplankton phenology in Lake Balaton using 10years of MERIS observations. *Remote Sensing of Environment,* 158**,** 441-452.

Pan, S., H. Tian, S. R. Dangal, Q. Yang, J. Yang, C. Lu, B. Tao, W. Ren & Z. Ouyang (2015) Responses of global terrestrial evapotranspiration to climate change and increasing atmospheric CO2 in the 21st century. *Earth's Future,* 3**,** 15-35.

Pearson, K. (1895) Note on regression and inheritance in the case of two parents. *Proceedings of the Royal Society of London,* 58**,** 240-242.

Peng, J., A. Loew, O. Merlin & N. E. Verhoest (2017) A review of spatial downscaling of satellite remotely sensed soil moisture. *Reviews of Geophysics,* 55**,** 341-366.

Piao, S., P. Ciais, Y. Huang, Z. Shen, S. Peng, J. Li, L. Zhou, H. Liu, Y. Ma & Y. Ding (2010) The impacts of climate change on water resources and agriculture in China. *Nature,* 467**,** 43-51.

Pielke, R., J. Eastman, T. Chase, J. Knaff & T. Kittel (1998) 1973‑1996 Trends in depth‑averaged tropospheric temperature. *Journal of Geophysical Research: Atmospheres,* 103**,** 16927-16933.

Pielke, R. A. (2005) Land use and climate change. *Science,* 310**,** 1625-1626.

Pielke, R. A., A. Pitman, D. Niyogi, R. Mahmood, C. McAlpine, F. Hossain, K. K. Goldewijk, U. Nair, R. Betts & S. Fall (2011) Land use/land cover changes and climate: modeling analysis and observational evidence. *Wiley Interdisciplinary Reviews: Climate Change,* 2**,** 828-850.

Pontius, R. G. & M. Millones (2011) Death to Kappa: birth of quantity disagreement and allocation disagreement for accuracy assessment. *International Journal of Remote Sensing,* 32**,** 4407-4429.

Puma, M. & B. Cook (2010) Effects of irrigation on global climate during the 20th century. *Journal of Geophysical Research: Atmospheres,* 115.

Qiao, H., M. Wu, M. Shakir, L. Wang, J. Kang & Z. Niu (2016) Classification of Small-Scale Eucalyptus Plantations Based on NDVI Time Series Obtained from Multiple High-Resolution Datasets. *Remote Sensing,* 8**,** 117.

Ramankutty, N. & J. A. Foley (1999) Estimating historical changes in global land cover: Croplands from 1700 to 1992. *Global Biogeochemical Cycles,* 13**,** 997-1027.

Rawat, J. & M. Kumar (2015) Monitoring land use/cover change using remote sensing and GIS techniques: A case study of Hawalbagh block, district Almora, Uttarakhand, India. *The Egyptian Journal of Remote Sensing and Space Science,* 18**,** 77-84.

Reed, B. C., J. F. Brown, D. VanderZee, T. R. Loveland, J. W. Merchant & D. O. Ohlen (1994) Measuring phenological variability from satellite imagery. *Journal of vegetation science,* 5**,** 703-714.

Rodriguez-Galiano, V., M. Chica-Olmo, F. Abarca-Hernandez, P. M. Atkinson & C. Jeganathan (2012) Random Forest classification of Mediterranean land cover using multi-seasonal imagery and multi-seasonal texture. *Remote Sensing of Environment,* 121**,** 93-107.

Rouse Jr, J. W., R. Haas, J. Schell & D. Deering (1974) Monitoring vegetation systems in the Great Plains with ERTS. *NASA special publication,* 351**,** 309.

Running, S. W., T. R. Loveland & L. L. Pierce (1994) A vegetation classification logic based on remote sensing for use in global biogeochemical models. *Ambio,* 23**,** 77-77.

Sabins, J. & K. Lulla (1987) Remote sensing: Principles and interpretation.

Schneider, A. & C. Mertes (2014) Expansion and growth in Chinese cities, 1978–2010. *Environmental Research Letters,* 9**,** 024008.

Sexton, J. O., X.-P. Song, M. Feng, P. Noojipady, A. Anand, C. Huang, D.-H. Kim, K. M. Collins, S. Channan & C. DiMiceli (2013) Global, 30-m resolution continuous fields of tree cover: Landsat-based rescaling of MODIS vegetation continuous fields with lidar-based estimates of error. *International Journal of Digital Earth,* 6**,** 427-448.

Shi, D. & X. Yang (2016) An Assessment of Algorithmic Parameters Affecting Image Classification Accuracy by Random Forests. *Photogrammetric Engineering & Remote Sensing,* 82**,** 407-417.

Speiser, J. L., V. L. Durkalski & W. M. Lee (2015) Random forest classification of etiologies for an orphan disease. *Statistics in medicine,* 34**,** 887-899.

Sun, L., B. Shen, Z. Gao, B. Sui, L. Bai, S.-H. Wang, G. An & J. Li (2007) The impacts of moisture transport of East Asian monsoon on summer precipitation in Northeast China. *Advances in Atmospheric Sciences,* 24**,** 606-618.

Takata, K., K. Saito & T. Yasunari (2009) Changes in the Asian monsoon climate during 1700–1850 induced by preindustrial cultivation. *Proceedings of the National Academy of Sciences,* 106**,** 9586-9589.

Tong, X., M. Brandt, Y. Yue, S. Horion, K. Wang, W. De Keersmaecker, F. Tian, G. Schurgers, X. Xiao & Y. Luo (2018) Increased vegetation growth and carbon stock in China karst via ecological engineering. *Nature Sustainability,* 1**,** 44.

Townshend, J., C. Justice, W. Li, C. Gurney & J. McManus (1991) Global land cover classification by remote sensing: present capabilities and future possibilities. *Remote Sensing of Environment,* 35**,** 243-255.

Townshend, J. R., C. Justice & V. Kalb (1987) Characterization and classification of South American land cover types using satellite data. *International Journal of Remote Sensing,* 8**,** 1189-1207.

Trenberth, K. E., J. T. Fasullo & J. Kiehl (2009) Earth's global energy budget. *Bulletin of the American Meteorological Society,* 90**,** 311-323.

Tucker, C. J., J. E. Pinzon, M. E. Brown, D. A. Slayback, E. W. Pak, R. Mahoney, E. F. Vermote & N. El Saleous (2005) An extended AVHRR 8‑km NDVI dataset compatible with MODIS and SPOT vegetation NDVI data. *International Journal of Remote Sensing,* 26**,** 4485-4498.

Tucker, C. J., J. R. Townshend & T. E. Goff (1985) African land-cover classification using satellite data. *Science,* 227**,** 369-375.

USDA. 2016. ⌷This is Northeast China.

Waldron, S., C. Brown & J. Longworth. 2008. An assessment of China's approach to grassland degradation and livelihood problems in the pastoral region. In *5th Annual Conference of the Consortium for Western China Development Studies*. Xi'an, China.

Walpole, R. E., R. H. Myers, S. L. Myers & K. Ye. 1993. *Probability and statistics for engineers and scientists*. New York: Macmillan.

Wang, F., M. Notaro, Z. Liu & G. Chen (2014) Observed Local and Remote Influences of Vegetation on the Atmosphere across North America Using a Model-Validated Statistical Technique That First Excludes Oceanic Forcings*. *Journal of Climate,* 27**,** 362-382.

Wang, X., H. Shen, W. Zhang, J. Cao, Y. Qi, G. Chen & X. Li (2015) Spatial and temporal characteristics of droughts in the Northeast China Transect. *Natural Hazards,* 76**,** 601-614.

Webster, P. J. 1987. The elementary monsoon. 3-32. Wiley: New York.

Wei, J., P. A. Dirmeyer, D. Wisser, M. G. Bosilovich & D. M. Mocko (2013) Where does the irrigation water go? An estimate of the contribution of irrigation to precipitation using MERRA. *Journal of Hydrometeorology,* 14**,** 275-289.

Williams, I. N. & M. S. Torn (2015) Vegetation controls on surface heat flux partitioning, and land‑atmosphere coupling. *Geophysical Research Letters,* 42**,** 9416-9424.

Woodcock, C. E. & A. H. Strahler (1987) The factor of scale in remote sensing. *Remote sensing of Environment,* 21**,** 311-332.

Woodcock, C. E., A. H. Strahler & D. L. Jupp (1988) The use of variograms in remote sensing: I. Scene models and simulated images. *Remote Sensing of Environment,* 25**,** 323-348.

Wu, W.-b., Y. Peng, H.-j. TANG, Q.-b. ZHOU, Z.-x. CHEN & R. Shibasaki (2010) Characterizing spatial patterns of phenology in cropland of China based on remotely sensed data. *Agricultural Sciences in China,* 9**,** 101-112.

Xue, Y. (1996) The impact of desertification in the Mongolian and the Inner Mongolian grassland on the regional climate. *Journal of Climate,* 9**,** 2173-2189.

Yang, B., Y. Zhang, Y. Qian, J. Tang & D. Liu (2016) Climatic effects of irrigation over the Huang‑Huai‑Hai Plain in China simulated by the weather research and forecasting model. *Journal of Geophysical Research: Atmospheres,* 121**,** 2246-2264.

Yang, F. & K. M. Lau (2004) Trend and variability of China precipitation in spring and summer: linkage to sea‑surface temperatures. *International Journal of Climatology,* 24**,** 1625-1644.

Yang, L., W.-l. Jiang, X. Bi-lin & L. Bo (2014) Observed Climatic Variations in the Growing Season of Field Crops in Northeast China from 1992 to 2012. *Journal of Integrative Agriculture,* 13**,** 1451-1461.

Yang, Z. L., Y. Dai, R. Dickinson & W. Shuttleworth (1999) Sensitivity of ground heat flux to vegetation cover fraction and leaf area index. *Journal of Geophysical Research: Atmospheres,* 104**,** 19505-19514.

Ye, J. S. (2014) Trend and variability of China's summer precipitation during 1955–2008. *International Journal of Climatology,* 34**,** 559-566.

Ye, Y. & X. Fang (2009) Land use change in Northeast China in the twentieth century: a note on sources, methods and patterns. *Journal of Historical Geography,* 35**,** 311-329.

Yi, Y. 2014. NE China drought leaves 330,000 thirsty.

Yin, G., Y. Zhang, Y. Sun, T. Wang, Z. Zeng & S. Piao (2015) MODIS Based Estimation of Forest Aboveground Biomass in China. *PloS one,* 10**,** e0130143.

Yin, X. (2008) Analysis on the change of land use by remote sensing technology in Manas county. *Journal of Shihezi University (Natural Science),* 26**,** 402-406.

Yin, X., M. Jabloun, J. E. Olesen, I. Öztürk, M. Wang & F. Chen (2016) Effects of climatic factors, drought risk and irrigation requirement on maize yield in the Northeast Farming Region of China. *The Journal of Agricultural Science,* 154**,** 1171-1189.

Zhang, X., M. A. Friedl & C. B. Schaaf (2006) Global vegetation phenology from Moderate Resolution Imaging Spectroradiometer (MODIS): Evaluation of global patterns and comparison with in situ measurements. *Journal of Geophysical Research: Biogeosciences,* 111.

Zhang, X., Q. Tang, J. Zheng & Q. Ge (2013) Warming/cooling effects of cropland greenness changes during 1982–2006 in the North China Plain. *Environmental Research Letters,* 8**,** 024038.

Zhao, N., S. Han, D. Xu, J. Wang & H. Yu (2016) Cooling and wetting effects of agricultural development on near-surface atmosphere over northeast China. *Advances in Meteorology,* 2016.

Zhao, X., P. Xu, T. Zhou, Q. Li & D. Wu (2013) Distribution and variation of forests in China from 2001 to 2011: A study based on remotely sensed data. *Forests,* 4**,** 632-649.

Zhao, Y., Y. Fang, C. Cui & A. Huang (2012) Effects of irrigation on precipitation in the arid regions of Xinjiang, China. *Journal of Arid Land,* 4**,** 132-139.

Zhu, X. (2012) The impact of agricultural irrigation on land surface characteristics and near surface climate in China.

Zhu, X., S. Liang & Y. Pan (2012) Observational evidence of the cooling effect of agricultural irrigation in Jilin, China. *Climatic change,* 114**,** 799-811.